

NASA Contractor Report 175023  
DOT-FAA-CT-86-1

# Particle Trajectory Computation on a 3-Dimensional Engine Inlet

(NASA-CR-175023) PARTICLE TRAJECTORY  
COMPUTATION ON A 3-DIMENSIONAL ENGINE INLET  
Final Report Ph.D. Thesis (Wichita State  
Univ.) 115 p HC A06/MF A01 C SCL 01C

N86-20379

G3/03 Unclas  
05518

John J. Kim  
Wichita State University  
Wichita, Kansas



January 1986

Prepared for  
Lewis Research Center  
Under Grant NAG 3-566

**NASA**  
National Aeronautics and  
Space Administration

  
US Department of Transportation  
Federal Aviation Administration

## PREFACE

The author would like to thank Dr. G. W. Zumwalt for his guidance and support throughout the course of this work. He is grateful to the Boeing Military Airplane Company (BMAC), Wichita, for funding this research through the BMAC IR&D Project 935.

The author would also like to thank: M. D. Breer of BMAC (Wichita) for his constant help and encouragement throughout the code development process; Dr. R. Elangovan of BMAC (Wichita) who provided many fruitful consultations and encouragement; Mr. W. Seibel for the help received in making the code efficient and the post-processor code development; Mr. A. B. Herren and D. T. Sawdy for supporting this project from the very beginning and for their critical reviews of various reports and a technical paper materialized from this project; Dr. T. A. Reyhner of Boeing Commercial Airplane Company (BCAC) for providing and modifying his CFD code for generating flow data used in this study; Mr. W. R. Jones and B. S. Terrill of BCAC for providing the bi-cubic patch parameter data for the inlet geometry investigated; Mr. J. Gass for providing the valuable computer graphics support for this project; Ms. J. Combs for her help in preparing many of the computer plots of the analysis results; Ms. K. Galliant for her help in the preparation of the manuscript.

This research was funded by BMAC, Wichita, through the Aircraft Systems and Propulsion Group.

## TABLE OF CONTENTS

	PAGE
PREFACE	i
NOMENCLATURE	vi
1.0 INTRODUCTION	1
2.0 PREVIOUS RELATED RESEARCH	5
3.0 TRAJECTORY MODEL	8
3.1 Model Assumptions	8
3.2 Trajectory Differential Equation	9
3.2.1 Meaning of P (inertia parameter)	10
3.2.2 Scaling of the Trajectory Problem	11
3.3 Drag Coefficient ( $C_D$ ) for Spherical Particles	11
3.3.1 Incompressible Sphere Drag Coefficient ( $C_D^{inc.}$ )	12
3.3.2 Cunningham Drag Correction ( $G(M/R_v)$ )	12
4.0 COMPUTATIONAL METHOD	15
4.1 Computational Procedure	15
4.2 Bi-cubic Surface Parametrization	15
4.3 Potential Flow Analysis	17
4.3.1 Flow Accuracy (3-D Full Potential Code)	18
4.3.2 Flow Velocity Interpolation at Trajectory Steps	18
4.3.2.1 Linear Interpolation Formula	18
4.3.2.2 Least-square Interpolation Formula	21

**PRECEDING PAGE BLANK NOT FILMED**

## TABLE OF CONTENTS

	PAGE
4.4 Numerical Integration of the Trajectory Differential Equation	27
4.4.1 Runge-Kutta Scheme (4th Order)	28
4.4.2 Adams Predictor-Corrector Scheme (4th Order)	29
4.4.3 Automatic Stepsize Control	29
4.5 Calculation of the Limiting Envelope of Trajectories	33
4.6 Calculation of the Local Droplet Impingement Efficiency ( $\beta$ )	35
4.7 Method for Solid Particles	41
5.0 RESULTS AND DISCUSSIONS	43
5.1 Analysis of Droplet Impingement on a Sphere	43
5.1.1 Langmuir-D Tunnel Droplet Size Distribution	45
5.1.2 Results	45
5.2 Analysis of Droplet Impingement on a 3-D Engine Inlet	47
5.2.1 Limiting Impingement Points	50
5.2.2 Droplet Trajectories on the Inlet Symmetry Plane	50
5.2.3 Computed Local Impingement Efficiency Distribution	51
5.3 Trajectory Simulation for a Solid Particle	62
6.0 CONCLUSIONS AND RECOMMENDATIONS FOR FURTHER WORK	64

## TABLE OF CONTENTS

	PAGE
APPENDIX A - Parametric Description of Curves and Surfaces	66
A.1.0 Parametric Curve Description	66
A.1.1 Parametric Cubic Curve Representation	67
A.2.0 Parametric Surface Description	70
A.2.1 Parametric Bi-cubic Surface Representation	70
A.2.2 Geometrical Properties of Bi-cubic Surface Parametrization	75
A.2.3 Coordinate Transformations on Patch Surface	77
A.3.0 Trajectory - Bi-cubic Patch Intersection	77
A.3.1 Problem Definition	78
A.3.2 Numerical Method	78
APPENDIX B - Derivation of the Trajectory Equation (3-1)	81
APPENDIX C - Table of Sphere Drag Coefficient	84
APPENDIX D - Comparison between the Computed 3-D Full Potential CFD Flow Data and Wind Tunnel Test Data	86
REFERENCES	97

## NOMENCLATURE

$a$	local sonic speed
$a_{\infty}$	sonic speed at freestream
$a_0(i,j)$	area of the freestream starting point grid element $\{\bar{x}_0(I,J)\}$
$a_m(i,j)$	area of the surface impingement point grid element $\{\bar{x}_m(I,J)\}$
$a_m^1(i,j,k)$	least-square flow velocity interpolation coefficient array associated with the surface cell $(i,j,k)$
$\bar{B}$	buoyancy force acting on the droplet
$C$	characteristic dimension of body
$C_D$	droplet drag coefficient
$C_D^{inc.}$	incompressible sphere drag coefficient
$c_i$	fraction of total LWC contributed by Langmuir-D multi-droplet droplets of diameter $d_i$
$\bar{D}$	fluid dynamic drag force acting on the droplet
$d$	droplet diameter
$dA$	infinitesimal impingement area on body surface
$dA_{\infty}$	infinitesimal freestream cross-section corresponding to $dA$

## NOMENCLATURE

$d_i$	$i$ th Langmuir-D multi-droplet droplet diameter
$\{f_i\}$	parametric cubic blending function basis; $i=1,2,3,4$
$G$	Cunningham drag correction factor
$\bar{G}$	gravity force acting on the droplet
$g$	gravitational acceleration
$h$	stepsize used in the numerical integration of the trajectory differential equation
$i,j,k$	computational $x,r,\theta$ mesh node indices
$\hat{i},\hat{j},\hat{k}$	unit vectors // to $x,y,z$ axis
$K(R_v)$	Stokes' parameter of droplet = $C_D(R_v) \cdot R_v / 24$
$K_n$	Knudsen number = $\lambda/d$
$\bar{T}$	position vector along a trajectory segment
$L$	length of a trajectory segment = $ \bar{p} - \bar{q} $
LWC	liquid water content of droplet cloud at freestream
LWC'	liquid water content at body surface
$M$	Mach number of air flow relative to droplet

## NOMENCLATURE

$M_{CF}$	Mach number of air flow at compressor face
$M_{\infty}$	Mach number of air flow at freestream
MVD	mean volumetric diameter of the droplet cloud
$\bar{n}$	unit normal vector at body surface (pointing outward)
$\bar{n}_{\infty}$	unit vector // to $\bar{V}_{\infty}$
P	inertia parameter of droplet = $\rho * V_{\infty} d^2 / (18\mu C)$
$P_{S\infty}$	freestream static pressure of air
$\bar{p}, \bar{q}$	trajectory segment end points
$[\bar{Q}]$	bi-cubic patch boundary condition matrix
R	Reynolds number of air flow based on d
$R_v$	Reynolds number of air flow relative to droplet
$r_{max}$	radial boundary for cylindrical computational domain
$r_n, r_t$	normal or tangential resiliency coefficient of solid particle
$r_{CF}$	inlet fan radius
$\bar{r}(u,v)$	position on a bi-cubic parametric patch surface



## NOMENCLATURE

$\bar{r}_u(u,v)$	tangent vector along a constant- $v$ parameter curve on a patch surface = $\partial\bar{r}(u,v)/\partial u$
$\bar{r}_{uv}(u,v)$	twist vector = $\partial^2\bar{r}(u,v)/\partial u\partial v$
$S$	total surface area of body surface (or a patch)
$s$	arc length along a constant- $\theta$ curve on body surface
$T_{s\infty}$	freestream static temperature of air
$t$	time, dimensionless with $C/V_\infty$
$\tilde{t}$	time
$[U]$	$u$ -parameter basis function = $[1 \ u \ u^2 \ u^3]$
$[V]$	$v$ -parameter basis function = $[1 \ v \ v^2 \ v^3]$
$\bar{U}$	droplet velocity, dimensionless with $V_\infty$
$\tilde{U}$	droplet velocity
$\bar{V}$	potential flow velocity, dimensionless with $V_\infty$
$\tilde{V}$	potential flow velocity
$\bar{V}_\infty$	freestream air velocity
$\bar{U}_c, \bar{x}_c$	droplet velocity or position computed at a corrector step (Adams predictor-corrector)

## NOMENCLATURE

$\bar{U}_p, \bar{x}_p$	droplet velocity or position computed at a predictor step (Adams predictor-corrector)
$w$	normalized line (trajectory segment) length parameter
$w(i,j,k)$	sub-cell volume of a cylindrical field cell, with a corner at node $(i,j,k)$
$X_{CF}$	compressor face x-boundary
$X_\infty$	freestream x-boundary of cylindrical computational domain
$\bar{x}$	droplet trajectory position, dimensionless with $C$
$x, r, \theta$	cylindrical coordinates
$x, y, z$	Cartesian coordinates
$\bar{x}_0(I,J)$	freestream starting point grid
$\bar{x}_m(I,J)$	impingement point grid
$\bar{x}_c(i,j)$	impingement centroid grid
$\alpha$	angle of attack (pitch angle)
$\beta$	local impingement efficiency
$\gamma$	ratio of specific heats of air = 1.4
$\gamma_m$	incident angle at impact (solid particle)

## NOMENCLATURE

$\delta$	Kronecker delta
$\delta V$	flowfield resolution (error)
$\sigma$	density ratio = $\rho/\rho^*$
$\varepsilon$	integration error estimate at Adams predictor-corrector step
$\varepsilon_1$	maximum absolute discrepancy between $\bar{U}_c$ and $\bar{U}_p$
$\varepsilon_2$	maximum relative discrepancy between $\bar{U}_c$ and $\bar{U}_p$
$\rho$	density of air
$\rho^*$	density of droplet
$\mu$	absolute air viscosity
$\phi$	roll angle
$\psi$	yaw angle
$\varepsilon_{ijk}$	Levi-Civita anti-symmetric tensor
$\omega$	angle between a point on sphere and $xz$ -plane
$\bar{\xi}$	unit direction vector along the line from $\bar{p}$ to $\bar{q}$
$\Gamma$	freestream cross-section of the limiting envelope of trajectories

## NOMENCLATURE

$\lambda$	mean free path of air
$\lambda_1, \lambda_2$	stepsize adjustment factors
$\tau_v$	velocity relaxation time of a droplet

### Subscripts and superscripts

---

'	derivative of a quantity
o	quantity at freestream or origin
(n)	nth iterate
T	matrix transpose
n	normal component
t	tangential component

## 1.0 INTRODUCTION

The extent and local flux rate of water droplet impingement on affected aircraft surfaces constitute the basic information needed for the design and analysis of various ice protection systems.

The cause of aircraft ice accretion is mostly due to the presence of atmospheric clouds containing supercooled water droplets. The water droplet content of clouds generally decreases with altitude and beyond about 22,000 ft above sea level, called the icing altitude, clouds consist mainly of frozen particles and do not pose, in most circumstances, a significant icing hazard [1]. For a given condition within the icing envelope smaller supercooled droplets may freeze entirely upon impact with the aircraft surface (rime icing), while larger droplets, requiring larger amounts of latent heat removal, may freeze slowly with runback (glaze icing).

As the supercooled droplets impact on the surface, the governing transport parameter is the local droplet mass flux rate at the surface, which is in turn related to the normalized local surface flux function,  $\beta$  (local impingement efficiency):

$$\text{Local droplet impingement intensity} = \beta \cdot V_{\infty} \cdot \text{LWC} \left[ \frac{\text{unit weight}}{\text{unit area} \cdot \text{unit time}} \right]$$

$$\text{Total droplet impingement intensity} = V_{\infty} \cdot \text{LWC} \int_S \beta dS \left[ \frac{\text{unit weight}}{\text{unit time}} \right]$$

$$\text{where LWC} = \text{liquid water content at freestream} \left[ \frac{\text{unit weight}}{\text{unit volume}} \right]$$

$$S = \text{total surface area of body} \quad [\text{unit area}]$$

The definition of  $\beta$  as the local droplet flux rate normalized to the freestream flux rate follows from the continuity of droplet mass flow applied to an infinitesimal droplet stream tube (Figure 1) of differential area vectors  $d\bar{A}_\infty$  at freestream ( $d\bar{A}_\infty$  is not // to  $\bar{V}_\infty$  in general) and  $d\bar{A}$  at the surface of impact:

$$(LWC) \bar{V}_\infty \cdot d\bar{A}_\infty = (LWC)' \bar{V} \cdot d\bar{A} \text{ (mass flow continuity)}$$

$$(LWC) \bar{V}_\infty \bar{n}_\infty \cdot d\bar{A}_\infty = (LWC)' (-\bar{V} \cdot \bar{n}) dA$$

$$\beta = \frac{\bar{n}_\infty \cdot d\bar{A}_\infty}{dA} = \frac{(LWC)' (-\bar{V} \cdot \bar{n})}{(LWC) \bar{V}_\infty} = \frac{\text{mass flux at } dA}{\text{mass flux at } dA_\infty} \quad (1.0)$$

where  $\bar{n} \equiv$  unit normal vector at  $dA$ ,

$\bar{n}_\infty \equiv$  unit vector // to  $\bar{V}_\infty$ ,

$\bar{V} (\bar{V}_\infty) \equiv$  local droplet velocity vector at  $dA$  ( $dA_\infty$ ),

$(LWC)' \equiv$  liquid water content at  $dA$ .

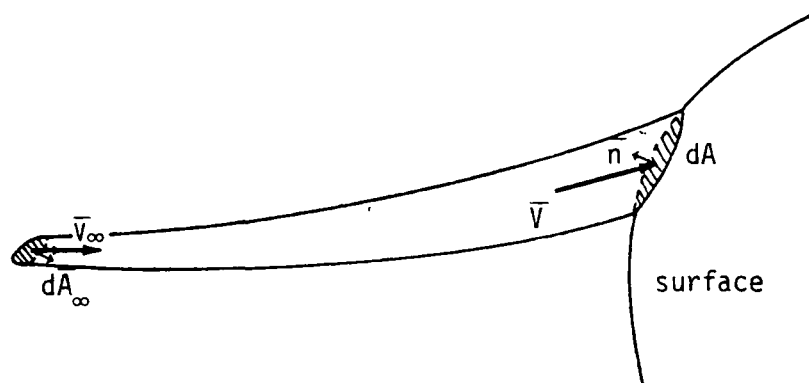


Figure 1 - Droplet Stream Tube

The ice protection systems currently in use or in development on various aircraft can typically be categorized into two kinds:

<u>System</u>	<u>Source</u>	<u>Typical Aircraft Application</u>
(a) anti-icing	hot air (bleed)	engine inlet, wing l.e., ram air scoop, pitot tube
(b) de-icing	pneumatic boot (pulsed air)	wing l.e., rotor blade
	electrothermal [2]	wing l.e., pitot tube, rotor blade, stabilizer
	electroimpulse [3]	wing l.e., rotor blade, strut, stabilizer
	fluid (freezing point depressant)	wing l.e. [4]

In an anti-icing system, heat is continuously supplied (during system operation) to the affected surface so that all of the impinging water can be evaporated or maintained above freezing. Thus, for the steady-state heat transfer analysis of the system, the total as well as the local water impingement intensities must be known at the icing interface.

As for the de-icing system, ice is allowed to accumulate to a certain level and heat or some form of mechanical energy is supplied in a transient manner to shed off the ice, thereby saving substantial energy expenditure (compared to the anti-icing system) at the expense of the aerodynamic penalty due to ice accretion. For the performance analysis of a de-icing system, the extent and shape of the ice accreted must be known as well as the tolerable level of ice accretion in terms of the associated aerodynamic penalty. Analytically, this requires ice accretion modeling [5,6], for which the local water impingement

intensity is an input, and detailed flow analysis about the body with the prescribed ice shape [7,8].

Thus the determination of local water droplet impingement efficiency ( $\beta$ ) on aircraft surfaces is a fundamental task in quantifying the aircraft icing phenomena.

Despite its importance in the design/analysis of ice protection systems for most of the present day engine inlets and wings which are highly 3-dimensional, there has been very little analytical or experimental work to determine the water droplet impingement efficiencies on 3-dimensional configurations.

The purpose of this research work is to develop a 3-dimensional particle trajectory analysis computer code to predict the local water droplet impingement efficiency ( $\beta$ ) on a representative commercial turbofan type engine inlet. This work grew out of the need to develop analysis tools leading to improved engine anti-icing and sand separator systems at the Boeing Military Airplane Company (BMAC), Wichita.



## 2.0 PREVIOUS RELATED RESEARCH

A detailed review of the relevant research literature is discussed in a recent report by Shaw [9].

The bulk of the available literature in the area of  $\beta$  determination comes from the extensive NACA icing research efforts in the 1940-1950 time period. The NACA research program concentrated mainly on the experimental determination of  $\beta$  on axisymmetric geometries [10,11] and 2-D airfoils [12-16].

One of the earlier analysis efforts is due to Langmuir and Blodgett [17] who calculated water droplet trajectories to predict impingement efficiencies about circular cylinders using a differential analyzer.

More recently, a number of researchers developed several water droplet trajectory codes to compute  $\beta$  [18-20] as well as to model ice accretion [5,6] and to assess aerodynamic penalties [7,8] on 2-D airfoils. Code development applicable for engine inlets was limited, partly due to the more complex flowfields involved and due to a complete lack of test data on these geometries. However, a code [21,22] was developed by BMAC and applied to various axisymmetric engine inlet anti-icing analysis problems.

Trajectory code development for 3-dimensional impingement problems has been of limited extent. Although two codes [23,24] exist that are capable of analyzing 3-D impingement problems, calculation of  $\beta$  was not reported.

The 3-D code developed by Norment [23] uses the Hess-Smith incompressible panel potential code [25] and a variable order Adams predictor-corrector integrator to solve the trajectory differential equation. To compute the fluid dynamic forces acting on the droplet at each trajectory position, it uses the direct approach of computing the

flow velocity at the required position by summing over all the panel source and vorticity contributions. Since each droplet trajectory involves computing hundreds of intermediate trajectory steps, the computing time will generally be high. As with other panel flow codes, the accuracy of computed flow velocities is ultimately limited by the panel density. For a trajectory segment near the panel surface, the intermediate trajectory steps will be crowded (compared to a segment far away from the surface) because of stronger flow gradients there. If the mean distance between these intermediate steps is small compared to the linear dimension of surface panels, the direct approach will result in non-smooth flow velocities along the trajectory and lead to numerical problems in solving the trajectory equation of motion. Thus, the choice of the direct approach for the trajectory code seems questionable in view of the inherent danger and high computing times involved. This code currently uses the non-lifting version of the Hess-Smith panel code, and is not applicable for problems involving engine inlets.

The recent 3-D code developed by Stock [24] employs a finite volume 3-D Euler flow code [26] and a 4th order Runge-Kutta scheme to solve the trajectory equation of motion. It was applied to the droplet impingement problem on a 3-D engine intake, utilizing a body-fitted computational mesh (grid approach). Body-fitted mesh definition of computational flow domain is generally accepted as one of higher flow resolution than any other fixed orthogonal mesh systems, because of its grid adaptability near the boundaries [27]. However, because of the finite volume approach employed, uniform flow velocity was assumed throughout the volume of each mesh cell, while at least five intermediate trajectory steps were computed in each mesh cell. This approach may be acceptable in the far field region, where the flowfield is approximately uniform. Near the boundary surface, the assumption of flow uniformity can be incorrect in predicting particle impact on the surface. The tangent impact points computed from this code indeed reveal erratic jumps between several pairs of adjacent tangent trajectories [24].

Since it is the fluid dynamic forces acting on the droplet that determine the droplet trajectory, accurate flowfield definition is a prerequisite for accurate droplet trajectory computation. For the grid approach, the additional requirement of accurate flow velocity interpolation along the trajectory must be met. Also, an accurate surface geometry definition of the body is needed in order to locate the impingement points precisely. This is not a trivial task for 3-dimensional geometries such as engine inlets.  $\beta$  is a local surface flux function and its accuracy is very sensitive to the local surface geometry. Flat panel surface definition, as is done in panel potential flow analyses, will not be adequate unless sufficient panel density is used.

For the present investigation, the grid approach is adapted based on the consideration of computational efficiency. Flow velocities were computed using a 3-D compressible full potential flow code [28,29] on a cylindrical mesh system. Linear and least-square interpolation techniques are employed for flow interpolation along trajectories to ensure smooth and accurate resolution of the flowfield. State-of-the-art bi-cubic parametric surface modeling techniques [30] are utilized to obtain an analytical definition of the 3-D engine inlet surface studied as well as to compute the impingement points accurately. Variable step fourth order Runge-Kutta and Adams predictor-corrector integration schemes were used to solve the trajectory equation, together with an automatic stepsize control scheme to maintain the desired integration accuracy in the numerical solution of the trajectory differential equation.

### 3.0 TRAJECTORY MODEL

The general motion of droplets moving through turbulent air flow regimes is not considered in this study. A rather simplistic approach, taken by researchers as early as 1940's [17], is to describe the quasi-steady motion of small spherical droplets moving in the steady flow of air, while the motion of droplets does not disturb the air flow. The predominant force acting on a droplet is then the fluid dynamic drag arising from the relative (slip) velocity of air with respect to the droplet. This is a valid approach in view of the fact that for the typical icing design conditions of intermittent and continuous maximum [1], the maximum concentration and mean volumetric diameter (MVD) of droplets are:

intermittent maximum

$$\text{LWC MAX} \approx 3.0 \text{ gm/m}^3$$

$$\text{MVD MAX} \approx 50 \text{ } \mu\text{m}$$

continuous maximum

$$\text{LWC MAX} \approx 0.8 \text{ gm/m}^3$$

$$\text{MVD MAX} \approx 40 \text{ } \mu\text{m}$$

For the concentrations and sizes of droplets within the icing envelope, the assumption of undisturbed airflow and spherical shape (due to surface tension) of droplets are quite valid.

#### 3.1 Model Assumptions

- (1) Single phase (air) flow about the body - particle phase does not disturb the flowfield of the gas phase.
- (2) Quasi-steady-state approximation - at each instant and position, the steady-state drag and other forces act on the particle.
- (3) Compressible or incompressible potential flowfield of the gas phase about the body.

(4) Spherical shape of particles.

Additionally, viscous flow effects such as thick boundary layer formation and flow separation are not considered because particle impingement usually occurs in the forward part of the body.

### 3.2 Trajectory Differential Equation

Under the model assumptions, the forces acting on the particle are the fluid drag, buoyancy, and gravity. By applying Newton's second law and non-dimensionalizing (Appendix B), the particle equations of motion reduce to the following:

$$dU_i/dt = C_D(R_v) \cdot R_v \cdot (V_i - U_i) / (24P) - (1-\sigma)g C \delta_{i2} / V_\infty^2 \quad (i = 1,2,3) \quad (3-1)$$

where

$$P \equiv \rho^* V_\infty d^2 / (18\mu C) = \text{inertia parameter of droplet.}$$

$$t \equiv \text{time (dimensionless with } C/V_\infty),$$

$$\sigma \equiv \rho/\rho^* = \text{density ratio of air to particle,}$$

$$C \equiv \text{characteristic dimension of body,}$$

$$R_v \equiv \text{relative Reynolds number of droplet,}$$

$$\bar{U} \equiv \text{particle velocity (dimensionless with } V_\infty),$$

$$\bar{V} \equiv \text{potential flow velocity (dimensionless with } V_\infty).$$

Because of the way the slip velocity,  $\bar{V} - \bar{U}$ , appears in the slip Reynolds number ( $R_v$ ), equation (3-1) must be solved numerically in general: in some ideal cases, when  $\bar{V}$  is a simple function of position and  $R_v$  can be expressed in a special form, equation (3-1) can be solved analytically [31,32].

### 3.2.1 Meaning of P (inertia parameter)

For a particle injected into the uniform flow,  $\bar{V} = \bar{V}_\infty$ , and obeying the Stokes' law of drag ( $C_D = 24/R_V$ ):

$$d\bar{U}/dt = (\bar{V}_\infty - \bar{U})/P \quad (3-2)$$

(neglecting  $(1-\sigma)gC/V_\infty^2 \ll 1$ .)

Equation (3-2) can be written as

$$d(\bar{U} - \bar{V}_\infty)/dt = -(\bar{U} - \bar{V}_\infty)/P \quad (\text{since } \bar{V}_\infty \text{ is constant})$$

which integrates to

$$\bar{U} = \bar{V}_\infty - (\bar{U}_0 - \bar{V}_\infty) \exp(-t/P); \quad (\bar{U}_0 \equiv \bar{U}(t=0)) \quad (3-3)$$

From equation (3-3),  $\bar{U} \rightarrow \bar{V}_\infty$  as  $t \rightarrow \infty$  monotonically, i.e., velocity of the particle relaxes to the flow velocity after a long time. Thus P is the non-dimensional equivalent of the velocity relaxation time ( $\tau_V$ ) characteristic of the particle:

$$P = \tau_V (V_\infty / C)$$
$$\tau_V = \rho^* d^2 / (18\mu) \quad [\text{unit time}] \quad (3-4)$$

Equation (3-4) implies that the larger, heavier particles will take longer time to relax to the flow velocity than the smaller, lighter particles. In the general case of arbitrary flow and  $C_D \neq C_D$  (Stokes), the velocity relaxation time concept is still useful in that a rough order of magnitude estimate of the particle motion in a given flow can be obtained.

### 3.2.2 Scaling of the Trajectory Problem

As was done in the previous section, the trajectory equation (3-1) can be simplified for the case of Stokes' drag law:

$$dU_i/dt = (V_i - U_i)/P - (1-\sigma)gC\delta_{i2}/V_\infty^2 \quad (3-5)$$

Equation (3-5) implies that, neglecting terms due to gravity and buoyancy, the particle trajectory for a specified starting condition is completely determined by the inertia parameter  $P$  for all dynamically similar flows. The only trajectory similarity parameter required is  $P$ , in addition to the usual flow similarity parameter such as the Reynolds and/or Mach number (depending on the degree of flow compressibility). As long as the Stokes' law of drag holds along the trajectory, matching of  $P$  guarantees the trajectory similarity for the same set of initial conditions for all dynamically similar flows. This similarity concept for constant  $P$  breaks down at the limit of the Stokes' law of drag because  $K(R_V)$  is non-linear in  $R_V$ ; its deviation from unity at a point in the trajectory is a measure of the extent to which the drag coefficient differs from the Stokes' law value. Consequently, the trajectory problem cannot be scaled in general due to the trajectory dependent Stokes' parameter,  $K(R_V)$ .

### 3.3 Drag Coefficient for Spherical Particles ( $C_D$ )

The particular form of the drag coefficient used in this study incorporates an analytical form for the standard drag curve and the Cunningham drag correction for molecular slip and compressibility effects:

$$C_D(M, R_V) = C_D^{inc} \cdot (R_V) / G(M/R_V) \quad (3-6)$$

where

$$C_D^{inc} \equiv \text{incompressible sphere drag coefficient}$$

$G(M/R_v) \equiv$  Cunningham drag correction factor

### 3.3.1 Incompressible Sphere Drag Coefficient ( $C_D^{inc.}$ )

There exist some experimental drag data [33,34] on water droplets in sizes well above the millimeter range where the droplets tend to deviate from sphericity. The effects of droplet instability/break-up are pertinent for larger droplets and hence are not considered here.

The deviation of water droplet drag data from that of the standard drag was found to be significant only for droplets of diameters larger than about 1 mm and for Reynolds numbers greater than about 1000. This observation was mainly due to the flattened shape of droplets in the size and Reynolds number range studied in the still air settling speed measurement [33]. In fact, a recent investigation [35] reported that, in both the Navier-Stokes flow analysis and settling speed measurement results, no significant differences in drag larger than the measurement errors were found between the solid and liquid spheres.

Equation used is the integrable form of Putnam [36],

$$C_D^{inc.}(R_v) = C_D^{Stokes}(R_v) \cdot \left(1 + \frac{1}{6} R_v^{2/3}\right) \quad (3-7)$$

which agrees to within about 5% of the standard drag curve in the range,  $0 \leq R_v \leq 1000$ . Comparison of this equation with several other available forms is listed in Appendix C; equation (3-7) is listed as  $C_D$  (Putnam).

### 3.3.2 Cunningham Drag Correction ( $G(M/R_v)$ )

For small droplets less than about 5  $\mu\text{m}$  diameter, reduction in drag can occur because of the molecular slip of air. Whenever the size of the particle becomes comparable to the mean free path of air molecules, this non-continuum effect can be significant. The first attempt to correct for this was made by Millikan in his oil drop experiment. He used the following correction formula to the Stokes' viscous drag for oil droplets:



$$C_D = C_D^{\text{Stokes}} \left[ 1 + (\lambda/d) \cdot (C_1 + C_2 e^{-C_3 d/\lambda}) \right]^{-1} \quad (3-8)$$

where  $\lambda$  is the mean free path of air,  
 $d$  is the particle diameter,  
 $C_1$ ,  $C_2$  and  $C_3$  are empirical constants.

The factor  $\lambda/d$  is also known as the Knudsen number ( $K_n$ ) which can be shown to be proportional to  $M/R_v$  from the kinetic theory of gases [37]:

$$\lambda/d \equiv K_n \propto M/R_v$$

where  $M \equiv$  Mach no. of gas flow relative to the particle.

The form of the correction adapted in this study is due to Calson and Hoglund [38], who proposed the following empirical fit to available experimental data for the ranges  $M \leq 2.0$  and  $R_v \leq 1000$ :

$$G(M/R_v) = A/B \quad (3-9)$$

where

$$A \equiv 1 + (M/R_v) [3.82 + 1.28 \exp(-1.25R_v/M)], \quad (3-10)$$

$$B \equiv 1 + \exp(-.427M^{-4.63} - 3R_v^{-.88}). \quad (3-11)$$

The numerator in equation (3-9),  $A$ , has the same form used by Millikan and only the numerical constants have been modified. This term represents the drag reduction factor to the incompressible drag due to the molecular slip or rarefaction effects.

The denominator,  $B$ , in equation (3-9) is the additional correction to account for the Mach number dependence of the particle drag (compressibility) in continuum flow.

It must be noted that the Cunningham correction, expressed as in equations (3-9), (3-10) and (3-11), must be evaluated at every trajectory step in the flowfield. The relative Mach number, M, can be evaluated from the compressible Bernoulli equation applied to the potential flow velocity:

$$V_{\infty}^2/2 + a_{\infty}^2/(\gamma-1) = \bar{V}^2/2 + a^2/(\gamma-1) \quad (3-12)$$

where  $a \equiv \sqrt{\gamma R T_s}$ ,

$$a_{\infty} \equiv \sqrt{\gamma R T_{s\infty}}$$

Thus,

$$T_s = \frac{\gamma-1}{2\gamma R} [1 - (\bar{V}/V_{\infty})^2] \cdot V_{\infty}^2 + T_{s\infty} \quad (3-13)$$

$$M = |\bar{V}-\bar{U}| \cdot V_{\infty} / \sqrt{\gamma R T_s} \quad (3-14)$$

Substitution of (3-13) into (3-14) gives

$$M = |\bar{V}-\bar{U}| \cdot [(\gamma-1)(1-V^2)/2 + \gamma R T_{s\infty} \cdot V_{\infty}^{-2}]^{-\frac{1}{2}} \quad (3-15)$$

## 4.0 COMPUTATIONAL METHOD

Analytical determination of water droplet impingement efficiency involves calculation of the flowfield about the body and calculation of individual particle trajectories that lead to impingement on the body. The local impingement efficiency ( $\beta$ ) is obtained by computing the impinging surface droplet flux relative to freestream flux as a function of body surface coordinates.

### 4.1 COMPUTATIONAL PROCEDURE

Droplet impingement analysis on the 3-D engine inlet involved the following major steps:

- (1) Bi-cubic parametric description of the inlet surface.
- (2) Potential flow analysis about the inlet.
- (3) Numerical integration of the trajectory equation.
- (4) Calculation of the limiting envelope of trajectories.
- (5) Calculation of  $\beta$  from the intermediate trajectories within the limiting envelope.

The steps involved in the procedure are illustrated in Figure 2.

### 4.2 BI-CUBIC SURFACE PARAMETRIZATION

Any point on a 3-dimensional surface element (patch) can be analytically defined in terms of a set of patch corner boundary conditions through bi-cubic surface parametrization (See Appendix A). Parametrization is complete when all the patch corner boundary conditions (patch boundary matrices) are obtained for the particular system of patches making up the composite patch surface of the inlet. This procedure involves cubic

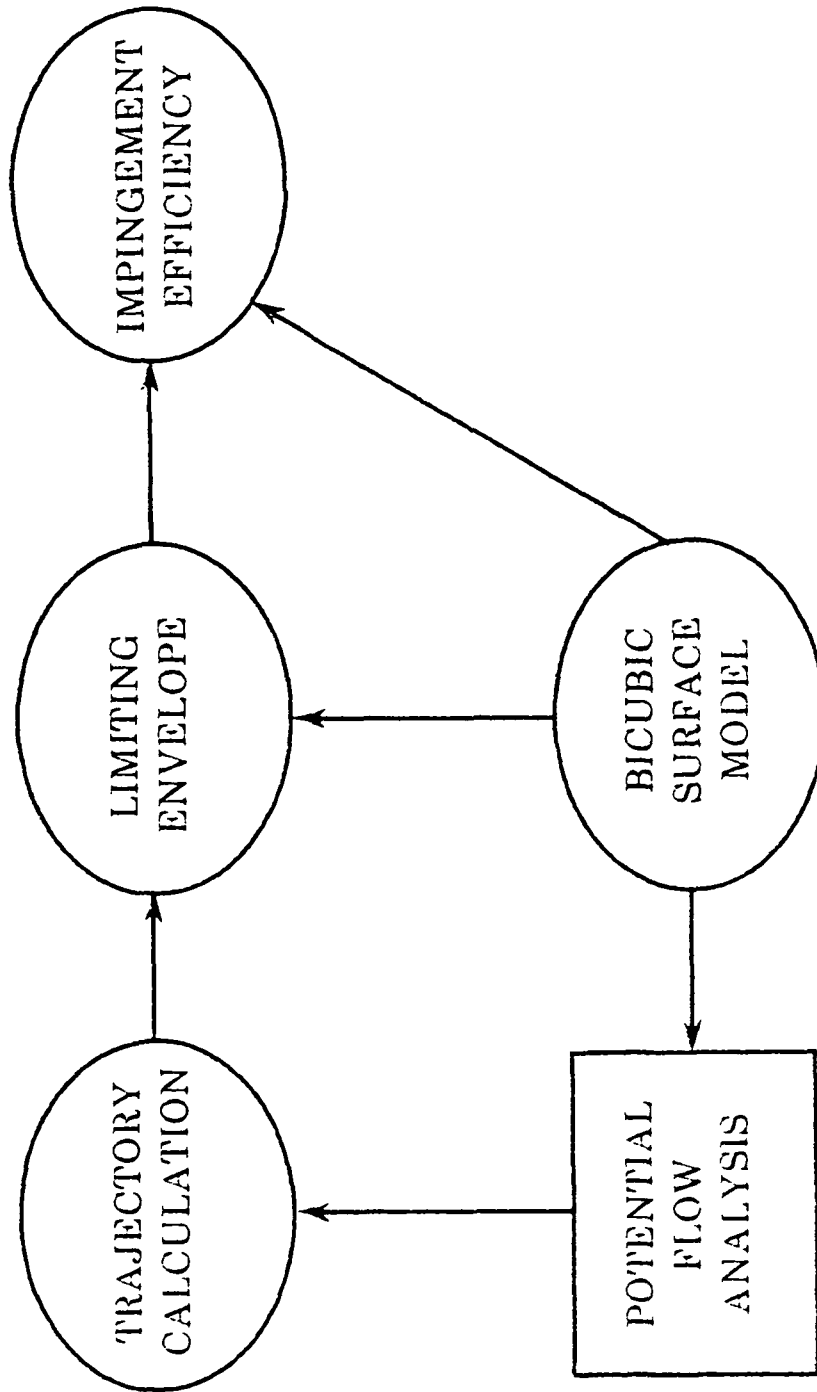


FIGURE 2 - COMPUTATIONAL PROCEDURE

parametric splining of the two sets of curves defining the composite path surface, using the accumulated chord length parametrization and Hermite interpolation schemes [39], to compute the required end point tangent and twist vectors for each curve segment.

The purpose of parametric surface description is two-fold:

- (1) It provides accurate surface normal velocity boundary conditions required for the full potential flow code input.
- (2) Accurate trajectory-surface intersections (impingement points) can be obtained through such parametrization (Appendix A).

A wiremesh diagram of the inlet derived from the bi-cubic patch parametrization is shown later in Figure 15. In the figure, the straight line edges of the wiremesh patches are for illustration only. These do not represent the actual patches whose edges are curved. For the inlet investigated in this study (737-300 prototype inlet), about 600 patches were used to define the surface.

#### 4.3 POTENTIAL FLOW ANALYSIS

Flow velocities are computed by the 3-D full potential code [29] on cylindrical mesh grids (69 x meshes, 49 r meshes, and 16  $\theta$  meshes). The flow code solves the full partial differential equations of compressible transonic potential flow by a finite difference scheme. The convergence acceleration is achieved by the successive line over-relaxation (SLOR) and multigrid techniques [40,41]. The multigrid scheme utilizes four levels of coarse and fine grids about the original mesh chosen such that during iteration cycles flow solutions are passed from one level to another to achieve the extremely fast convergence of flow solutions. For an average engine inlet flow problem involving 50,000 mesh points, the CRAY-1S computing time is only about one minute.

A typical adaptive mesh grid used for engine inlet flow analyses is shown later in Figure D8, Appendix D.

#### 4.3.1 Flow Accuracy (3-D full potential code)

This particular CFD (Computational Fluid Dynamics) computer code used for this investigation is an example of a time-tested code. Since its initial production version developed in the early 1970s, many validation comparisons with experimental data are available, including the NASA wing-pylon-nacelle model (Figure D1, Appendix D). Practically all of the Boeing commercial engine inlets were designed using this code and later correlated with wind tunnel data. However, most of these validations are Boeing proprietary data and cannot be included here. Figures D2 through D7 (NASA wing-pylon-nacelle model) and Figures D9 through D11 (full scale commercial turbofan-engine type inlet) are from NASA CR3514 and these show good agreement with the measured surface Mach number data.

#### 4.3.2 Flow Velocity Interpolation at Trajectory Steps

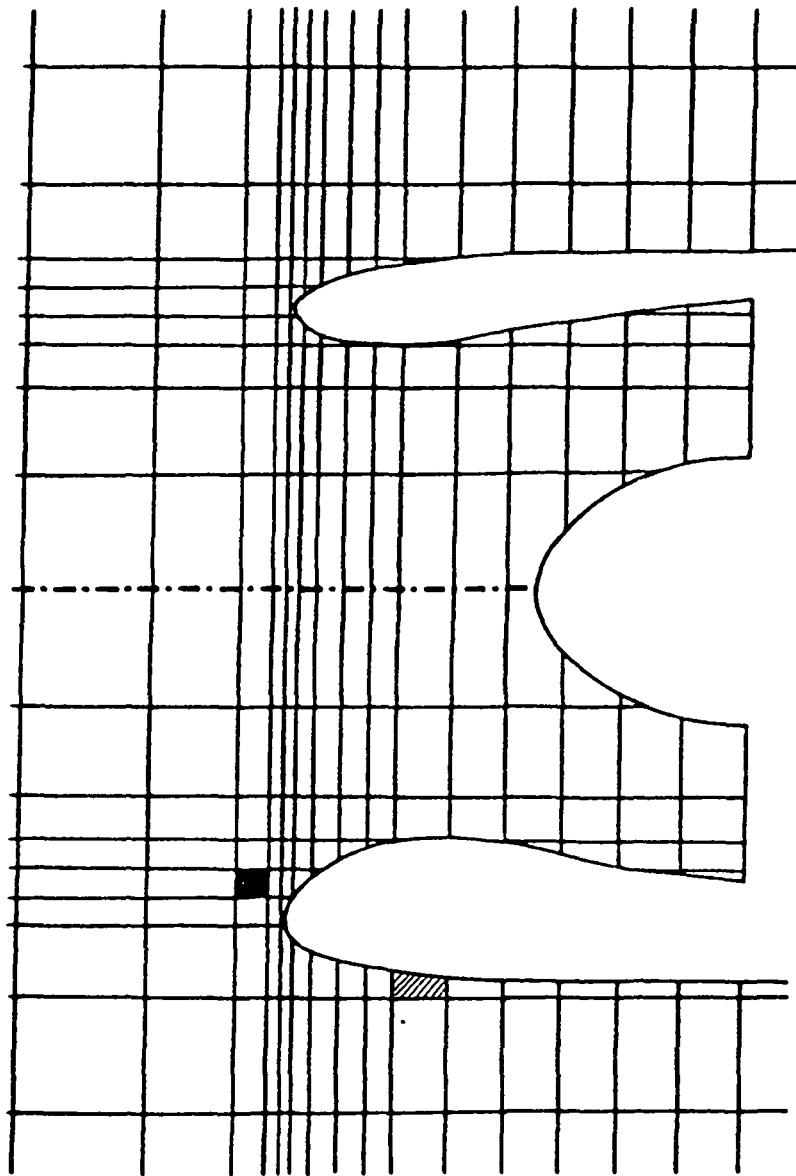
Two different interpolation schemes are employed:

- (1) Volume weighted linear interpolation in field cells.
- (2) Least-square interpolation in surface cells.

Example of the two types of mesh cells are illustrated in Figure 3 showing a typical coarse mesh definition of the flow domain about an engine inlet.

##### 4.3.2.1 Linear Interpolation Formula

Figure 4 depicts a cylindrical field cell with the mesh node origin at  $(i,j,k)$ ;  $i$ ,  $j$  and  $k$  are the  $x$ ,  $r$  and  $\theta$  mesh indices of the node. The flow velocity,  $\bar{V}(x,r,\theta)$ , at an interior point,  $(x,r,\theta)$ , is



■ ≡ field cell

▨ ≡ surface cell

Figure 3 - 2-dimensional Illustration of Field Cell and Surface Cell in a Typical Coarse Computational Mesh Definition

$$\begin{aligned}
\bar{V}(x,r,\theta) = & (\text{Vol})^{-1} \cdot \{ \bar{V}(i,j,k) \cdot w(i+1,j+1,k+1) + \bar{V}(i,j,k+1) \cdot w(i+1,j+1,k) \\
& + \bar{V}(i+1,j,k+1) \cdot w(i,j+1,k) + \bar{V}(i+1,j,k) \cdot w(i,j+1,k+1) \quad (4-1) \\
& + \bar{V}(i,j+1,k) \cdot w(i+1,j,k+1) + \bar{V}(i,j+1,k+1) \cdot w(i+1,j,k) \\
& + \bar{V}(i+1,j+1,k+1) \cdot w(i,j,k) + \bar{V}(i+1,j+1,k) \cdot w(i,j,k+1) \}
\end{aligned}$$

where

$$x_i \leq x \leq x_{i+1}, \quad r_j \leq r \leq r_{j+1}, \quad \theta_k \leq \theta \leq \theta_{k+1},$$

$\bar{V}(i,j,k) \equiv$  Flow velocity at the node  $(i,j,k)$ ,

$$\text{Vol} \quad \equiv (x_{i+1} - x_i) \cdot (r_{j+1}^2 - r_j^2) \cdot (\theta_{k+1} - \theta_k) / 2$$

= total volume of the cell,

$w(i,j,k) \equiv$  volume of the sub-cell whose two corners are  $(x,r,\theta)$  and  $(x_i, r_j, \theta_k)$ .

Explicitly, w's are:

$$w(i,j,k) = (x - x_i) \cdot (r^2 - r_j^2) \cdot (\theta - \theta_k) / 2$$

$$w(i+1,j,k) = (x_{i+1} - x) \cdot (r^2 - r_j^2) \cdot (\theta - \theta_k) / 2$$

$$w(i,j+1,k) = (x - x_i) \cdot (r_{j+1}^2 - r^2) \cdot (\theta - \theta_k) / 2$$

$$w(i,j,k+1) = (x - x_i) \cdot (r^2 - r_j^2) \cdot (\theta_{k+1} - \theta) / 2$$

$$w(i,j+1,k+1) = (x - x_i) \cdot (r_{j+1}^2 - r^2) \cdot (\theta_{k+1} - \theta) / 2$$

$$w(i+1,j+1,k) = (x_{i+1} - x) \cdot (r_{j+1}^2 - r^2) \cdot (\theta - \theta_k) / 2$$

$$w(i+1,j,k+1) = (x_{i+1} - x) \cdot (r^2 - r_j^2) \cdot (\theta_{k+1} - \theta) / 2$$

$$w(i+1,j+1,k+1) = (x_{i+1} - x) \cdot (r_{j+1}^2 - r^2) \cdot (\theta_{k+1} - \theta) / 2$$



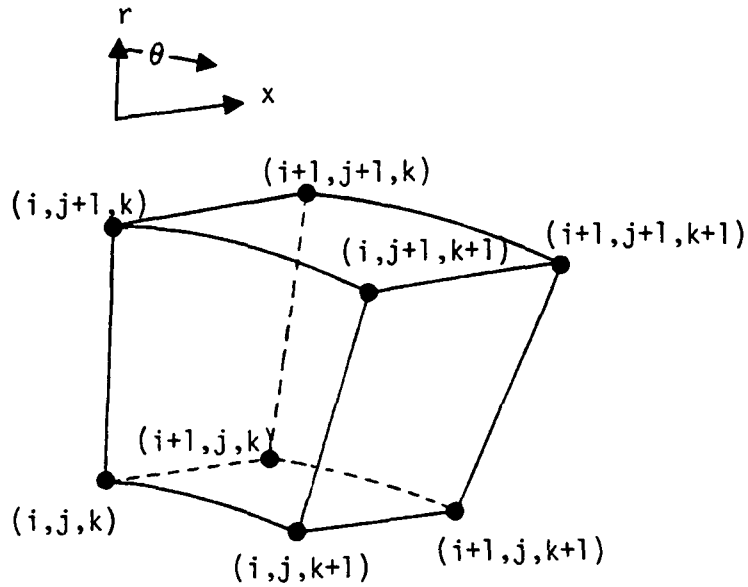


FIGURE 4 - Cylindrical Field Mesh Cell

#### 4.3.2.2 Least-Square Interpolation Formula

When a mesh cell intersects the surface, as in the surface cell shown in Figure 5, interpolation becomes difficult. For example, a straight forward application of the Taylor series formula would require evaluation of the flow gradients with respect to the coordinate variables which depends on the particular way the surface intersects the mesh cell. This is a time consuming process since all the possible cases of surface intersecting cell geometries have to be accounted for.

A different approach is employed in this study, whereby the flow velocity at a desired point is assumed to be a function of the space coordinates and the unknown set of coefficients are to be determined from the least-square fitting of this function at the exterior and mesh-surface intersection points (Figure 5) associated with the surface cell:

$$\bar{V}(x_1, x_2, x_3) = \bar{a}_1 + \bar{a}_2 x_1 + \bar{a}_3 x_2 + \bar{a}_4 x_3 + \bar{a}_5 x_1 x_2 + \bar{a}_6 x_2 x_3 + \bar{a}_7 x_1 x_3 \quad (4-2)$$

This is equivalent to the lowest second order Taylor expansion about the point  $(x_1^0, x_2^0, x_3^0)$  in a vector form:

$$\begin{aligned} \bar{V}(x_1, x_2, x_3) &= \bar{V}(0) + \sum_{i=1}^3 x_i \left( \frac{\partial \bar{V}}{\partial x_i} \right)_0 + \frac{1}{2!} \sum_{i=1}^3 \sum_{j=1}^3 x_i x_j \left( \frac{\partial^2 \bar{V}}{\partial x_i \partial x_j} \right)_0 + 0(3) \\ &= \bar{V}(0) + x_1 \left( \frac{\partial \bar{V}}{\partial x_1} \right)_0 + x_2 \left( \frac{\partial \bar{V}}{\partial x_2} \right)_0 + x_3 \left( \frac{\partial \bar{V}}{\partial x_3} \right)_0 \\ &\quad + 1/2 [ x_1 x_2 \left( \frac{\partial^2 \bar{V}}{\partial x_1 \partial x_2} \right)_0 + x_2 x_3 \left( \frac{\partial^2 \bar{V}}{\partial x_2 \partial x_3} \right)_0 + x_1 x_3 \left( \frac{\partial^2 \bar{V}}{\partial x_1 \partial x_3} \right)_0 ] \\ &\quad + 0(2; \text{higher order}) + 0(3) \end{aligned} \quad (4-3)$$

where (0) and subscript o are taken to mean the quantities evaluated at some arbitrary origin  $(x_1^0, x_2^0, x_3^0)$  in the neighborhood of the surface cell.

Thus the least-square model, equation (4-2), reduces to the lowest second order Taylor expansion of the flow velocity if the following equalities are made:

$$\bar{a}_1 = \bar{V}(0)$$

$$\bar{a}_i = \left( \frac{\partial \bar{V}}{\partial x_i} \right)_0 ; \quad i = 2, 3, 4$$

$$\bar{a}_5 = 1/2 \left( \frac{\partial^2 \bar{V}}{\partial x_1 \partial x_2} \right)_0$$

$$\bar{a}_6 = 1/2 \left( \frac{\partial^2 \bar{V}}{\partial x_2 \partial x_3} \right)_0$$

$$\bar{a}_7 = 1/2 \left( \frac{\partial^2 \bar{V}}{\partial x_1 \partial x_3} \right)_0$$

Equation (4-2) can be put in the matrix form

$$[\xi_1 \ \xi_2 \ \xi_3 \ \xi_4 \ \xi_5 \ \xi_6 \ \xi_7] \begin{bmatrix} \bar{a}_1 \\ \bar{a}_2 \\ \bar{a}_3 \\ \bar{a}_4 \\ \bar{a}_5 \\ \bar{a}_6 \\ \bar{a}_7 \end{bmatrix} = |\bar{V}(x_1, x_2, x_3)| \quad (4-4)$$

where

$$\xi_1 = 1, \ \xi_2 = x_1, \ \xi_3 = x_2, \ \xi_4 = x_3, \ \xi_5 = x_1x_2, \ \xi_6 = x_2x_3 \text{ and } \xi_7 = x_1x_3.$$

For a total of  $n$  ( $n \geq 7$ ) boundary points (exterior mesh and surface-mesh intersection points) defining the surface cell, the successive application of equation (4-4) to the  $n$  boundary points results in:

$$\begin{bmatrix} \xi_{1,1} & \xi_{1,2} & \dots & \dots & \dots & \xi_{1,6} & \xi_{1,7} \\ \xi_{2,1} & \xi_{2,2} & \dots & \dots & \dots & \xi_{2,6} & \xi_{2,7} \\ \xi_{3,1} & \dots & \dots & \dots & \dots & \dots & \dots \\ \dots & \dots & \dots & \dots & \dots & \dots & \dots \\ \dots & \dots & \dots & \dots & \dots & \dots & \dots \\ \dots & \dots & \dots & \dots & \dots & \dots & \dots \\ \dots & \dots & \dots & \dots & \dots & \dots & \dots \\ \xi_{n,1} & \dots & \dots & \dots & \dots & \xi_{n,6} & \xi_{n,7} \end{bmatrix} \begin{bmatrix} \bar{a}_1 \\ \bar{a}_2 \\ \bar{a}_3 \\ \bar{a}_4 \\ \bar{a}_5 \\ \bar{a}_6 \\ \bar{a}_7 \end{bmatrix} = \begin{bmatrix} \bar{V}(1) \\ \bar{V}(2) \\ \dots \\ \dots \\ \dots \\ \dots \\ \bar{V}(n-1) \\ \bar{V}(n) \end{bmatrix} \quad (4-5)$$

This is an over-determined system with 7 unknowns ( $\bar{a}$ 's) and  $n$  equations.  $\bar{V}(k)$  is the known flow velocity at the  $k^{\text{th}}$  boundary point. The matrix  $[\xi(I,J)]$  ( $I=1,2,\dots,n$ ;  $J=1,2,\dots,7$ ) contains the terms involving only the coordinate positions of the  $n$  boundary points defining the surface cell. Equation (4-5) is solved for  $\bar{a}$ 's using Householder's least-square minimization procedure for over-determined system of equations [42]:

$$E = \sum_{l=1}^n \sum_{m=1}^7 (\epsilon_{lm} \bar{a}_m - \bar{v}_l)^2 \quad ; \quad l = 1, 2, \dots, n \\ m = 1, 2, \dots, 7$$

Minimizing E with respect to  $\bar{a}_k$  ( $k = 1, 2, \dots, 7$ ) ;

$$\begin{aligned} 0 &= \frac{\partial E}{\partial \bar{a}_k} = \sum_{l=1}^n \sum_{m=1}^7 \frac{\partial}{\partial \bar{a}_k} [(\epsilon_{lm} \bar{a}_m - \bar{v}_l)^2] \\ &= \sum_{l=1}^n \sum_{m=1}^7 \frac{\partial}{\partial \bar{a}_k} [(\epsilon_{lm} \bar{a}_m - \bar{v}_l)^T \cdot (\epsilon_{lm} \bar{a}_m - \bar{v}_l)] \\ &= 2 \sum_{l=1}^n \sum_{m=1}^7 (\epsilon_{lm} \bar{a}_m - \bar{v}_l)^T \cdot (\epsilon_{lm} \delta_{km}) \\ &= 2 \sum_{l=1}^n (\epsilon_{lk})^T \cdot (\epsilon_{lk} \bar{a}_k - \bar{v}_l) \\ &= 2 \sum_{l=1}^n [(\epsilon_{lk})^T (\epsilon_{lk}) (\bar{a}_k) - (\epsilon_{lk})^T (\bar{v}_l)] \end{aligned}$$

Therefore  $[\epsilon]^T [\epsilon] [A] = [\epsilon]^T [V]$

where  $[\epsilon] \equiv [\epsilon_{lm}]$ ,

$$[A] \equiv [\bar{a}_1 \bar{a}_2 \bar{a}_3 \bar{a}_4 \bar{a}_5 \bar{a}_6 \bar{a}_7]^T,$$

$$[V] \equiv [\bar{v}_1 \bar{v}_2 \dots \bar{v}_{n-1} \bar{v}_n]^T.$$

In some special situations when  $n < 7$ , extra mesh or surface-mesh points (and associated flow velocities) adjacent to the surface cell are used to meet the matrix dimensional requirement,  $n \geq 7$ , in solving for the least-square coefficients  $\{\bar{a}_i\}$ .

To achieve computational efficiency, all of the surface intersecting mesh cells were identified and the least-square coefficients determined and stored in a file prior to the running of the 3-D trajectory code. Each mesh cell is identified, as shown in Figure 5, with the set of mesh node indices,  $(i,j,k)$ , and the associated set of 21 least-square coefficients,  $\{a_m^1(i,j,k)\}$ ,  $l=1,2,3$ ;  $m=1,2,\dots,7$  ( $l$  is the coordinate component index for computing  $V_l$ ). As long as a trajectory position  $(x,r,\theta)$  is inside the surface cell  $(i,j,k)$ , the coefficients  $\{a_m^1(i,j,k)\}$  are used in equation (4-2) to compute the interpolated flow velocity at that position  $(x=x_1, r=x_2, \theta=x_3)$ .

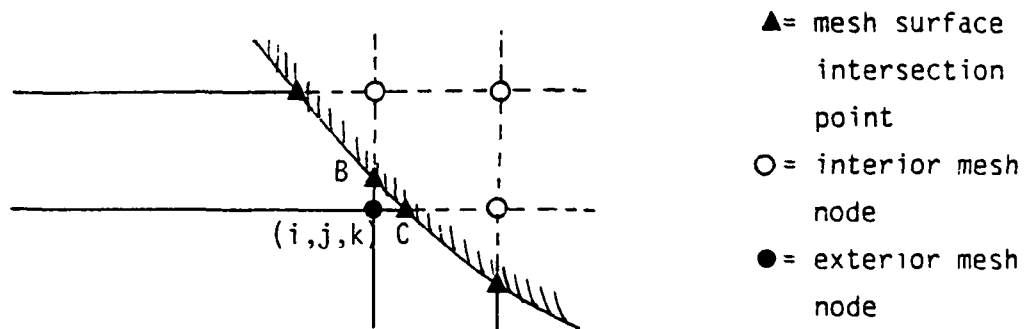


FIGURE 5 - 2-Dimensional Illustration of a Surface Cell Associated with an Exterior Mesh Node  $(i,j,k)$

For the surface cell (Figure 5) associated with the node  $(i,j,k)$ , the least square coefficients  $\{\bar{a}_m^1(i,j,k)\}$  can be obtained from the positions and flow velocities at B, C, and the node  $(i,j,k)$ .

The least-square interpolation formula, equation (4-2), resolves the potential flow velocity near the surface very accurately and smoothly. This is shown in Figure 6 where the comparison is made between the interpolated and the CFD output velocities at the mesh-surface intersections on the lower cowl surface of the 737-300 prototype engine

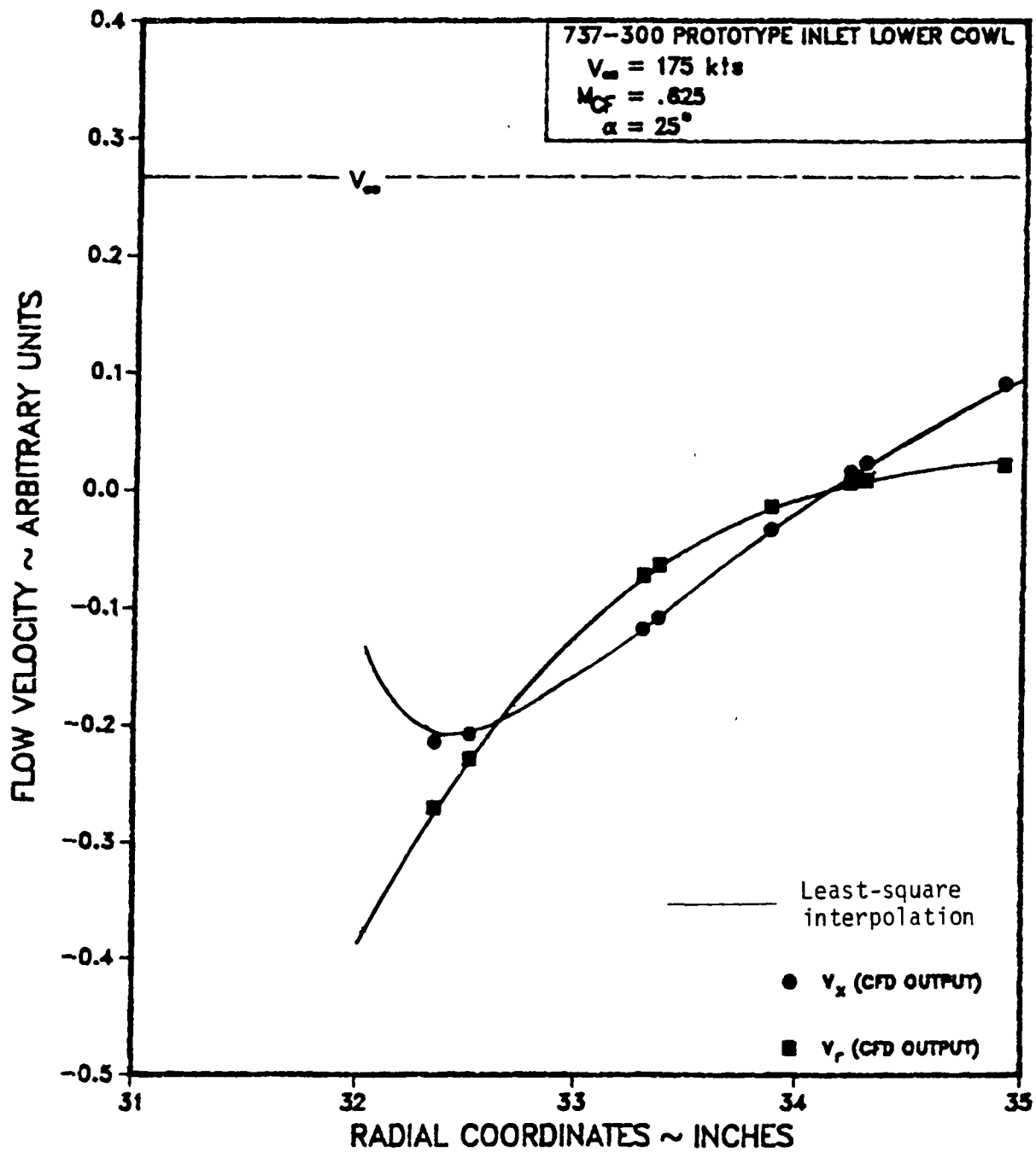


Figure 6 - Lower Cowl Surface Flow Velocities Computed by Least-square Interpolation

inlet. It should be noted that the interpolated curves are obtained not by fitting the CFD output flow velocities at the surface (solid symbols in Figure 6) but from the least-square coefficients of the surface cells involved, by using equation (4-2) continuously along the cowl surface.

#### 4.4 Numerical Integration of the Trajectory Differential Equation

Substituting the drag coefficient, expressed as in equations (3-6), (3-7), (3-9), (3-10) and (3-11), into the trajectory equation (3-1)

$$dU_i/dt = C_D^{\text{Stokes}}(R_V) \cdot R_V \cdot (1 + \frac{1}{6}R_V^{2/3}) \cdot (V_i - U_i) \cdot [24P \cdot G(M/R_V)]^{-1} \quad (4-6)$$

$$- (1-\sigma)g C_{\delta_{i2}} V_{\infty}^{-2}$$

where

$$G(M/R_V) = \frac{1 + (M/R_V)[3.82 + 1.28\exp(-1.25R_V/M)]}{1 + \exp[-.427M^{-4.63} - 3R_V^{-.88}]}$$

$$M = M(\bar{V}, \bar{U}) \text{ as shown in equation (3-15)}$$

$$R_V = R_V(\bar{V}, \bar{U}) \text{ as defined below equation (3-1)}$$

$$\bar{V} = \bar{V}(\bar{x})$$

From the above functional relationships, the R.H.S. of equation (4-6) depends only on the particle position and velocity:

$$d\bar{U}/dt = \bar{F}(\bar{x}, \bar{U})$$

Together with the definition of  $\bar{U}$  as the time derivative of  $\bar{x}$ , we arrive at the following two coupled first order differential equations in time:

$$d\bar{x}/dt = \bar{U}, \quad (4-7)$$

$$d\bar{U}/dt = \bar{F}(\bar{x}, \bar{U}). \quad (4-8)$$

The above represents an initial value problem and thus requires a self-starting type procedure in the numerical integration. The Runge-Kutta method is a self-starting type with high degree of accuracy. One disadvantage is that a large number of function evaluations is involved.

Compared to the same order Runge-Kutta integrator, the Adams predictor-corrector requires one-half the number of function evaluations with comparable accuracy, but is not self-starting.

In this study, a combination of the 4th order Runge-Kutta and Adams predictor-corrector schemes with an automatic stepsize control is used to solve the trajectory equation (4-6). A flow chart of the numerical integration scheme is shown in Figure 7.

#### 4.4.1 Runge-Kutta Scheme (4th order)

The 4th order scheme, accurate to 5th order in Taylor expansion, is used to start or restart the integration process from the initial condition or when the stepsize is changed due to the error control process at the end of an Adams predictor-corrector step.

The coupled first order equations (4-7) and (4-8) take the following Runge-Kutta forms

$$\bar{U}(n+1) = \bar{U}(n) + h \cdot \{\bar{A} + 2\bar{B} + 2\bar{C} + \bar{D}\} / 6 \quad (4-9)$$

$$\bar{x}(n+1) = \bar{x}(n) + h \cdot \{\bar{a} + 2\bar{b} + 2\bar{c} + \bar{d}\} / 6 \quad (4-10)$$

where

$$h = t_{n+1} - t_n, \quad \bar{U}(n) \equiv \bar{U}(t_n), \quad \bar{x}(n) \equiv \bar{x}(t_n)$$

$$\bar{a} = \bar{U}(n), \quad \bar{A} = \bar{F}[\bar{x}(t_n), \bar{U}(t_n)]$$

$$\bar{b} = \bar{a} + h \cdot \bar{A} / 2, \quad \bar{B} = \bar{F}[\bar{x}(t_n) + h \cdot \bar{a} / 2, \bar{b}]$$



$$\bar{c} = \bar{a} + h \cdot (\bar{A} + \bar{B})/4, \quad \bar{C} = \bar{F}[\bar{x}(t_n) + h \cdot (\bar{A} + \bar{b})/4, \bar{c}]$$

$$\bar{d} = \bar{c} + h \cdot \bar{C}/2, \quad \bar{D} = \bar{F}[\bar{x}(t_n) + h \cdot (\bar{A} + \bar{b} + 2\bar{c})/4, \bar{d}]$$

#### 4.4.2 Adams predictor-corrector scheme (4th order)

This scheme predicts and corrects the next time step ( $t_{n+4}$ ) from the three previous Runge-Kutta time steps ( $t_{n+1}$ ,  $t_{n+2}$ ,  $t_{n+3}$ ):

$$\begin{array}{l} \text{Predicted} \\ \text{Corrected} \end{array} \left[ \begin{array}{l} \bar{U}_p(n+4) = \bar{U}(n+3) + h \cdot [-9\bar{F}(n) + 37\bar{F}(n+1) - 59\bar{F}(n+2) + 55\bar{F}(n+3)]/24 \\ \bar{x}_p(n+4) = \bar{x}(n+3) + h \cdot [-9\bar{U}(n) + 37\bar{U}(n+1) - 59\bar{U}(n+2) + 55\bar{U}(n+3)]/24 \\ \bar{U}_c(n+4) = \bar{U}(n+3) + h \cdot [\bar{F}(n+1) - 5\bar{F}(n+2) + 19\bar{F}(n+3) + 9\bar{F}(\bar{x}_p(n+4), \bar{U}_p(n+4))] / 24 \\ \bar{x}_c(n+4) = \bar{x}(n+3) + h \cdot [\bar{U}(n+1) - 5\bar{U}(n+2) + 19\bar{U}(n+3) + 9\bar{U}_p(n+4)] / 24 \end{array} \right.$$

where

$$\bar{F}(n) \equiv \bar{F}[\bar{x}(n), \bar{U}(n)].$$

This procedure is recursive, i.e., as long as the agreement between the predicted and corrected values are within the specified error margin integration proceeds in a step by step manner.

#### 4.4.3 Automatic Stepsize Control

After each predictor-corrector computation, the integration error ( $\epsilon$ ) is checked to determine whether to accept the corrected values and proceed or to reject the step and restart the integration using the Runge-Kutta procedure. The integration error at a particular step is not the truncation error occurred at that step corresponding to the particular choice of numerical scheme, but is the global error of the numerical solution from the true solution at that step. The approach of controlling the truncation error at every step usually involves additional number of function evaluations comparable to those required

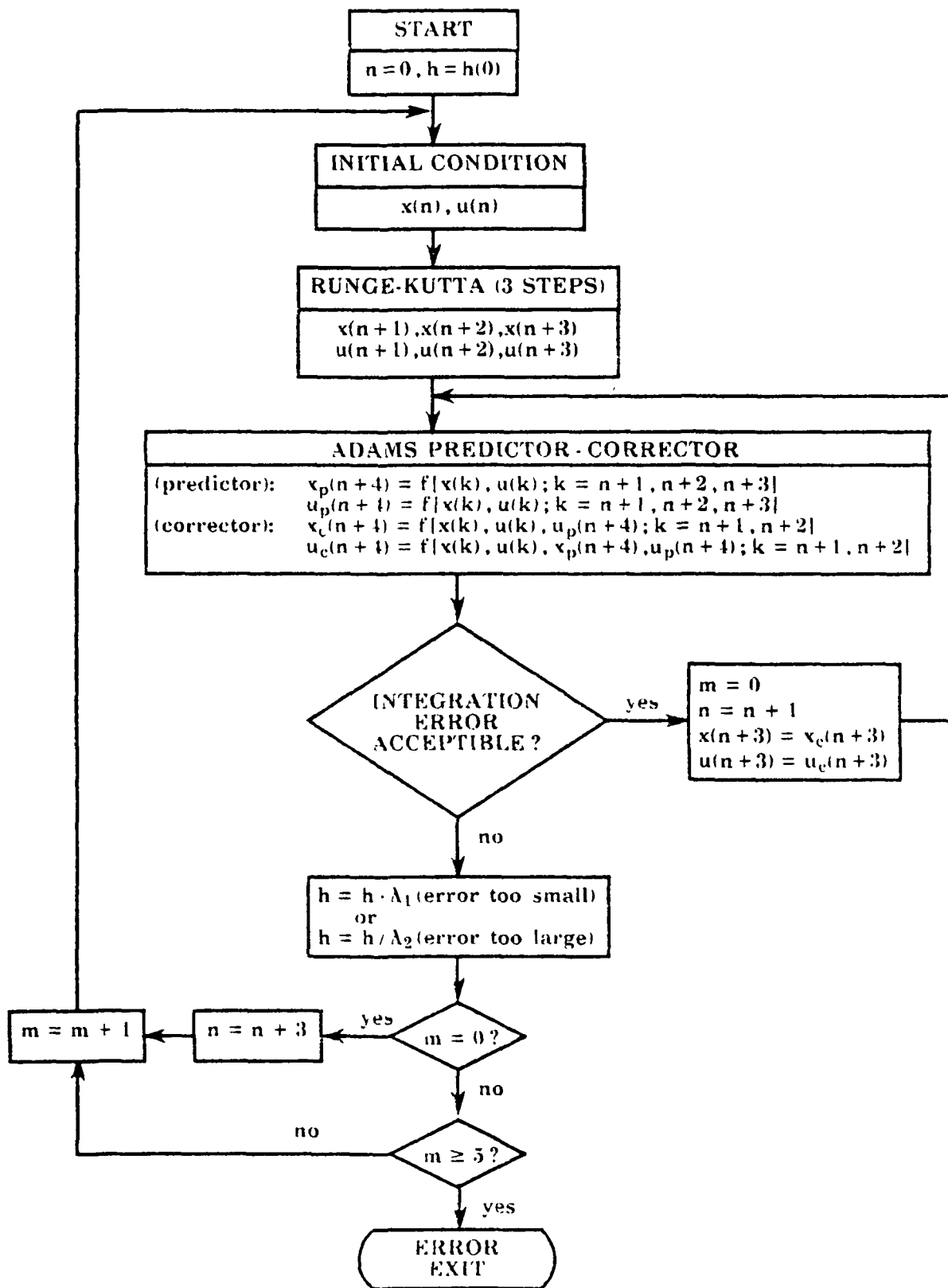


FIGURE 7 - INTEGRATION SCHEME FOR TRAJECTORY COMPUTATION

to integrate the equation, and still does not guarantee satisfactory control of the global numerical error.

The approach adapted here is to use the discrepancy between the predicted and corrected values as a measure of the integration error,  $\epsilon = \epsilon(\bar{U}_C, \bar{U}_p)$ . The two types of error indicating the discrepancy between  $\bar{U}_p$  and  $\bar{U}_C$  are the absolute,  $\epsilon_1(U_C^i - U_p^i)$ , and the relative  $\epsilon_2(U_p^i/U_C^i)$ , errors:

	<u>Situation</u>	Type of <u>Error Preferred</u>	<u>Min. Error ( <math>\epsilon_{min}</math> )</u>	<u>Max. Error ( <math>\epsilon_{max}</math> )</u>
(1)	$ \bar{U}_C ,  \bar{U}_p $ large	relative ( $\epsilon_2$ )	?	0.01(1%)
(2)	$ \bar{U}_C ,  \bar{U}_p $ small	absolute ( $\epsilon_1$ )	?	$\delta V$ (flowfield error)

The error bound on  $\epsilon_1$  must be tied to  $\delta V$ , since the R.H.S. of the differential equation (4-6) depends on  $(\bar{V} - \bar{U})$ ; if  $|\bar{V}|$  is accurate to  $\delta V$ , then the absolute error of  $\bar{U}$  should be of the same order of magnitude. However, if  $\epsilon_1$  is within the flowfield accuracy,  $\epsilon_2$  may be unacceptably large;

$|U_C^i|, |U_p^i|$  may be small (comparable to  $\delta V$ ) but

$|(U_C^i - U_p^i)/U_C^i|$  or  $|1 - |U_p^i/U_C^i||$  may be large.

Thus, the flowfield accuracy ( $\delta V$ ) plays an important role in the error control process.  $\delta V$  for the 3-D inlet flowfield was about 0.001 based on the flow velocities normalized to the Mach number at freestream ( $M_\infty = .267$ ).

Based on the above physical considerations, the following integration error estimate/control scheme is devised:

(1)  $\epsilon_1, \epsilon_2, e_1(i)$  and  $e_2(i)$  initialized to zero ( $i=1,2,3$ )

$$(2) |U_C^i| \leq \delta V ; e_1(i) = |U_C^i - U_P^i| \quad (4-11)$$

$$|U_C^i| > \delta V ; e_2(i) = \text{MAX} \{ |(U_C^i - U_P^i)/U_C^i|, |1 - |U_P^i/U_C^i|| \} \quad (4-12)$$

( $i=1,2,3$ )

$$\epsilon_1 = \text{MAX} (\epsilon_1, \text{MAX} [e_1(1), e_1(2), e_1(3)])$$

$$\epsilon_2 = \text{MAX} (\epsilon_2, \text{MAX} [e_2(1), e_2(2), e_2(3)])$$

(3) case 1 ( $\epsilon_1 \leq 2 \delta V$ );

$\epsilon_{\min} \leq \epsilon = \epsilon_2 \leq \epsilon_{\max} \rightarrow$  successful predictor-corrector step

$\epsilon = \epsilon_2 < \epsilon_{\min} \rightarrow$  rejected,  $h' = h \cdot \lambda_1$  (increase stepsize)

$\epsilon = \epsilon_2 > \epsilon_{\max} \rightarrow$  rejected,  $h' = h/\lambda_2$  (decrease stepsize)

case 2 ( $\epsilon_1 > 2 \delta V$ )  $\rightarrow$  rejected,  $h' = h/\lambda_2$  (decrease stepsize)

Thus, the error control scheme first checks to see if the maximum absolute error ( $\epsilon_1$ ) of ( $\bar{U}_C, \bar{U}_P$ ) components is within the flow resolution. If it is (case 1), then it checks whether the maximum relative error ( $\epsilon_2$ ) is within the set relative error margin ( $\epsilon_{\min}, \epsilon_{\max}$ ). Otherwise (case 2), the step is rejected, and stepsize decreased to restart the integration process using the Runge-Kutta procedure.

For the 3-0 inlet trajectory analysis, the following error control parameters are used:

$$\begin{aligned} \delta V &= 0.001 \\ \epsilon_{\min} &= 0.001 \quad , \quad \epsilon_{\max} = 0.01 \\ \lambda_1 &= 1.5 \quad , \quad \lambda_2 = 1.87 \end{aligned}$$

Integral or integer fractional relationship between  $\lambda_1$  and  $\lambda_2$  is to be avoided because of the danger of repetitive stepsize changes.

#### 4.5 Calculation of the Limiting Envelope of Trajectories

The limiting envelope of droplet trajectories is the surface traced out by the inner and outer tangent trajectories (Figure 8). For droplets starting at freestream constant-x plane with the same initial velocity as  $\bar{V}_\infty$ , the bounding radial starting positions,  $(r_{o\min}(\theta_o), r_{o\max}(\theta_o))$ , are searched for each selected value of  $\theta_o$  which results in a pair of tangent trajectories. Repeating this process by sweeping  $\theta_o$  with selected increments, the freestream impingement bound,  $\Gamma(r_{o\min}(\theta_o), r_{o\max}(\theta_o))$ , is determined.  $\Gamma$  represents the cross-section of the impinging envelope of trajectories at the freestream constant-x plane.

A tangent trajectory is determined via a trial and error process. Along a radial line ( $\theta_o$  ray) on the constant-x freestream plane, a pair of radial starting positions  $r_{o1}$  and  $r_{o2}$  are searched that result in impinging and non-impinging trajectories, respectively, to the engine cowl surface. Once  $r_{o1}$  and  $r_{o2}$  are found, an iterative bi-section procedure is applied until a set tolerance is met:

- (1)  $r_{o1}$  (impinging),  $r_{o2}$  (non-impinging);  $(x_o, \theta_o, \bar{U}_o = \bar{V}_\infty)$  fixed
- (2)  $r_o = (r_{o1} + r_{o2})/2$  (new guess)
- (3)  $|r_o - r_{o1}| \leq \text{TOL?}$   $\left[ \begin{array}{l} - \frac{Y}{N} \frac{E}{O} \frac{S}{-} \\ \longrightarrow (-1) \end{array} \right] \text{ (tangent trajectory found)} \longrightarrow \text{EXIT}$

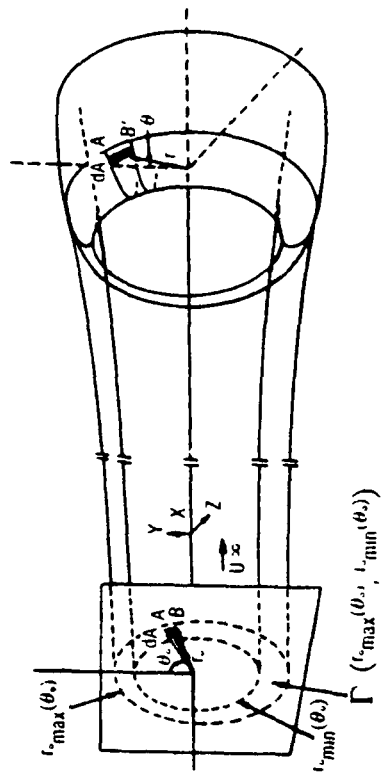


Figure 8 - Limiting Envelope of Trajectories

(4) compute trajectory

until particle  $\left\{ \begin{array}{l} \text{impinges: set } r_{o1} = r_o \longrightarrow (2) \\ \text{reaches computational} \\ \text{boundary without impinging} \longrightarrow (5) \end{array} \right.$

(5)  $r_o = r_{o2} \longrightarrow (2)$

If  $r_{o2}$  had the trajectory end point radial position (at the fan face, the downstream computational boundary) within the fan radius,

$r_{o\min} = r_{o1}$ . Otherwise,  $r_{o\max} = r_{o1}$ .

Steps (1) thru (5) are performed for  $\theta_o(n) = \theta_o(n-1) + \Delta\theta$ ,

$n = 1, 2, \dots, n_{\max}$ ;  $n_{\max} = 30$ ,  $\theta_o(0) = 0^\circ$  and  $\Delta\theta = 180^\circ/n_{\max}$ .

The  $2(n_{\max}+1)$  tangent trajectories found this way represent the limiting envelope of trajectories, whose impingement points on the cowl surface now represent the limiting impact points. Any trajectories which start at  $(x_o, r_{o\min} \leq r_o \leq r_{o\max}, \theta_o)$  will impinge on the surface region enclosed by the boundary curves defined by the inner and outer limiting impact points.

#### 4.6 Calculation of the Local Droplet Impingement Efficiency ( $\beta$ )

One can now run a number of trajectories starting at an array of points within the region,  $\Gamma(r_{o\min}(\theta_o), r_{o\max}(\theta_o))$ , in an orderly fashion to obtain the array of impingement points on the cowl surface (Figure 9). Let  $\bar{x}_o(I, J)$  and  $\bar{x}_m(I, J)$  denote the array of starting points from  $\Gamma(r_{o\min}(\theta_o), r_{o\max}(\theta_o))$  and the corresponding impingement point array on the surface, respectively.

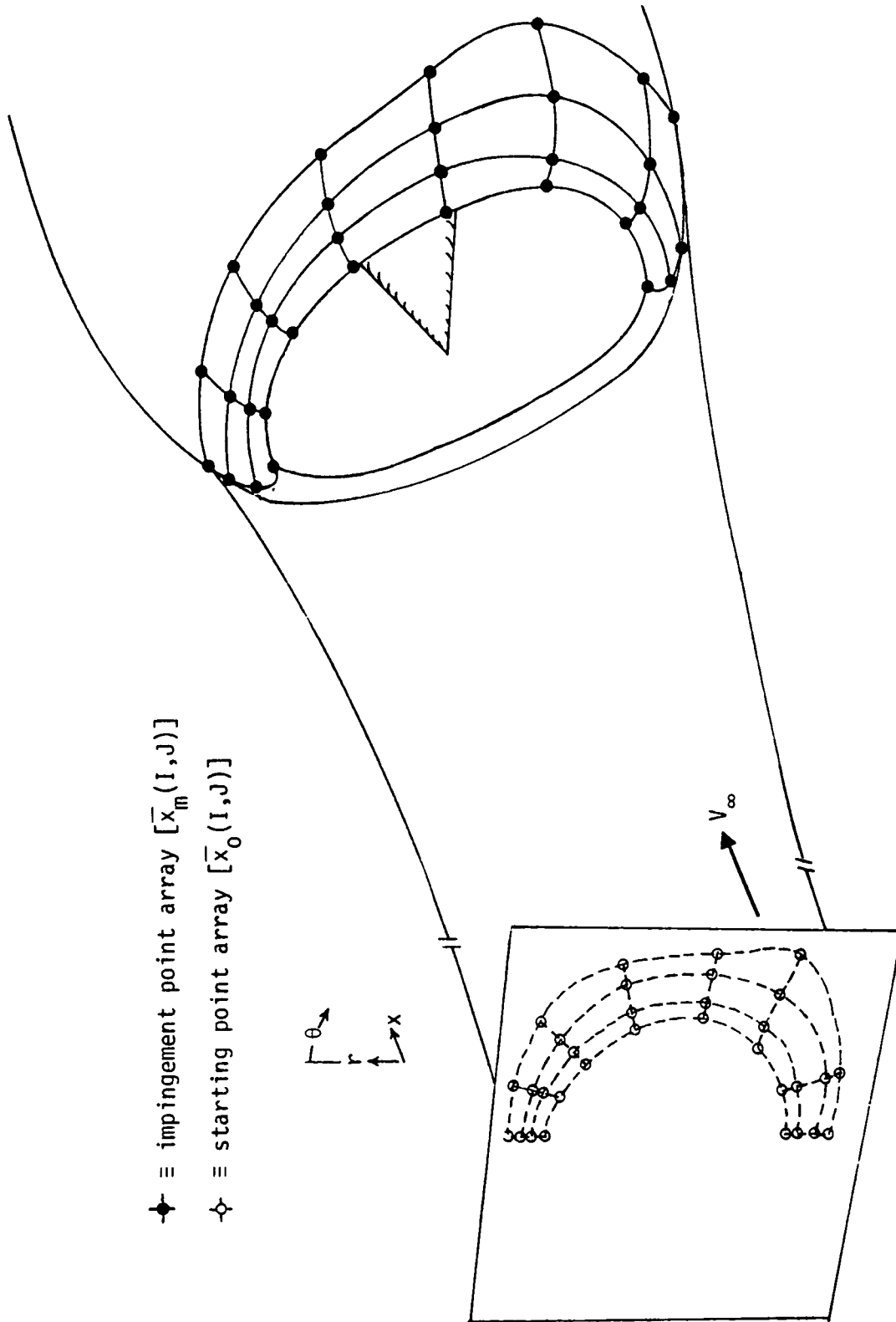


Figure 9 - Illustration of the Starting Point Array  $[\bar{x}_0(I,J)]$  and Impingement Point Array  $[\bar{x}_m(I,J)]$



We can define the associated area elements;

$a_o(i,j) \equiv$  area of the element formed by the four corner points,  
 $\{\bar{x}_o(I,J), \bar{x}_o(I,J+1), \bar{x}_o(I+1,J), \bar{x}_o(I+1,J+1)\}$   
 at the freestream constant-x plane,

$a_m(i,j) \equiv$  area of the element formed by the four corner points,  
 $\{\bar{x}_m(I,J), \bar{x}_m(I,J+1), \bar{x}_m(I+1,J), \bar{x}_m(I+1,J+1)\}$   
 at the surface,

where  $I = 1,2,\dots, \text{IMAX}$  (IMAX = nmax)

$J = 1,2,\dots, \text{JMAX}$  (JMAX = nmax/2)

$i = 1,2,\dots, \text{IMAX}-1$

$j = 1,2,\dots, \text{JMAX}-1$

The local impingement efficiency ( $\beta$ ), as in equation (1.0), can be approximated by

$$\beta(\bar{x}_c(i,j)) \approx \frac{\bar{n}_\infty \cdot \hat{i} a_o(i,j)}{a_m(i,j)} \quad (4-13)$$

where  $\bar{x}_c(i,j) \equiv$  centroid location of  $a_m(i,j)$ .

The unit direction vector,  $\bar{n}_\infty$ , of  $\bar{V}_\infty$  for the general engine inlet attitude having a set of pitch ( $\alpha$ ), roll ( $\phi$ ) and yaw ( $\psi$ ) angles with respect to the space coordinate axes can be obtained from the Euler rotation matrix applied to the unit vector obtained when the engine inlet body axes and the space axes coincide:

$$\begin{aligned}
& [n_{\infty}(1) \ n_{\infty}(2) \ n_{\infty}(3)]^T \\
& = \begin{bmatrix} \cos\alpha\cos\psi & \sin\alpha\sin\phi\cos\psi - \cos\phi\sin\psi & \sin\alpha\cos\phi\cos\psi + \sin\phi\sin\psi \\ \cos\alpha\sin\psi & \sin\alpha\sin\phi\sin\psi + \cos\phi\cos\psi & \sin\alpha\cos\phi\sin\psi - \sin\phi\cos\psi \\ -\sin\alpha & \cos\alpha\sin\phi & \cos\alpha\cos\phi \end{bmatrix} \begin{bmatrix} 1 \\ 0 \\ 0 \end{bmatrix} \\
& = \begin{bmatrix} \cos\alpha\cos\psi \\ \cos\alpha\sin\psi \\ -\sin\alpha \end{bmatrix} \tag{4-14}
\end{aligned}$$

Substituting (4-14) into (4-13),

$$\beta(\bar{x}_c(i,j)) = \cos\alpha\cos\psi a_o(i,j)/a_m(i,j) \tag{4-15}$$

Equation (4-15) means that for a general orientation of the body with respect to the space coordinate system, we can choose the constant-x plane at the freestream as the plane of trajectory starting positions to compute the flux ratios. The projection of the freestream flux along the direction of  $\bar{V}_{\infty}$  is accounted for by the factor  $(\cos\alpha\cos\psi)$  involving the pitch and yaw angles only.

Thus the grid of  $\beta$  values can be computed numerically, using equation (4-15), at the centroids of the impingement point grid,  $\bar{x}_m(I,J)$ . Unless the grids are dense, i.e., large IMAX and JMAX, the  $\beta$  distribution on the surface defined at  $\bar{x}_c(i,j)$ 's will not be smooth. Also,  $\bar{x}_c(i,j)$ 's are not particularly useful in organizing and presenting the computed  $\beta$  distribution on the surface because of its point function definition of  $\beta$  on 3-D surfaces.

In order to obtain a more accurate  $\beta$  distribution and to express it as a function of the surface arc length(s) along a set of constant- $\theta$  cowl contours, the following had to be done:

- (1) Select a desired  $\theta$  (constant- $\theta$  cowl contour along which  $\beta$  is to be determined)
- (2) From the coarse impingement centroid grid,  $\bar{x}_c(i,j)$ , and the corresponding  $\bar{x}_o(I,J)$  grid computed, find the  $I_1$  and  $I_2$  ( $\theta$ -ray indices) that result in the condition

$$\theta_c(I_1, J) \leq \theta \leq \theta_c(I_2, J), \quad J = 1, 2, \dots, JMAX$$

- (3) Determine KMAX:  $[\theta_o(I_2) - \theta_o(I_1)]/KMAX = 1^\circ$

- (4) Find tangent trajectories for the rays,

$$\theta_o(K) = \theta(I_1) + K; \quad K = 1, 2, \dots, KMAX-1$$



- (5) Compute  $a_o(k,j)$ ,  $a_m(k,j)$ ,  $\beta(x_c(k,j))$ ;  $k = 1, 2, \dots, KMAX-2$   
 $j = 1, 2, \dots, JMAX-1$

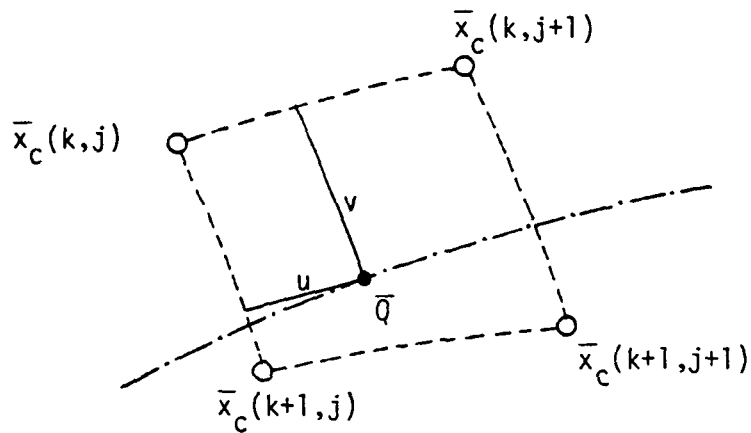
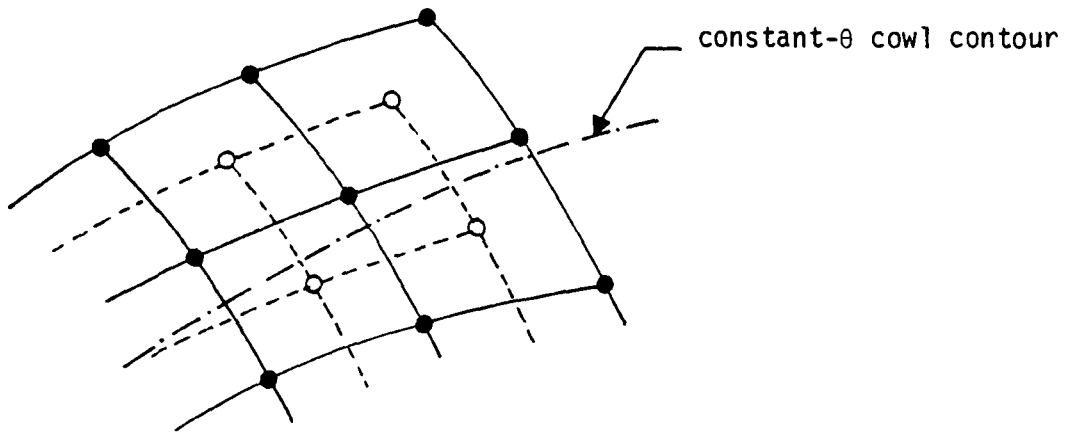
Steps (1) thru (5) are repeated for all other  $\theta$ 's desired.

Thus a much finer grid definition of  $\beta$  is obtained that encloses a particular constant- $\theta$  cowl contour desired. By parametric cubic splining of the contour curve, the arc length (s) of a point on the curve can be computed with respect to the cowl hi-lite position:

$$(s = 0 \text{ is the hi-lite; } s+ \equiv \text{ outside; } s- \equiv \text{ inside}).$$

Moving the points along the cowl contour with selected  $\Delta s$ ,  $\beta$  at a point along the contour can be interpolated from the surface grid cell corner values  $\{\beta(\bar{x}_c(k,j)), \beta(\bar{x}_c(k,j+1)), \beta(\bar{x}_c(k+1,j)), \beta(\bar{x}_c(k+1,j+1))\}$  of the centroid grid that encloses the point in question (Figure 10).

-  impingement point grid,  $\bar{x}_m(I,J)$
-  impingement centroid grid,  $\bar{x}_c(i,j)$



$$\beta(\bar{Q}) \cong \beta(\bar{x}_c(k+1,j+1)) \cdot u \cdot v + \beta(\bar{x}_c(k,j+1)) \cdot u \cdot (1-v) + \beta(\bar{x}_c(k,j)) \cdot (1-u) \cdot (1-v) + \beta(\bar{x}_c(k+1,j)) \cdot (1-u) \cdot v$$

Figure 10 - Illustration of the Centroid Impingement Grid  $[\bar{x}_c(i,j)]$  and  $\beta$  Interpolation

#### 4.7 Method for Solid Particles

Most of the assumptions involved in the trajectory model are valid also for analyzing solid particles such as sand grains. One exception is the assumption of spherical shape - sand particles come in all shapes (irregular). If sand particles are characterized in terms of mass, however, one can still consider the shape to be spherical with an effective diameter characterized by their settling behavior in still air such as the terminal velocity and range. Stokes' diameter, for example, is the effective diameter of an equivalent spherical particle having the same mass and terminal velocity, based on the Stokes' drag, as the actual particle. Available data on sand particles of varying shapes [43,44] indicate that, as long as the size is not too large (<1mm), the settling behavior is about the same for particles having similar masses.

The other consideration is the impact behavior - solid particles will bounce off the surface of impact. Shape of the particle will affect the bounce kinematics in a complicated way. Detailed analysis of such behavior is not worth pursuing, except to say that it will involve analyses of statistical nature. Some experimental data [45] are available that characterize the average behavior of solid particle kinematics at metallic surfaces of impact.

The controlling kinematic parameter is the resiliency coefficients,  $r_n$  and  $r_t$ , relating the normal ( $\bar{U}_{n2}$ ) and tangential ( $\bar{U}_{t2}$ ) particle velocities after the impact to those before impact,  $\bar{U}_{n1}$  and  $\bar{U}_{t1}$ :

$$\bar{U}_{n2} = -r_n \bar{U}_{n1} \quad (4-16)$$

$$\bar{U}_{t2} = r_t \bar{U}_{t1}$$

The normal and tangential components of  $\bar{U}_1$  are

$$\bar{U}_{n1} = \bar{n}(\bar{U}_1 \cdot \bar{n}) \quad (4-17)$$

$$\bar{U}_{t1} = \bar{n} \times (\bar{U}_1 \times \bar{n})$$

where  $\bar{n}$   $\equiv$  unit normal vector at the impact point (pointing outward from the surface)

Combining (4-16) and (4-17),

$$\begin{aligned}\bar{U}_{n2} &= -r_n \bar{n} (\bar{U}_1 \cdot \bar{n}) \\ \bar{U}_{t2} &= r_t \bar{n} \times (\bar{U}_1 \times \bar{n}) \\ \bar{U}_2 &= \bar{U}_{n2} + \bar{U}_{t2} = r_t \bar{n} \times (\bar{U}_1 \times \bar{n}) - r_n \bar{n} (\bar{U}_1 \cdot \bar{n})\end{aligned}\quad (4-18)$$

With known values of the resiliency coefficients, the particle velocity immediately after impact ( $\bar{U}_2$ ) can be determined from equation (4-18). In the numerical integration of the trajectory equation, incorporation of the particle bounce mechanism amounts to restarting the integration process with the renewed initial condition,  $(\bar{x}_m, \bar{U}_2)$ , at the point of impact,  $(\bar{x}_m)$ .

The impact point position ( $\bar{x}_m$ ) and the unit normal ( $\bar{n}$ ) are computed as described in the trajectory-bi-cubic patch intersection algorithm (Appendix A).

Some available experimental data [45] indicate that the resiliency coefficients are functions of the impact incident angle,  $\gamma_m$ , as well as the incident particle velocity magnitude,  $|\bar{U}_1|$ ;

$$\begin{aligned}r_n &= r_n(|\bar{U}_1|, \gamma_m) \\ r_t &= r_t(|\bar{U}_1|, \gamma_m)\end{aligned}$$

More research work in the measurement of these parameters are required in order to obtain an adequate empirical kinematic model for sand particles.

## 5.0 RESULTS AND DISCUSSIONS

The basic numerical integration scheme of solving 3-D particle trajectories in potential flow of air was first checked by analyzing the water droplet impingement problem on a spherical body. This task was performed for a number of reasons:

- (1) Availability of the well documented NACA wind tunnel impingement data [11].
- (2) Well known incompressible potential flow solution in analytical form suitable for speedy code implementation.
- (3) Trajectory-surface intersection is easy to compute on the body.
- (4)  $\beta$  computation on the body is simple due to its axisymmetry.

Having gained confidence from the axisymmetric analysis, the numerical scheme for a full-fledged 3-D impingement analysis was worked out, incorporating much of the code developed for the axisymmetric problem.

### 5.1 ANALYSIS OF DROPLET IMPINGEMENT ON A SPHERE

The potential flow velocity,  $\bar{V}$ , can be expressed in terms of the Cartesian coordinates,  $(x,y,z)$ :

$$\bar{V}(x,y,z) = \left[ 1 + \frac{1}{2}r^{-3}(1-3x^2r^{-2}), -\frac{3}{2}xyr^{-5}, \frac{3}{2}xzr^{-5} \right] \quad (5-1)$$

where  $r^2 \equiv x^2 + y^2 + z^2,$

$$(x,y,z) \equiv (X,Y,Z)/R = \text{non-dimensional field point}$$

$$R = \text{radius of sphere located at } (0,0,0)$$

The intersection between a trajectory segment,  $\bar{T}(w)$ , and the surface of sphere,  $x^2+y^2+z^2 = 1$ , is obtained by solving

$$\left. \begin{aligned} \bar{T}(w) &= \bar{p} + \bar{\xi}Lw \\ 1 &= x^2+y^2+z^2 \end{aligned} \right\} \Rightarrow \sum_{i=1}^3 (p_i + \xi_i Lw)^2 = 1 \quad (5-2)$$

which is quadratic in  $w$  ( $w, L, \bar{p}$  and  $\bar{\xi}$  are defined as in equation (A-34), Appendix A).

Calculation of the limiting envelope of trajectories follows the same procedure described in Section 4.5, except that the scan for  $\theta$  rays is not required due to the axisymmetry of the problem. However, several trajectories having different  $\theta$  starting values were checked to verify the axisymmetry in computed trajectories.

The local impingement efficiency ( $\beta$ ) takes the following simple analytic form (Figure 11):

$$\beta(w) = r_0 dr_0 / (r ds) = - d[r_0^2/2] / d[\cos w] \quad (5-3)$$

where  $r_0 = x_0^2 + y_0^2 + z_0^2$ ; freestream starting radial position of an impinging trajectory (dimensionless with  $R$ ),

$w = s/R$ ; angle subtended by the impingement point at the origin (center of sphere).

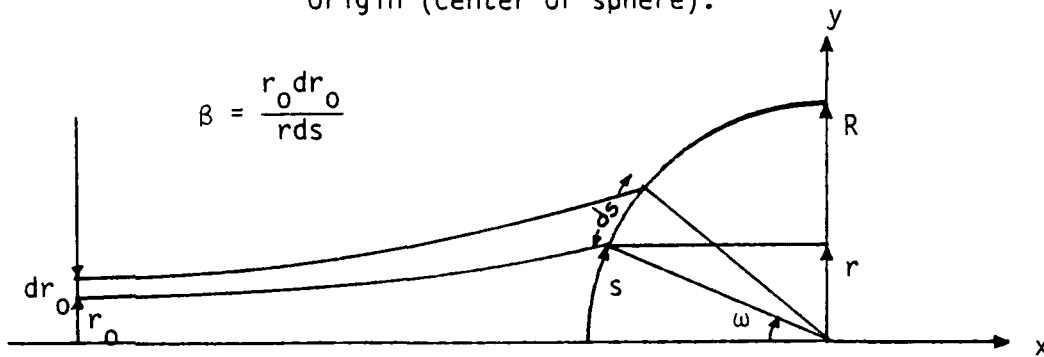


FIGURE 11 - Illustration of  $\beta$  for an Axisymmetric Geometry



Using the definition,  $\omega = s/R$ , equation (5-3) is expressed in terms of the dimensionless arc length,  $s/R$ :

$$B(s/R) = -d\{r_0^2/2\}/d[\cos(s/R)] \quad (5-4)$$

For a number of impinging droplet trajectories ( $i=1,2,\dots,n$ ) equation (5-4) can be evaluated by a cubic spline of  $\{(r_0^2/2)_i\}$  as a function of  $\{\cos(s/R)_i\}$ . The cubic spline derivatives thus obtained determine  $B(s/R)$ .

#### 5.1.1 Langmuir-0 Tunnel Droplet Size Distribution

The numerical procedure was carried out utilizing the accepted tunnel droplet size distribution due to Langmuir [17]. This distribution is a discretized plot of the cumulative LWC fraction versus the seven droplet sizes normalized to the mean volumetric diameter (MVD), as shown in Figure 12.

For a tunnel cloud condition of a particular MVD, calculation of  $B$  involves weighting according to the multi-droplet size distribution:

$$B(s/R) = \sum_{i=1}^7 c_i \beta_i(s/R) \quad (5-5)$$

where  $\beta_i$  is the local impingement efficiency due to the droplets of diameter group  $d_i$ ,  $c_i$  is the fraction of the total LWC contributed by droplets in the diameter group  $d_i$ .

#### 5.1.2 Results

The following tunnel condition was used in the computation in order to compare with the NACA test results:

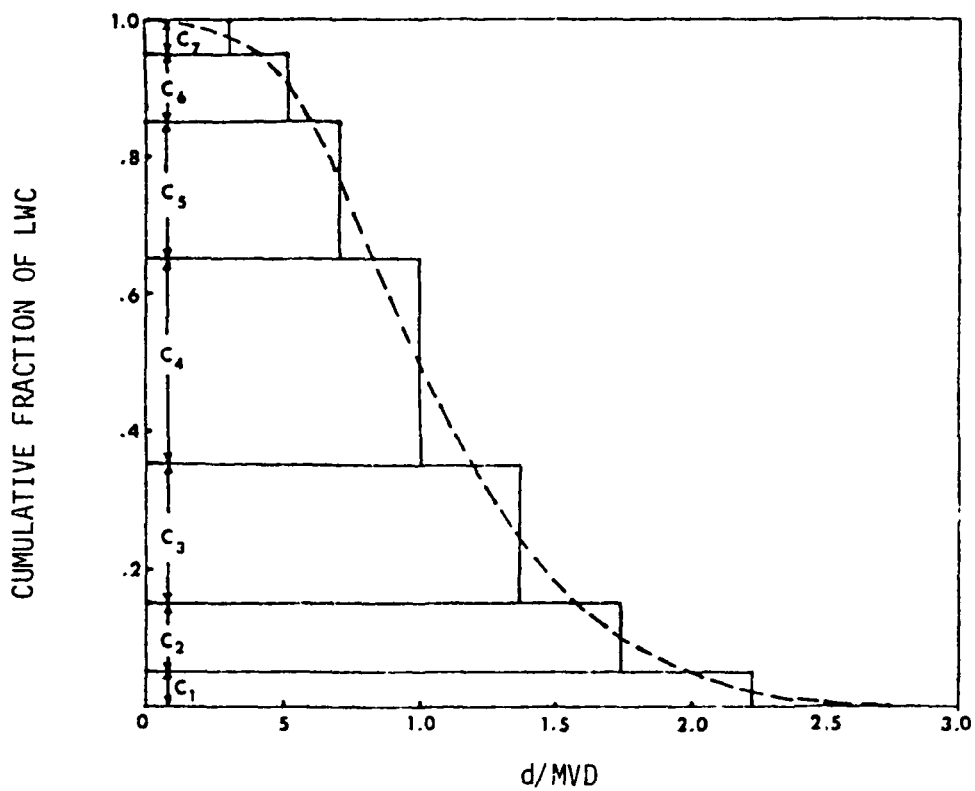


FIGURE 12 - LANGMUIR - D MULTI-DROPLET SIZE DISTRIBUTION

R (sphere radius)	=	9 inches
$V_{\infty}$	=	157 kts
$P_{S\infty}$	=	28 in.Hg
$T_{S\infty}$	=	50 <sup>0</sup> F
MVD	=	11.5 and 14.7 $\mu$ m

A plot of a typical water droplet trajectory is shown in Figure 13 for a 14.7  $\mu$ m diameter droplet. Also shown are the two potential flow streamlines (freestream starting position of the droplet trajectory was identical to that of the upper streamline). The droplet trajectory exhibits the inertial behavior through its departure from the high curvature portions of the upper streamline.

Figure 14 shows a comparison of computed and test data of  $\beta$  vs.  $s/R$  for the two MVD tunnel clouds. Computed results are in good agreement with the experimental data, well within the reported experimental errors of 10% in LWC and 6% in MVD for the tunnel clouds measured.

The significance of the Cunningham drag correction is indicated by the closer agreement, near the flow stagnation region, between the computed and test  $\beta$  values. This observed trend is understood in terms of the increased droplet impingement by the smaller droplet size population of the Langmuir-D droplet spectra, resulting from the appreciable Cunningham drag reduction for these droplets. The impinging droplet flux due to smaller droplets is more localized near the stagnation region than in the case of larger droplets because of the differences in their inertia.

## 5.2 ANALYSIS OF DROPLET IMPINGEMENT ON A 3-D ENGINE INLET

Impingement analysis on the 737-300 prototype inlet was performed for the following flight conditions:

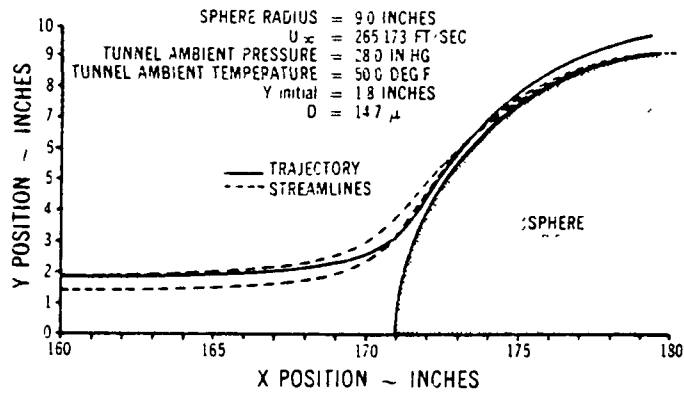


Figure 13 - Droplet Trajectory and Streamlines; Sphere

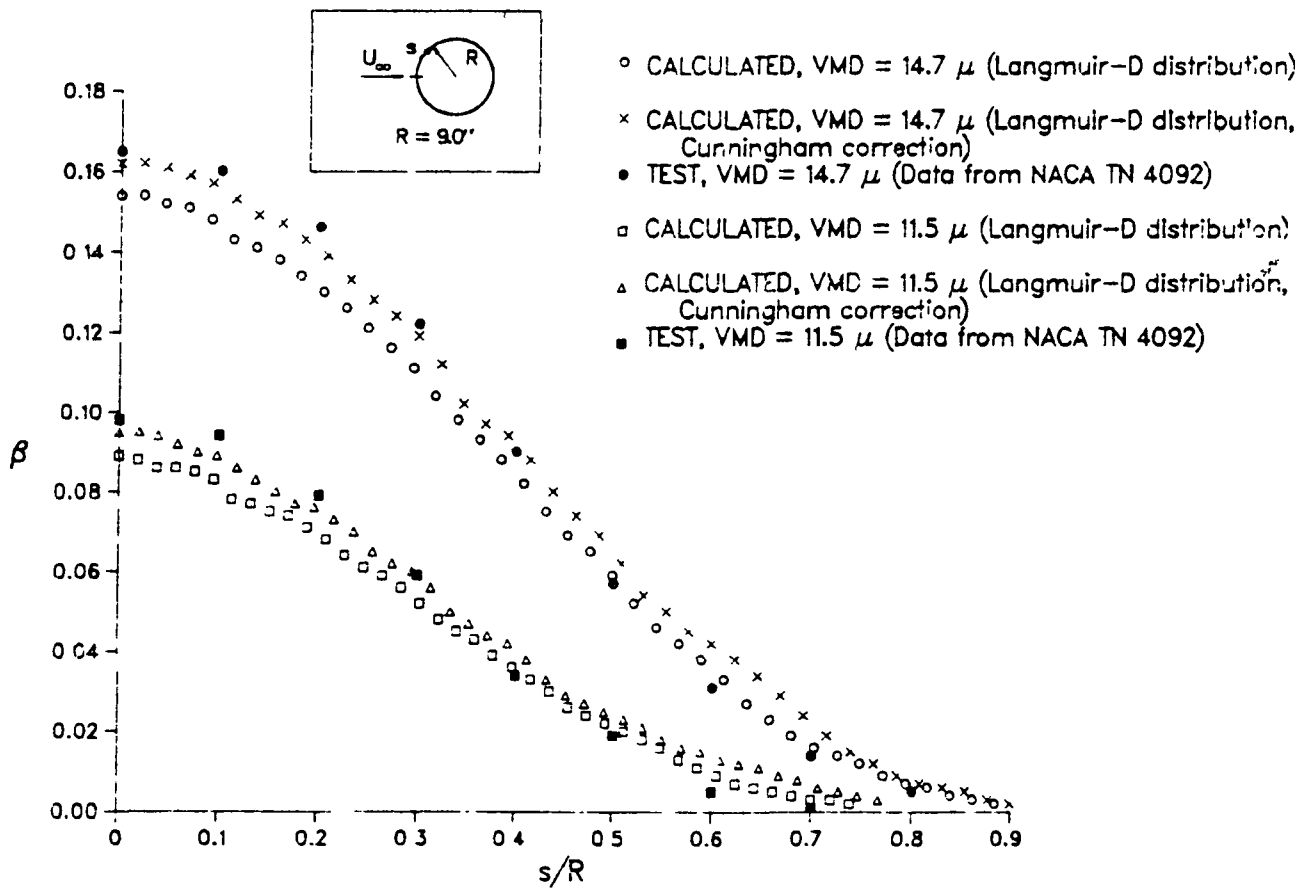


Figure 14 - Local Impingement Efficiency; Sphere

$$\alpha = 0^\circ \text{ and } 25^\circ$$

$$V_\infty = 175 \text{ kts}$$

$$T_{S_\infty} = 50^\circ\text{F}$$

$$P_{S_\infty} = 28.2 \text{ in. Hg}$$

$$M_{CF} = .625 \text{ (compressor face Mach no.)}$$

$$d = 30\mu\text{m}$$

The  $\alpha = 25^\circ$  condition, close to the inlet design separation envelope, was selected as the 'worst' test case to thoroughly check the trajectory analysis code. These conditions represent a realistic full-power-takeoff flight situation, but are not representative of a typical icing condition. However, as to be seen from the computed results, these represent a severe flowfield situation in terms of the droplet trajectory computation, because of the high engine suction flow as well as the extreme angle of attack involved.

The computational boundaries for the 3-D full potential as well as the 3-D trajectory code were

$$|X_\infty - X_{CF}| = 10r_{CF}$$

$$r_{\max} = 10r_{CF}$$

where  $X_\infty$  = freestream x-boundary of cylindrical computational domain

$X_{CF}$  = compressor face x-boundary

$r_{CF}$  = inlet fan radius

$r_{\max}$  = radial boundary for cylindrical computational domain.

The computing time for each angle of attack case impingement analysis was about 5 min. on the CRAY-1S.

### 5.2.1 Limiting Impingement Points

The tangent impact points (\*) are shown in Figures 15 and 16. The extent of droplet impingement is indicated by the portion of cowl surface bounded by these points. The 3-dimensional character of the flowfield and geometry causes the azimuthal variation of the tangent impact positions. It should be noted that no such variation in  $\theta$  is possible for an axisymmetric inlet at zero angle of attack, although  $\theta$ -variation of a different kind will result at non-zero angles of attack for axisymmetric inlets (non-axisymmetric flowfield).

The following features are noted from Figures 15 and 16.

- (1) Wider extent of droplet impingement near  $\theta = 135^\circ$  ('squashed' region) for both  $\alpha = 0^\circ$  and  $\alpha = 25^\circ$  cases.
- (2) For  $\alpha = 0^\circ$  case, all of the inner tangent impact points lie on the inner cowl surface; for  $\alpha = 25^\circ$ , a switch-over occurs at  $\theta \approx 110^\circ$  beyond which the inner tangent impact points lie completely on the outer cowl surface.

These observations can be understood in terms of (1) the increased exposure area to droplet impingement near the 'squashed' region due to the thickening of cowl cross-section near  $\theta = 135^\circ$  and (2) the effect of high angle of attack causing the droplet impingement to occur more on the outer cowl surface for  $\theta \geq 90^\circ$ .

### 5.2.2 Droplet Trajectories on the Inlet Symmetry Plane

The impinging droplet trajectories on the inlet symmetry plane are shown in Figures 17 thru 22.

The details of these near the upper ( $\theta = 0^\circ$ ) and lower ( $\theta = 180^\circ$ ) cowls are depicted in Figures 18 and 19 ( $\alpha = 0^\circ$ ) and in Figures 21 and 22 ( $\alpha = 25^\circ$ ).

The main feature noted in these figures is that the trajectories exhibit strong inward curvature as they approach the lip region. This is caused by the strong inlet suction flow typical of the full-power-takeoff setting. The combined effect of the high suction and high angle of attack is even more pronounced in Figures 20 and 22, where some extreme trajectory turn-arounds are seen near the lower cowl lip.

### 5.2.3 Computed Local Impingement Efficiency Distributions

Plots of computed  $\beta$  as a function of cowl contour arc length ( $s$ ) at  $\theta = 0^\circ, 45^\circ, 90^\circ, 135^\circ$  and  $180^\circ$  are shown in Figure 23 for both angles of attack. Arc length ( $s$ ) is the surface contour distance measured from the origin at the hi-lite, along a particular constant- $\theta$  cowl contour curve.

The following features are noted from the computed  $\beta$  curves;

- (1)  $\beta$  peaks broaden and decrease monotonically from  $\theta = 0^\circ$  to  $\theta = 135^\circ$  for both angles of attack.
- (2) Zero angle of attack cases exhibit more rapid rise to the peak  $\beta$  values compared to  $\alpha = 25^\circ$  cases, with the exception of curves for  $\theta = 180^\circ$ .
- (3) Double  $\beta$  peaks are observed for  $\theta = 180^\circ$  ( $\alpha = 25^\circ$ ), with a sharp maximum of  $\beta = .84$  and a weak secondary peak of  $\beta = .25$ .

Observation (1) can be explained in terms of the geometric character of the inlet; the progressive thickening of the cowl cross-sections from  $\theta = 0^\circ$  to  $\theta = 135^\circ$ , thus resulting in successively lower local droplet flux while increasing the extent of exposure to droplet impingement.

The second feature can be explained in that the distribution of impinging trajectories is more asymmetric about cowl hi-lites in  $\alpha = 0^\circ$  cases than  $\alpha = 25^\circ$ , as seen in Figures 18 and 21 for example. The strong inward curvature of trajectories adjacent to the inner tangent trajectory causes the location of the near normal impaction to be closer to the inner tangent impact point. For  $\alpha = 25^\circ$  cases the effect of high angle of attack partially offsets this trend, resulting in a more symmetric distribution.

The presence of strong turn-arounds in trajectories (Figure 22) is responsible for the sharp primary  $\beta$  peak in observation (3), causing a localized region of high droplet flux. The weak secondary peak in  $\beta$  occurs near the location of near normal impaction; local maxima in  $\beta$  is expected to occur whenever the impact velocity of droplet is nearly aligned with the surface normal vector, as shown in equation (1.0). Similar observations were also reported in 2-D cases, involving an airfoil with a leading edge ram air scoop [22] and ice-accreted airfoils [46], where the trajectories undergo strong turn-arounds due to the abrupt and strong flow gradients present near the leading edge.

The tails of the  $\beta$  curves are not plotted because these will require extrapolation of  $\beta$  in the present numerical scheme (see Figure 10); although the  $\beta$  values must go to zero at the tangent impact points (zero droplet flux since  $\bar{U} \cdot \bar{n} = 0$  there), the edge of the centroid grid  $\{\bar{x}_c(i,j)\}$  is reached before getting to the edge of the impingement point grid  $\{\bar{x}_m(I,J)\}$ .

Experimental impingement data for the 3-D inlet analyzed are not presently available for comparison with the computed results. However, there is an on-going research program (Joint BMAC-Wichita State University) to obtain impingement data for the inlet analyzed as well as for several other geometries during the time period 1985-1986. Project director for this research program is Dr. G.W. Zumwalt and the experimental  $\beta$  measurement involves a dye-water mixture spraying technique as well as laser reflectance spectroscopy. Tests will be conducted at the NASA-Lewis Icing Research Tunnel (IRT) under joint FAA and NASA sponsorship.



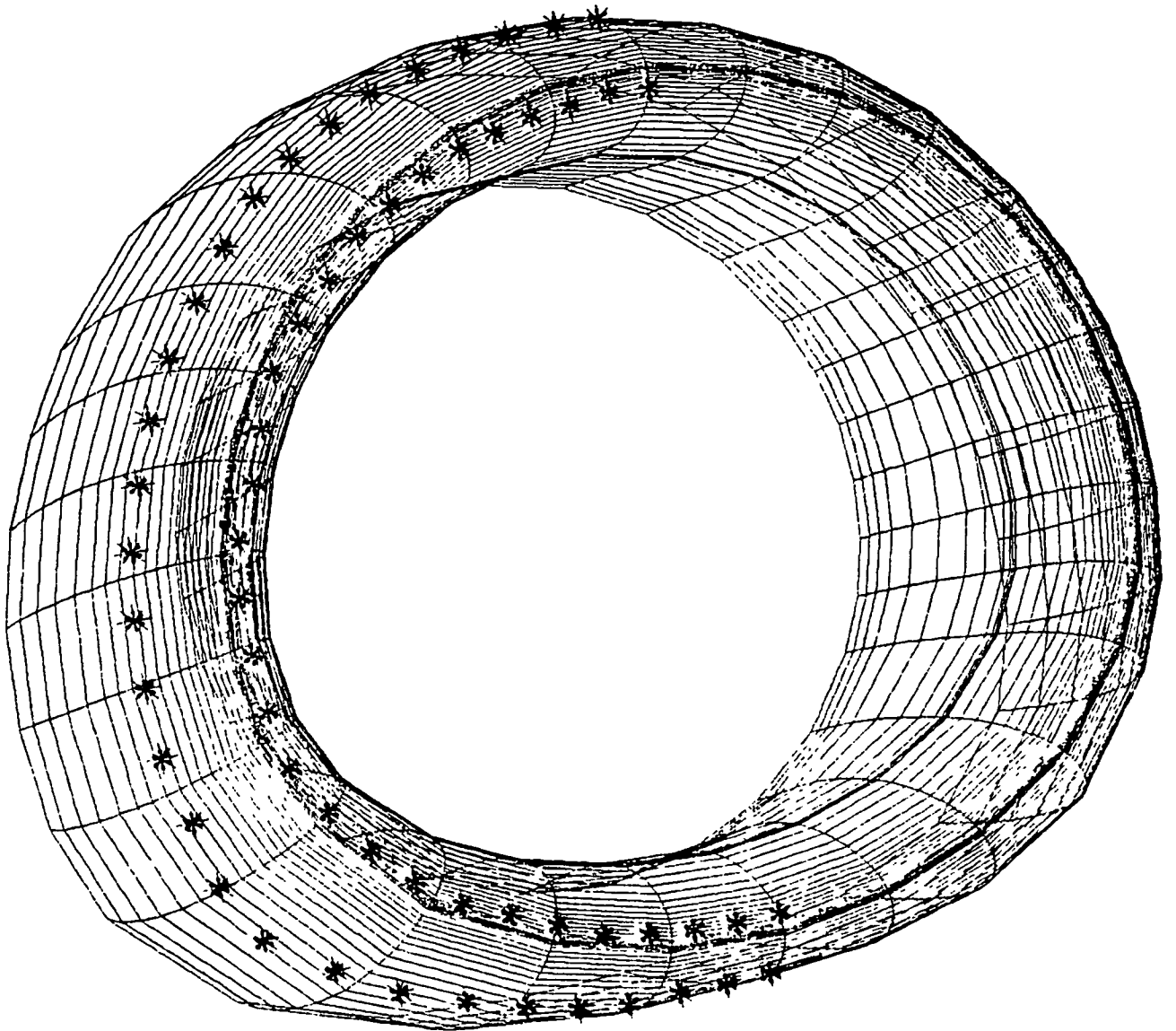


Figure 15 - Limiting Impingement Points;  $\alpha = 0^{\circ}$ , 737-300 Prototype Inlet

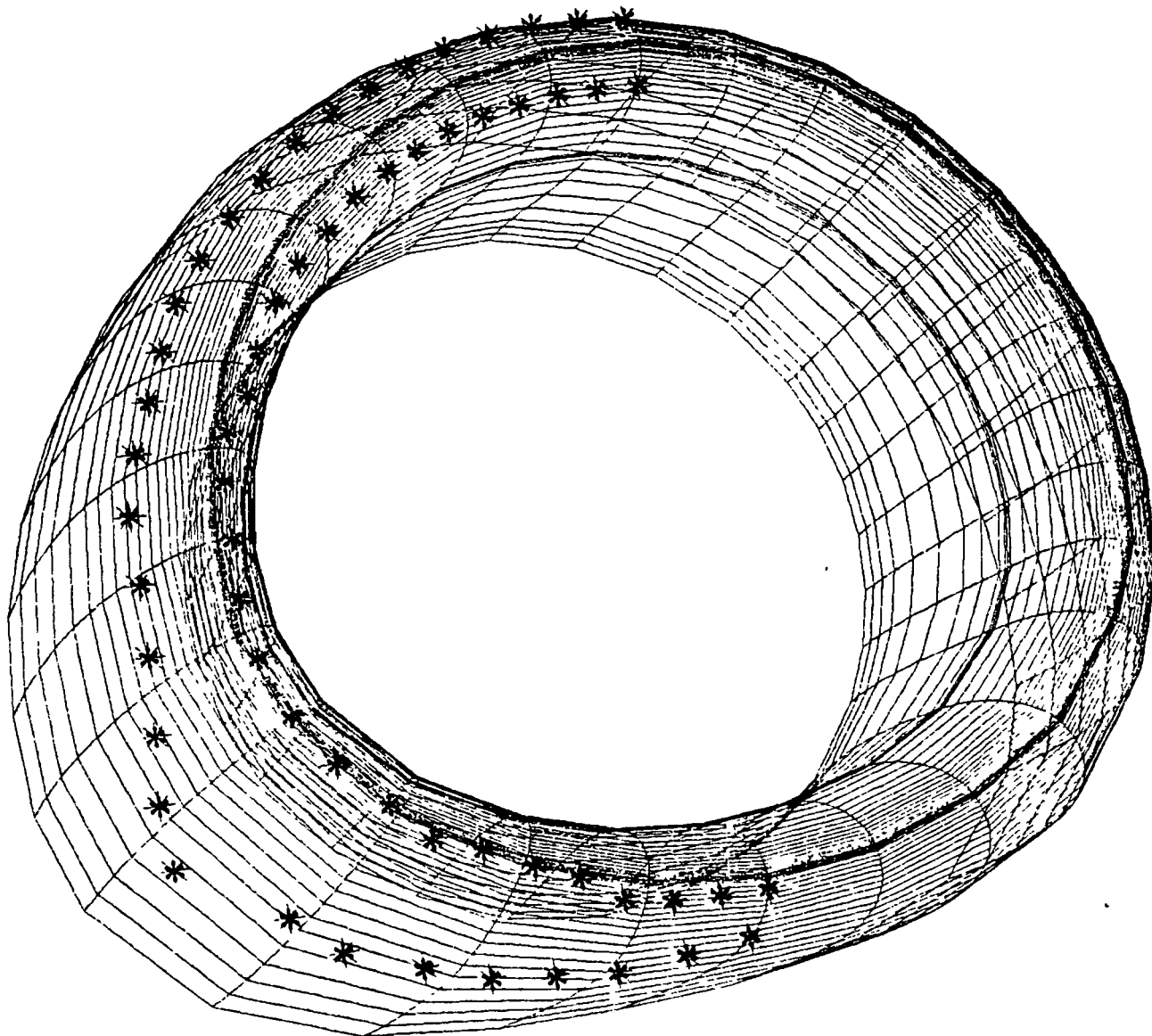


Figure 16 - Limiting Impingement Points;  $\alpha = 25^{\circ}$ , 737-300 Prototype Inlet

ORIGINAL PAGE IS  
OF POOR QUALITY

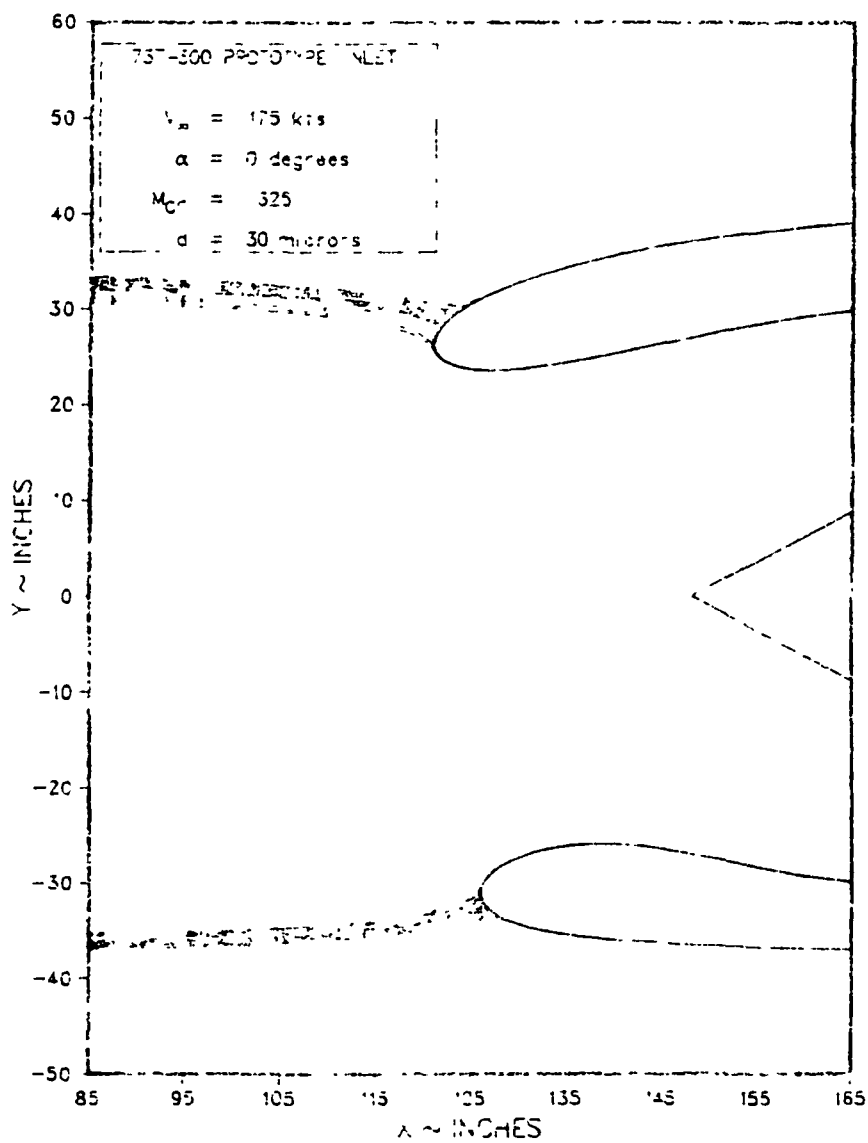


Figure 17 - Impinging Droplet Trajectories,  $\alpha = 0^{\circ}$

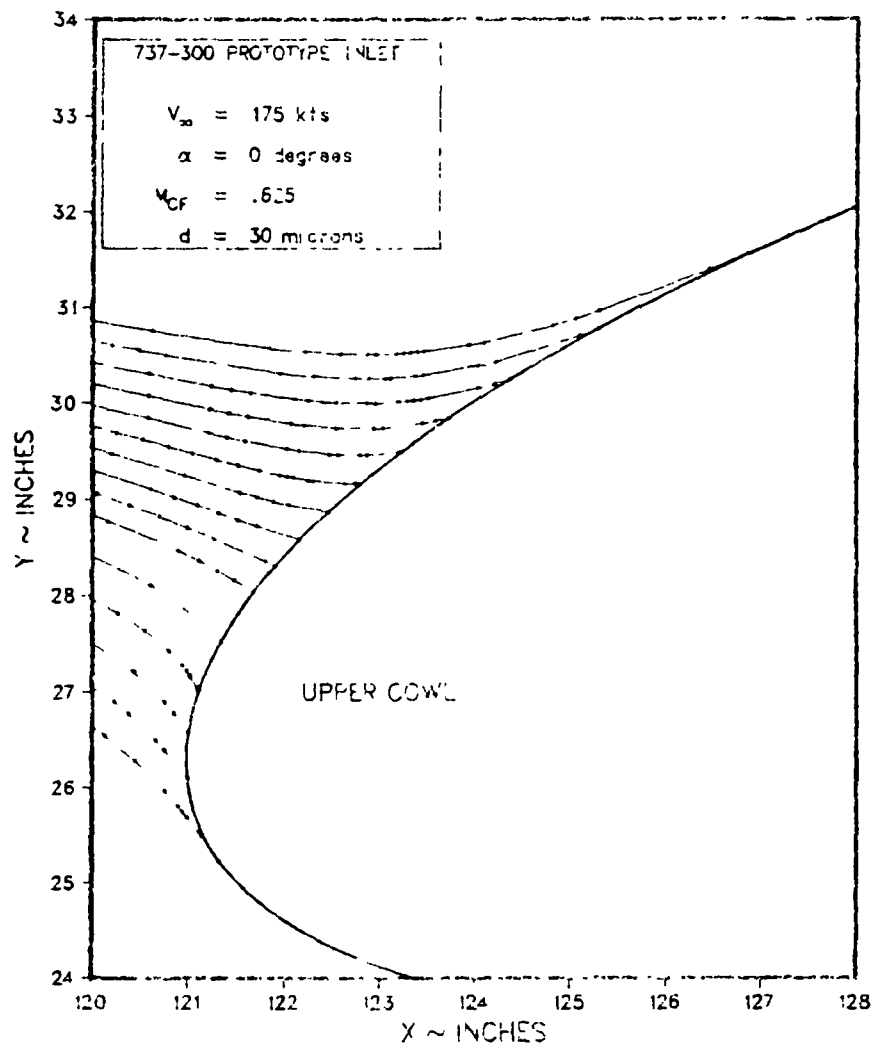


Figure 18 - Impinging Droplet Trajectories, Upper Cowl;  $\alpha = 0^{\circ}$

ORIGINAL PAGE IS  
OF POOR QUALITY

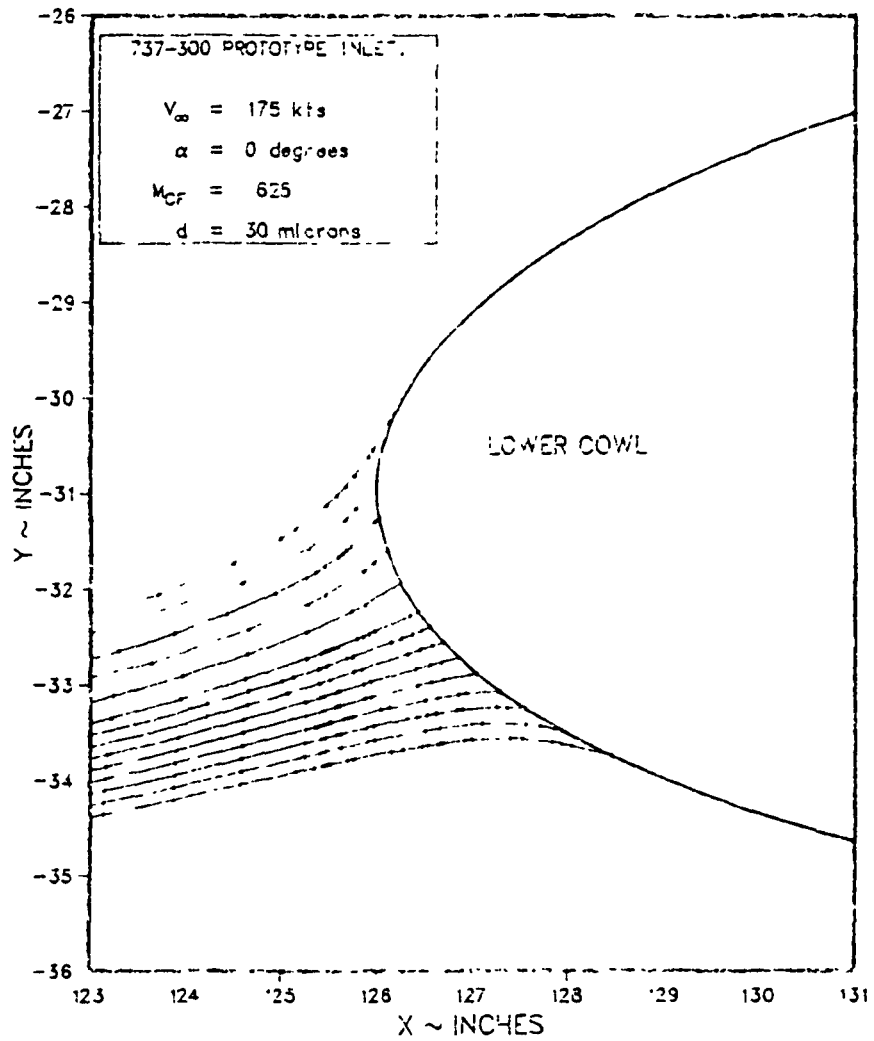


Figure 19 - Impinging Droplet Trajectories, Lower Cowl;  $\alpha = 0^{\circ}$

ORIGINAL PAGE IS  
OF POOR QUALITY

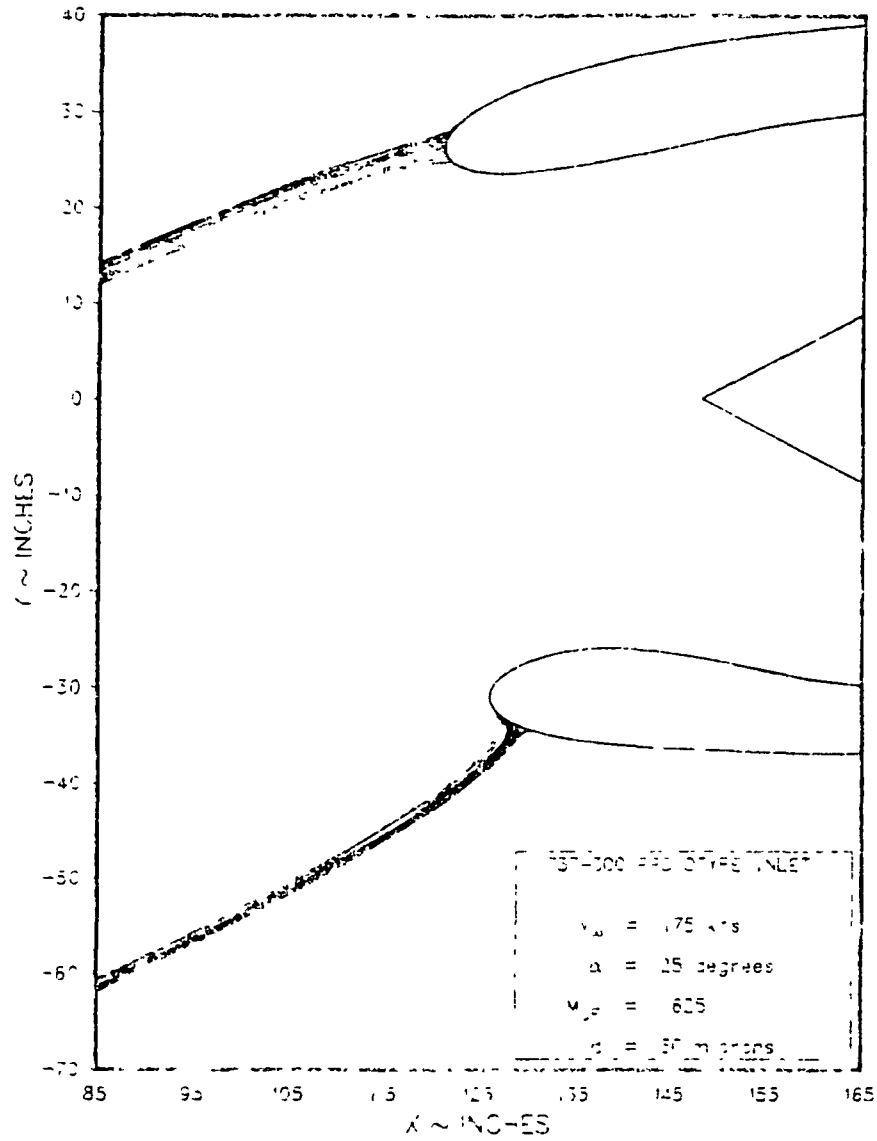


Figure 20 - Impinging Droplet Trajectories;  $\alpha = 25^\circ$

ORIGINAL PAGE 13  
OF FOUR QUALITY

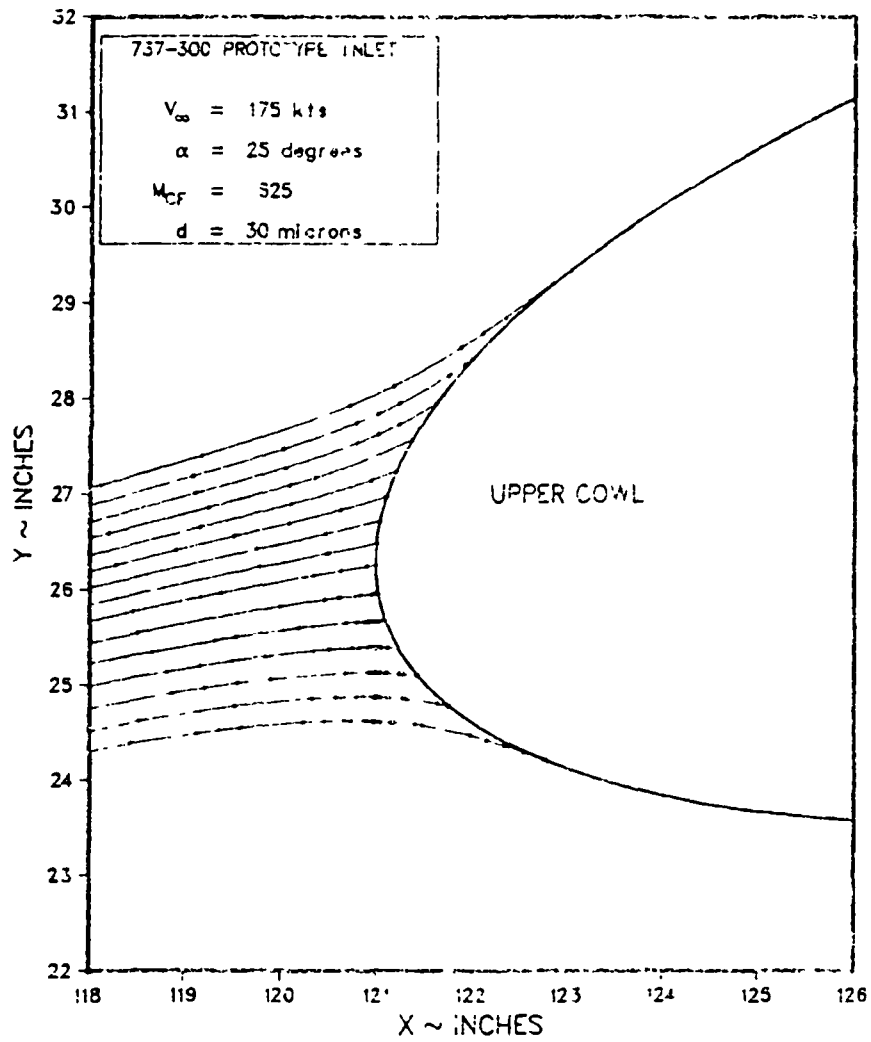


Figure 21 - Impinging Droplet Trajectories, Upper Cowl;  $\alpha = 25^{\circ}$

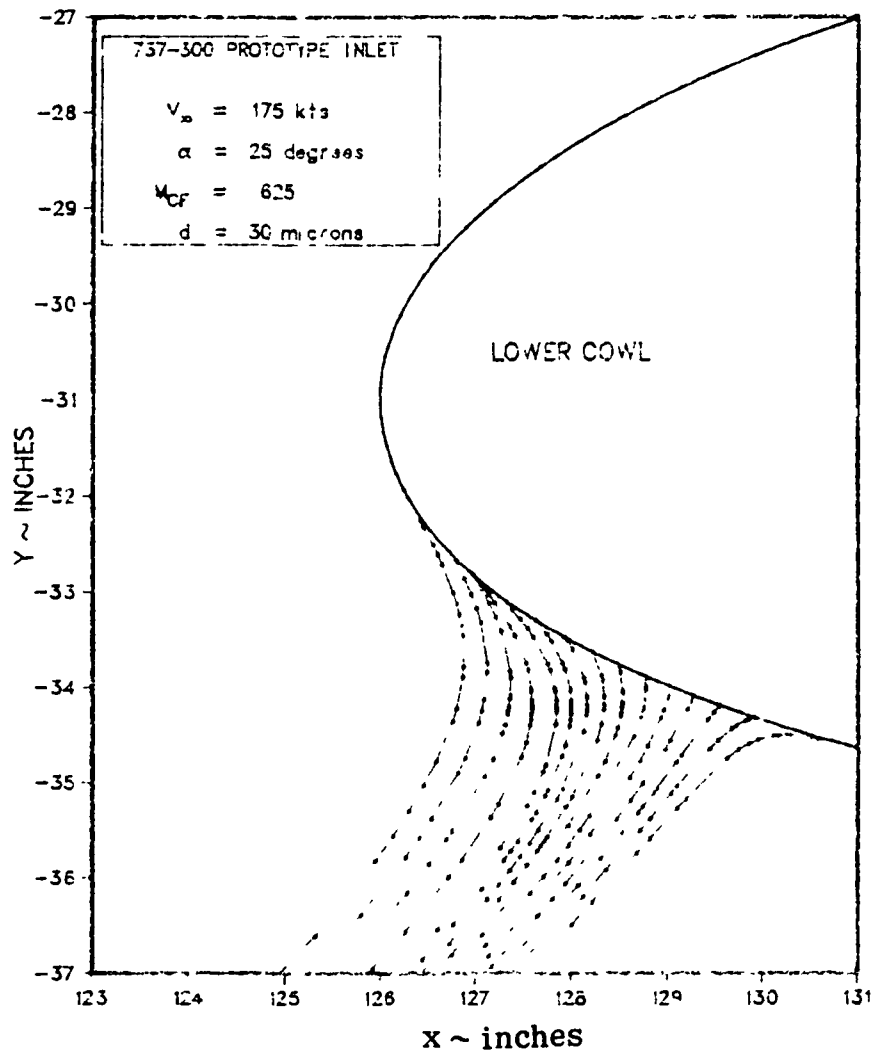


Figure 22 - Impinging Droplet Trajectories, Lower Cowl;  $\alpha = 25^{\circ}$



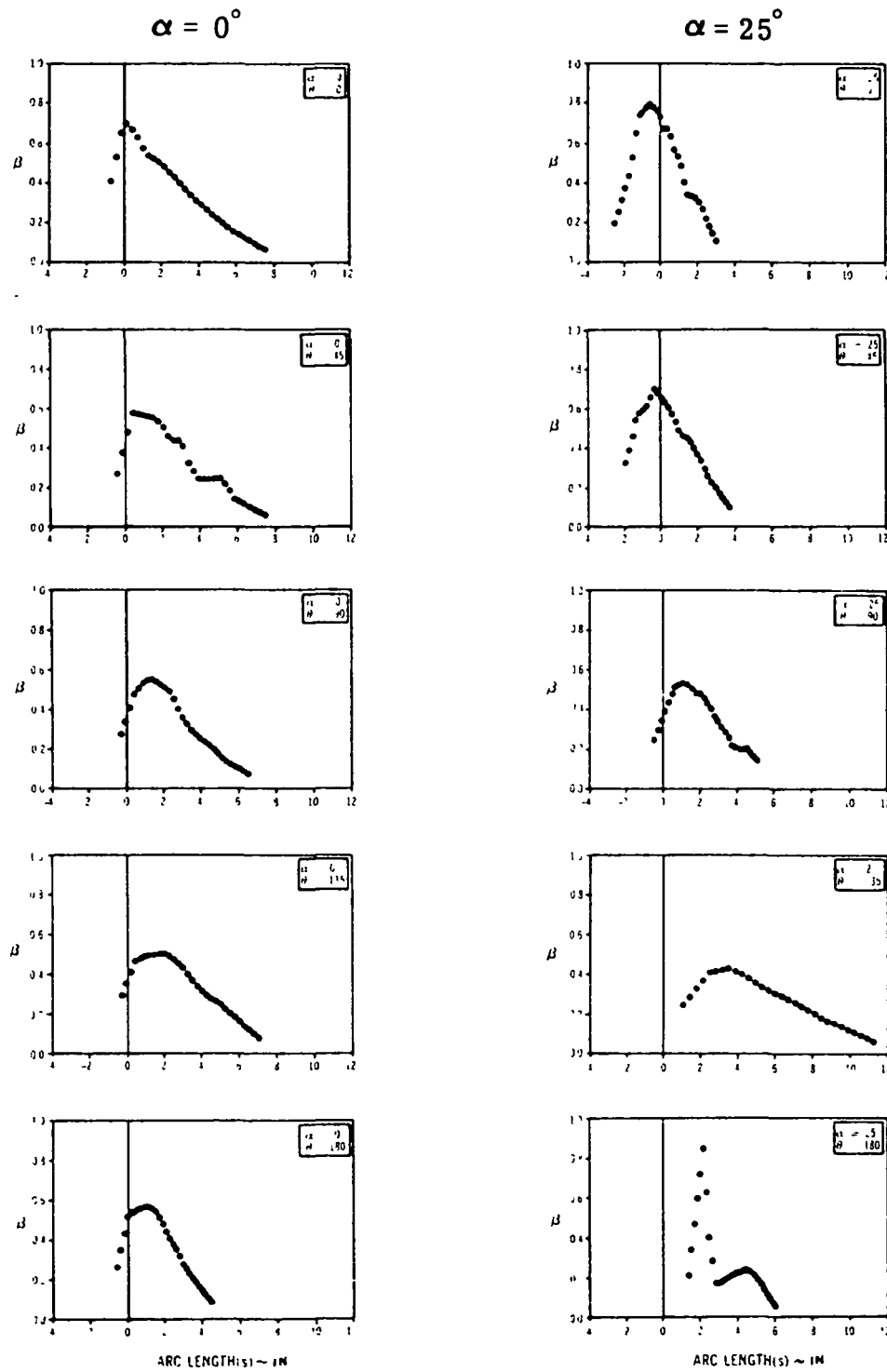


Figure 23 - Computed Local Impingement Efficiency Distribution;  
737-300 Prototype Inlet,  $\alpha = 0^\circ$  and  $25^\circ$

### 5.3 TRAJECTORY SIMULATION FOR A SOLID PARTICLE

A sample trajectory simulation of a solid particle was performed using the flowfield about the 737-300 prototype inlet at  $25^\circ$  angle of attack. A simplistic bounce kinematic model assuming 50% momentum loss along the normal and no loss along the tangential direction ( $r_n = 0.5$ ,  $r_t = 1.0$  in equation (4-18)) was used to compute the particle velocity immediately after the impact.

The particle was injected into the flowfield at about two fan radii ahead of the inlet with the initial velocity (cylindrical) of  $[U_x, U_r, U_\theta] = [0, -2V_\omega, V_\omega]$ . The ricochet trajectory of the particle is depicted in Figure 24.

The sand separator efficiency of an engine inlet can be determined by tracing many such trajectories to compute the normalized freestream flux (or the flux through the surface of initial trajectory positions) of particles that correspond to the particle flux at the sand separator (scavenge) channel of the engine inlet.

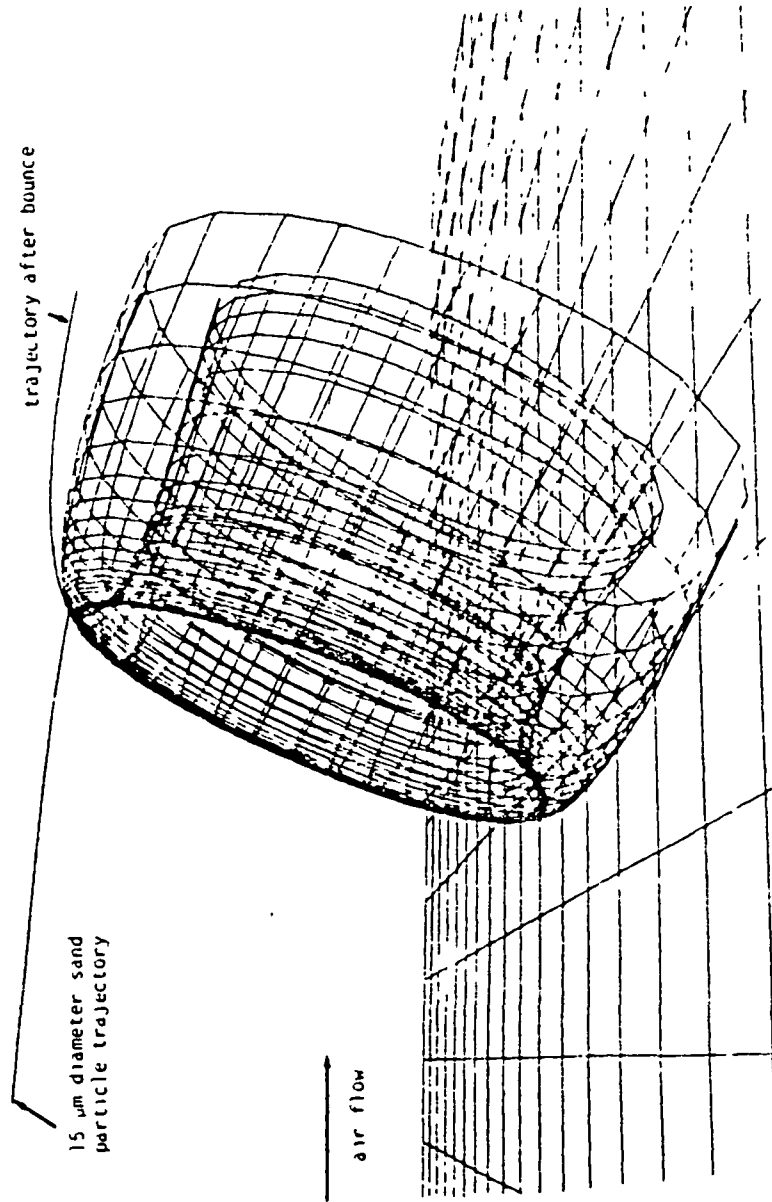


FIGURE 24 - SAND PARTICLE TRAJECTORY TRACE;  
737-300 PROTOTYPE INLET,  $\alpha = 25^\circ$

## 6.0 CONCLUSIONS AND RECOMMENDATIONS FOR FURTHER WORK

Based on the results, findings and the physical assumptions of the present analysis method, the following conclusions can be made:

- (1) This investigation represents the first attempt in the analytical determination of the detailed water droplet impingement efficiency distribution on a 3-D engine inlet surface.
- (2) Accurate surface definition of the 3-D surface is essential in the 3-D droplet trajectory/impingement analyses.
- (3) For the grid (mesh) definition of the flowfield, the flowfield accuracy as well as an accurate means of flow velocity interpolation are essential in computing accurate droplet trajectories.
- (4) Integration error control in the numerical integration of the trajectory equation is an important consideration in that it governs the computational efficiency as well as the accuracy of the computed trajectories with respect to the flowfield accuracy.
- (5) This analysis tool can easily be extended for problems involving solid particles, such as sand ingestion analyses.
- (6) Although experimental data is not yet available to directly verify the analysis results for the engine inlet analyzed, good agreement is obtained between the published test and computed results for an axisymmetric problem investigated.
- (7) Present analysis tool will not be appropriate for problems involving large concentration of water droplets ( $LWC \geq 10 \text{ gm/m}^3$ ) or large droplets ( $d \geq 1000 \text{ }\mu\text{m}$ ).

Some recommendations for further work are:

- (1) Particle heat transfer equations should be incorporated in order to extend the present method to transonic/supersonic flows or flows in the engine compressor and turbine stages.
- (2) Reliable experimental drag data for large, non-spherical droplets is needed to extend the droplet size range of the method.
- (3) Effect of thick boundary layers on droplet trajectory should be studied for internal flow applications.
- (4) Improved trajectory computation can be achieved by using a body-fitted mesh definition of the flowfield and solving the trajectory equation in the transformed Cartesian mesh obtained through the metric of transformation for the particular body-fitted mesh chosen.

## APPENDIX A

### Parametric Description of Curves and Surfaces

#### A.1.0 Parametric Curve Description

A 3-dimensional curve segment can be represented parametrically by a polynomial expansion of the parameter variable  $u$

$$\bar{r}(u) = \sum_{n=0}^{n_{\max}} \bar{a}_n u^n, \quad u \in [0,1] \quad (\text{A-1})$$
$$n = 0,1,2,\dots, n_{\max}$$

where  $\bar{r}$   $\equiv$  position vector along the curve,

$\bar{a}_n$   $\equiv$   $n^{\text{th}}$  order vector coefficient.

The vectors corresponding to the parameter values of  $u=0$  and  $u=1$ , i.e.,  $\bar{r}(0)$  and  $\bar{r}(1)$ , are the end point positions of the curve segment.

The maximum power ( $n_{\max}$ ) of the parametric variable retained in the expansion determines the order of parametrization. Thus  $n_{\max}=3$  (or  $n_{\max}=5$ ) represents a cubic (or quintic) parametrization. The cubic and quintic representations are currently two of the most commonly used forms of analytic curve/surface construction techniques [39].

It will be shown later that these curve parametrization equations lead to surface parametric equations.

### A.1.1 Parametric Cubic Curve Representation

From equation (A-1), the parametric cubic curve is

$$\bar{r}(u) = \bar{a}_0 + \bar{a}_1 u + \bar{a}_2 u^2 + \bar{a}_3 u^3 \quad (A-2)$$

Equation (A-2) can be written in matrix form,

$$\bar{r}(u) = [U] [\bar{A}]^T$$

$$\text{where } [U] \equiv [1 \ u \ u^2 \ u^3]$$

$$[\bar{A}] \equiv [\bar{a}_0 \ \bar{a}_1 \ \bar{a}_2 \ \bar{a}_3]$$

(A-3)

Differentiating equation (A-3) with respect to  $u$ ,

$$\bar{r}_u(u) = [0 \ 1 \ 2u \ 3u^2] [\bar{A}]^T \quad (A-4)$$

The end point ( $u = 0, u = 1$ ) quantities of equations (A-2) and (A-3) are

$$\bar{r}(0) = [1 \ 0 \ 0 \ 0] [\bar{A}]^T$$

$$\bar{r}(1) = [1 \ 1 \ 1 \ 1] [\bar{A}]^T$$

$$\bar{r}_u(0) = [0 \ 1 \ 0 \ 0] [\bar{A}]^T$$

$$\bar{r}_u(1) = [0 \ 1 \ 2 \ 3] [\bar{A}]^T$$

These can be expressed in matrix form,

$$[\bar{r}(0) \ \bar{r}(1) \ \bar{r}_u(0) \ \bar{r}_u(1)]^T = [N] [\bar{A}]^T \quad (A-5)$$

where

$$[N] \equiv \begin{bmatrix} 1 & 0 & 0 & 0 \\ 1 & 1 & 1 & 1 \\ 0 & 1 & 0 & 0 \\ 0 & 1 & 2 & 3 \end{bmatrix}$$

The L.H.S. of equation (A-5) is just the vector array of the four curve end point conditions (positions and tangents) required to determine the four vector coefficients of the cubic parametrization. To solve for  $[\bar{A}]$ , equation (A-5) is to be inverted:

$$[\bar{A}]^T = [C \mid \bar{r}(0) \quad \bar{r}(1) \quad \bar{r}_u(0) \quad \bar{r}_u(1)]^T \quad (A-6)$$

where

$$[C] \equiv [N]^{-1} = \begin{bmatrix} 1 & 0 & 0 & 0 \\ 0 & 0 & 1 & 0 \\ -3 & 3 & -2 & -1 \\ 2 & -2 & 1 & 1 \end{bmatrix}$$

Substitution of (A-6) into (A-3) completes the cubic curve parametrization,

$$\bar{r}(u) = [U] [C] [\bar{r}(0) \quad \bar{r}(1) \quad \bar{r}_u(0) \quad \bar{r}_u(1)]^T \quad (A-7)$$

Equation (A-7) implies that the cubic parametrization requires only the end point positions and slopes as inputs.

Another approach of arriving at the same result is to express  $\bar{r}(u)$  in terms of a set of four cubic polynomial blending functions,  $\{f_i\}$ ;

$$\begin{aligned} \bar{r}(u) &= \bar{r}(0) f_1(u) + \bar{r}_u(0) f_2(u) + \bar{r}(1) f_3(u) + \bar{r}_u(1) f_4(u) \quad (A-8) \\ &= [f_1(u) \quad f_2(u) \quad f_3(u) \quad f_4(u)] [\bar{r}(0) \quad \bar{r}_u(0) \quad \bar{r}(1) \quad \bar{r}_u(1)]^T \end{aligned}$$

Equation (A-8) imposes the following constraints on the blending functions:

	$f_1$	$f_1'$	$f_2$	$f_2'$	$f_3$	$f_3'$	$f_4$	$f_4'$	
$u = 0$	1	0	0	0	0	1	0	0	(A-9)
$u = 1$	0	0	1	0	0	0	0	1	



The cubic blending functions are

$$f_m(u) = \sum_{n=1}^4 b_{mn} u^{n-1} \quad ; \quad m = 1, 2, 3, 4 \quad (\text{A-10})$$

Coefficients  $b_{mn}$  are determined easily from (A-9) and (A-10):

$$\begin{array}{lll} m = 1; & 1 = b_{11} & b_{11} = 1 \\ & 0 = b_{11} + b_{12} + b_{13} + b_{14} & b_{12} = 0 \\ & 0 = b_{12} & b_{13} = -3 \\ & 0 = b_{12} + 2b_{13} + 3b_{14} & b_{14} = 2 \end{array}$$

Repeating the process for the remaining three, we have

$$\begin{array}{ll} f_1(u) = & -3u^2 + 2u^3 \\ f_2(u) = & 3u^2 - 2u^3 \\ f_3(u) = & u \quad -2u^2 + 3u^3 \\ f_4(u) = & -u^2 + u^3 \end{array} \quad (\text{A-11})$$

In matrix form, (A-11) becomes

$$\begin{aligned} [ f_1(u) \quad f_2(u) \quad f_3(u) \quad f_4(u) ] &= [ 1 \quad u \quad u^2 \quad u^3 ] \begin{bmatrix} 1 & 0 & 0 & 0 \\ 0 & 0 & 1 & 0 \\ -3 & 3 & -2 & 1 \\ 2 & -2 & 1 & 1 \end{bmatrix} \\ &= [ U ] [ C ] \end{aligned} \quad (\text{A-12})$$

Substituting (A-12) into (A-8), we see that the same parametric equation (A-7) results.

## A.2.0 Parametric Surface Description

The parametric curve formulation can be extended to describe a surface element (patch) by allowing the vector coefficients in equation (A-1) to be functions of a second parameter.

### A.2.1 Parametric Bi-cubic Surface Representation

Expressing the vector coefficients  $[\bar{a}_i]$  of equation (A-2) as functions of a second parameter  $v$ , we have

$$\bar{r}(u,v) = \bar{a}_0(v) + \bar{a}_1(v)u + \bar{a}_2(v)u^2 + \bar{a}_3(v)u^3 \quad (A-13)$$

Since equations (A-2) and (A-8) are equivalent, i.e.,  $\bar{a}_i$ 's are simply the linear combinations of the curve end point position and tangent vectors, one can also introduce the parameter  $v$  into the equation (A-8) to describe a patch;

$$\bar{r}(u,v) = \bar{r}(0,v)f_1(u) + \bar{r}_u(0,v)f_2(u) + \bar{r}(1,v)f_3(u) + \bar{r}_u(1,v)f_4(u) \quad (A-14)$$

If we had arrived at the curve parametric equation using the parameter variable name  $v$  instead of  $u$  and then introduced the second parameter  $u$ , we would have obtained

$$\bar{r}(u,v) = \bar{r}(u,0)f_1(v) + \bar{r}_v(u,0)f_2(v) + \bar{r}(u,1)f_3(v) + \bar{r}_v(u,1)f_4(v). \quad (A-15)$$

Inspection of equations (A-14) and (A-15) shows that each form uses a set of single parameter blending functions and hence is not symmetric in  $u$  and  $v$ . Physical meaning of these equations can be shown from Figure A1.

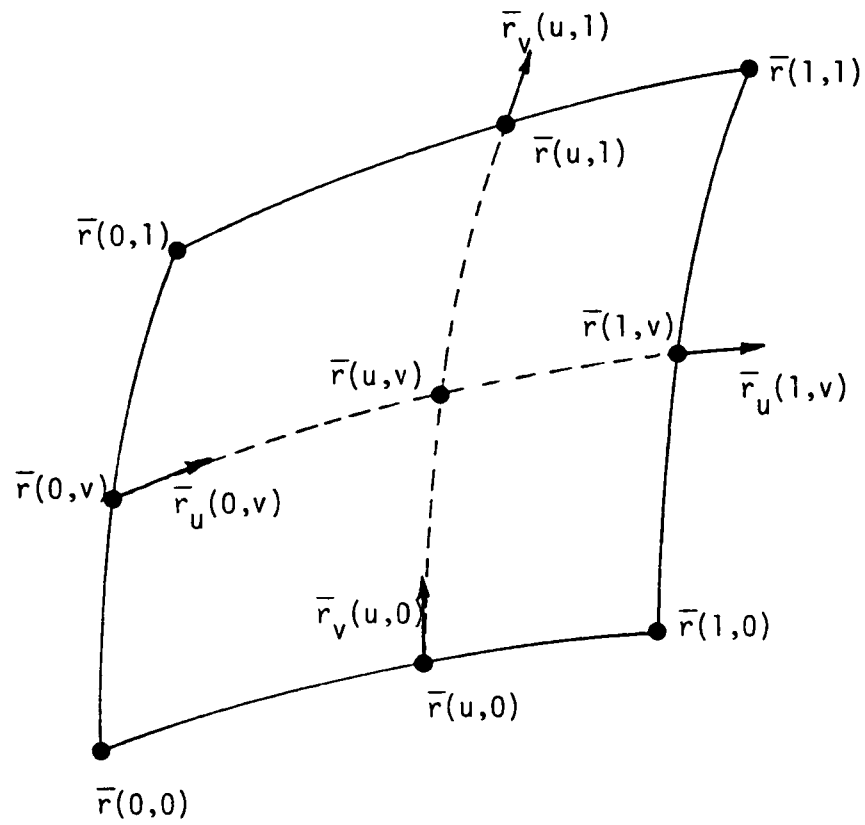


Figure A1 - Parametric Surface Patch

The parametric form of (A-14) is expressed in terms of the variable end points ( $\bar{r}(0,v)$  and  $\bar{r}(1,v)$ ) and end point tangents ( $\bar{r}_u(0,v)$  and  $\bar{r}_u(1,v)$ ). Therefore it represents a u-parameter family of curves spanning the patch as the curve end conditions are continuously changed by sweeping v in the interval, [0,1]. Likewise, equation (A-15) represents a v-parameter family of curves spanning the patch. In order to obtain a bi-cubic surface parametrization symmetric in u and v, the two equations, (A-14) and (A-15), must be combined.

From equation (A-14)

$$\bar{r}(u,0) = \bar{r}(0,0)f_1(u) + \bar{r}(1,0)f_2(u) + \bar{r}_u(0,0)f_3(u) + \bar{r}_u(1,0)f_4(u) \quad (A-16)$$

$$\bar{r}(u,1) = \bar{r}(0,1)f_1(u) + \bar{r}(1,1)f_2(u) + \bar{r}_u(0,1)f_3(u) + \bar{r}_u(1,1)f_4(u) \quad (A-17)$$

Taking partials of (A-14) with respect to v

$$\bar{r}_v(u,v) = \bar{r}_v(0,v)f_1(u) + \bar{r}_v(1,v)f_2(u) + \bar{r}_{uv}(0,v)f_3(u) + \bar{r}_{uv}(1,v)f_4(u)$$

from which

$$\bar{r}_v(u,0) = \bar{r}_v(0,0)f_1(u) + \bar{r}_v(1,0)f_2(u) + \bar{r}_{uv}(0,0)f_3(u) + \bar{r}_{uv}(1,0)f_4(u) \quad (A-18)$$

$$\bar{r}_v(u,1) = \bar{r}_v(0,1)f_1(u) + \bar{r}_v(1,1)f_2(u) + \bar{r}_{uv}(0,1)f_3(u) + \bar{r}_{uv}(1,1)f_4(u) \quad (A-19)$$

Substituting equations (A-16) thru (A-19) into (A-15) and re-expressing each term on the R.H.S. of (A-15) in matrix form,

$$\begin{aligned} \bar{r}(u,0)f_1(v) &= [ \bar{r}(0,0)f_1(u) + \bar{r}(1,0)f_2(u) + \bar{r}_u(0,0)f_3(u) + \bar{r}_u(1,0)f_4(u) ] f_1(v) \\ &= [ f_1(u) \ f_2(u) \ f_3(u) \ f_4(u) ] \begin{bmatrix} \bar{r}(0,0) & 0 & 0 & 0 \\ \bar{r}(1,0) & 0 & 0 & 0 \\ \bar{r}_u(0,0) & 0 & 0 & 0 \\ \bar{r}_u(1,0) & 0 & 0 & 0 \end{bmatrix} \begin{bmatrix} f_1(v) \\ f_2(v) \\ f_3(v) \\ f_4(v) \end{bmatrix} \quad (A-20) \end{aligned}$$

$$\begin{aligned}
\bar{r}(u,1)f_2(v) &= [\bar{r}(0,1)f_1(u)+\bar{r}(1,1)f_2(u)+\bar{r}_u(0,1)f_3(u)+\bar{r}_u(1,1)f_4(u)]f_2(v) \\
&= [f_1(u) \ f_2(u) \ f_3(u) \ f_4(u)] \begin{bmatrix} 0 & \bar{r}(0,1) & 0 & 0 \\ 0 & \bar{r}(1,1) & 0 & 0 \\ 0 & \bar{r}_u(0,1) & 0 & 0 \\ 0 & \bar{r}_u(1,1) & 0 & 0 \end{bmatrix} \begin{bmatrix} f_1(v) \\ f_2(v) \\ f_3(v) \\ f_4(v) \end{bmatrix} \quad (A-21)
\end{aligned}$$

$$\begin{aligned}
\bar{r}_v(u,0)f_3(v) &= [\bar{r}_v(0,0)f_1(u)+\bar{r}_v(1,0)f_2(u)+\bar{r}_{uv}(0,0)f_3(u)+\bar{r}_{uv}(1,0)f_4(u)]f_3(v) \\
&= [f_1(u) \ f_2(u) \ f_3(u) \ f_4(u)] \begin{bmatrix} 0 & 0 & \bar{r}_v(0,0) & 0 \\ 0 & 0 & \bar{r}_v(1,0) & 0 \\ 0 & 0 & \bar{r}_{uv}(0,0) & 0 \\ 0 & 0 & \bar{r}_{uv}(1,0) & 0 \end{bmatrix} \begin{bmatrix} f_1(v) \\ f_2(v) \\ f_3(v) \\ f_4(v) \end{bmatrix} \quad (A-22)
\end{aligned}$$

$$\begin{aligned}
\bar{r}_v(u,1)f_4(v) &= [\bar{r}_v(0,1)f_1(u)+\bar{r}_v(1,1)f_2(u)+\bar{r}_{uv}(0,1)f_3(u)+\bar{r}_{uv}(1,1)f_4(u)]f_4(v) \\
&= [f_1(u) \ f_2(u) \ f_3(u) \ f_4(u)] \begin{bmatrix} 0 & 0 & 0 & \bar{r}_v(0,1) \\ 0 & 0 & 0 & \bar{r}_v(1,1) \\ 0 & 0 & 0 & \bar{r}_{uv}(0,1) \\ 0 & 0 & 0 & \bar{r}_{uv}(1,1) \end{bmatrix} \begin{bmatrix} f_1(v) \\ f_2(v) \\ f_3(v) \\ f_4(v) \end{bmatrix} \quad (A-23)
\end{aligned}$$

Adding equations (A-20) thru (A-23), equation (A-15) becomes

$$\bar{r}(u,v) = [f_1(u) \ f_2(u) \ f_3(u) \ f_4(u)] [\bar{Q}] [f_1(v) \ f_2(v) \ f_3(v) \ f_4(v)]^T \quad (A-24)$$

where the patch boundary matrix  $[\bar{Q}]$  is given by

$$[\bar{Q}] \equiv \begin{bmatrix} \bar{r}(0,0) & \bar{r}(0,1) & \bar{r}_v(0,0) & \bar{r}_v(0,1) \\ \bar{r}(1,0) & \bar{r}(1,1) & \bar{r}_v(1,0) & \bar{r}_v(1,1) \\ \bar{r}_u(0,0) & \bar{r}_u(0,1) & \bar{r}_{uv}(0,0) & \bar{r}_{uv}(0,1) \\ \bar{r}_u(1,0) & \bar{r}_u(1,1) & \bar{r}_{uv}(1,0) & \bar{r}_{uv}(1,1) \end{bmatrix} \quad (A-25)$$

Using the relationship (A-12) the blending function arrays can be expressed as

$$[f_1(u)f_2(u)f_3(u)f_4(u)] = [U] [C]$$

$$[f_1(v)f_2(v)f_3(v)f_4(v)]^T = [C]^T [V]^T$$

where  $[U]$ ,  $[V]$ , and  $[C]$  are defined as before.

Thus, the bi-cubic surface parametric equation is

$$\bar{r}(u,v) = [U] [C] [\bar{Q}] [C]^T [V]^T \quad (A-26)$$

Looking at the array elements of  $[\bar{Q}]$  the bi-cubic surface parametrization requires the four vector quantities at each of the four corners of the patch element;

$\bar{r} \equiv$  (position vector)

$\bar{r}_u \equiv$  (tangent vector along constant- $v$  curve)

$\bar{r}_v \equiv$  (tangent vector along constant- $u$  curve)

$\bar{r}_{uv} \equiv$  (twist vector)

Equation (A-26) is in a compact matrix form, well suited for numerical programming purposes.

### A.2.2 Geometrical Properties of Bi-cubic Surface Parametrization

From the bi-cubic parametric patch equation (A-26) many geometrical quantities can be obtained in analytic forms.

The unit normal vector ( $\bar{n}$ ) at a point  $\bar{r}(u_0, v_0)$  on the surface:

$$\bar{n} = \pm \frac{\bar{r}_u(u_0, v_0) \times \bar{r}_v(u_0, v_0)}{|\bar{r}_u(u_0, v_0) \times \bar{r}_v(u_0, v_0)|} \quad (\text{A-27})$$

(proper sign is to be chosen for particular application)

Here, 
$$\bar{r}_u(u_0, v_0) = [U'(u_0)][C][\bar{Q}][C]^T[V(v_0)]^T$$

$$\bar{r}_v(u_0, v_0) = [U(u_0)][C][\bar{Q}][C]^T[V'(v_0)]^T$$

$$[U'] \equiv \frac{\partial}{\partial u}[U] = [0 \ 1 \ 2u \ 3u^2]$$

$$[V'] \equiv \frac{\partial}{\partial v}[V] = [0 \ 1 \ 2v \ 3v^2].$$

The surface area (S) of a patch surface:

$$S = \int_0^1 \int_0^1 |\bar{r}_u \times \bar{r}_v| dudv \quad (\text{A-28})$$

where  $(\bar{r}_u \times \bar{r}_v)_i = \sum_{j=1}^3 \sum_{k=1}^3 \epsilon_{ijk} \left(\frac{\partial \bar{r}}{\partial u}\right)_j \left(\frac{\partial \bar{r}}{\partial v}\right)_k$

$$\left(\frac{\partial \bar{r}}{\partial u}\right)_j \equiv [U'] [C] [Q_j] [C]^T [V]^T$$

$$\left(\frac{\partial \bar{r}}{\partial v}\right)_k \equiv [U] [C] [Q_k] [C]^T [V']^T$$

The volume (Vol) subtended by a patch surface at the origin:

$$\text{Vol} = \frac{1}{3} \int_0^1 \int_0^1 \bar{r} \cdot (\bar{r}_u \times \bar{r}_v) dudv \quad (\text{A-29})$$

where  $\bar{r} \cdot (\bar{r}_u \times \bar{r}_v) = \sum_{i=1}^3 \sum_{j=1}^3 \sum_{k=1}^3 \epsilon_{ijk} r_i \left(\frac{\partial r}{\partial u}\right)_j \left(\frac{\partial r}{\partial v}\right)_k$



### A.2.3 Coordinate Transformations on Patch Surface

Once a surface is parametrized, transformations, such as translation and rotation, are easily implemented without having to modify the parameter functions - only the vector quantities at the boundary corners of the patch need be transformed. If  $[R]$  denotes the particular transformation matrix and  $\bar{r}^*$  the position vector in the transformed system

$$\bar{r}^*(u,v) = [U][C][\bar{Q}^*][C]^T[V]^T \quad (A-30)$$

where components of the new patch boundary matrix  $[\bar{Q}^*]$  are

$$Q^*_i = \sum_{j=1}^3 R_{ij} Q_j \quad ; \quad i = 1,2,3 \quad (A-31)$$

Similarly derivative quantities are obtained using the same  $[\bar{Q}^*]$ ;

$$\bar{r}'_u(u,v) = [U'] [C] [\bar{Q}^*] [C]^T [V]^T \quad (A-32)$$

### A.3.0 Trajectory-Bicubic Patch Intersection

To compute the impingement point on the surface defined in terms of the bicubic parametric patch notation, equations (A-25) and (A-26), the geometric intersection between the trajectory line segment and the patch must be determined.

### A.3.1 Problem Definition

At the required intersection point, the following must be satisfied:

$$F_i(u,v,w) \equiv l_i(w) - r_i(u,v) = 0; \quad i = 1,2,3 \quad (\text{A-33})$$

Quantities  $\bar{l}(w)$  and  $\bar{r}(u,v)$  represent the position along the line (trajectory) segment and the position on the patch surface respectively:

$$\text{(line)} \quad l_i(w) = p_i + \xi_i w L \quad (\text{A-34})$$

where  $\bar{\xi} \equiv (\bar{q} - \bar{p})/L =$  unit direction vector along the line,

$L \equiv |\bar{p} - \bar{q}| =$  length of the line segment,

$w \equiv$  normalized line length parameter ( $0 \leq w \leq 1$ ),

$(\bar{p}, \bar{q}) \equiv$  line end position vectors.

$$\text{(patch)} \quad \bar{r}_i(u,v) = [U][C][Q_i][C]^T[V]^T$$

### A.3.2 Numerical Method

Solution of (A-33) is obtained by the Newton-Raphson technique for solving a system of non-linear algebraic equations:

$$(1) \quad \bar{x}(n) = (x_1, x_2, x_3) \equiv (u, v, w)$$

$$\bar{F}(n) = \bar{l}[x_3(n)] - \bar{r}[x_1(n), x_2(n)]$$

$$(2) \quad J_{ij}(n) = \left[ \frac{\partial F_i}{\partial x_j} \right]_{\bar{x}(n)}$$

$$(3) \quad \sum_{j=1}^3 J_{ij}(n) \cdot \Delta_j(n) = -F_i(n) \quad (\bar{\Delta} \text{ is solved by Gauss elimination})$$

$$(4) \quad \bar{x}(n+1) = \bar{x}(n) + \bar{\Delta}(n)$$

Steps (1) thru (4) are iterated, each time updated with the correction vector  $\bar{\Delta}$ , until the equation (A-33) is satisfied within a specified tolerance.

Since the solution is sought within the specified line segment and on the patch surface, the following constraints must be imposed on the independent variables:

$$\begin{aligned} 0 &\leq x_1 (=u) \leq 1 \\ 0 &\leq x_2 (=v) \leq 1 \\ 0 &\leq x_3 (=w) \leq 1 \end{aligned}$$

The constraint equations are satisfied by the transformation

$$x_i = s_i^2 / (1 + s_i^2) \quad ; \quad s_i \in (-\infty, \infty) \quad ; \quad i = 1, 2, 3 \quad (\text{A-35})$$

The Newton-Raphson steps can be modified accordingly in terms of the new variable  $\bar{s} = (s_1, s_2, s_3)$ :

$$J_{ij}^*(n) = \sum_{k=1}^3 \left[ \frac{\partial F_i}{\partial x_k} \cdot \frac{\partial x_k}{\partial s_j} \cdot \delta_{jk} \right]_{\bar{s}(n)} = J_{ij}(n) \cdot 2s_j \cdot (1 + s_j^2)^{-2} \quad (\text{A-36})$$

$$\sum_{j=1}^3 J_{ij}^*(n) \cdot \Delta_j^*(n) = - F_i[\bar{s}(n)] \quad (\text{A-37})$$

$$\bar{s}(n+1) = \bar{s}(n) + \bar{\Delta}^*(n) \quad (\text{A-38})$$

Thus the transformation (A-35) modifies the Newton-Raphson Jacobian elements in a simple way, as shown in (A-36). The components of the unconstrained Jacobian elements are

$$J_{i1} = \frac{\partial}{\partial u} [l_i(w) - r_i(u, v)] = - \frac{\partial r_i(u, v)}{\partial u} = - [U'] [C] [Q_i] [C]^T [V]^T$$

$$J_{i2} = \frac{\partial}{\partial v} [l_i(w) - r_i(u, v)] = - \frac{\partial r_i(u, v)}{\partial v} = - [U] [C] [Q_i] [C]^T [V']^T$$

$$J_{i3} = \frac{\partial}{\partial w} [l_i(w) - r_i(u, v)] = \xi_i L$$

At the converged solution  $(u_0, v_0, w_0)$ , the intersection point  $(\bar{x}_m)$  and the unit outward normal vector  $\bar{n}(\bar{x}_m)$  are computed by substitution of  $(u_0, v_0)$  into the patch parametric equations (A-26) and (A-27):

$$(x_m)_i = \bar{r}_i(u_0, v_0)$$

$$(n)_i = H_i / \left( \sum_{j=1}^3 H_j^2 \right)^{1/2}$$

$$H_i = \sum_{j=1}^3 \sum_{k=1}^3 \epsilon_{ijk} \cdot J_{j1}(u_0, v_0) \cdot J_{k2}(u_0, v_0)$$

APPENDIX B

Derivation of the Trajectory Equation (3-1):

$$dU_i/dt = C_D(R_V) \cdot R_V \cdot (V_i - U_i) / (24P) - (1-\sigma)gC\delta_{i2}/V_\infty^2 \quad (B-1)$$

A vector diagram of the forces acting on the particle is shown in Figure B1.

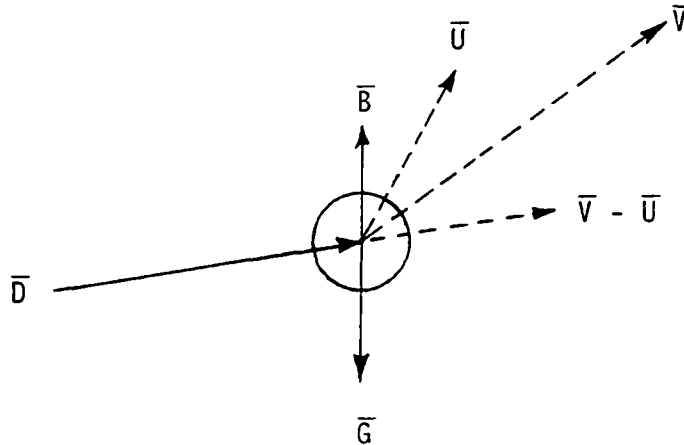


Figure B1 - Forces Acting on Particle and Velocities at Center of Particle

Drag force,  $\bar{D}$ , is given by

$$D_i = C_D(R_V) \cdot q \cdot a \cdot \cos(i,n) \quad (B-2)$$

- where
- $R_V = \rho |\tilde{V} - \tilde{U}| d / \mu$ ,
  - $C_D =$  sphere drag coefficient,
  - $q = \frac{1}{2} \rho |\tilde{V} - \tilde{U}|^2 =$  velocity head experienced by the particle in the flowfield,
  - $a = \pi d^2 / 4 =$  projected area of spherical particle,
  - $\tilde{V} =$  flow velocity,  $\tilde{U} =$  particle velocity,
  - $\cos(i,n) = (\tilde{V} - \tilde{U})_i / |\tilde{V} - \tilde{U}| =$  direction cosine between the unit vectors  $\hat{i}$  (// to i-axis) and  $\hat{n}$  (// to  $\tilde{V} - \tilde{U}$ ).

Using the definitions, (B-2) becomes

$$D_i = \frac{1}{2} \rho C_D(R_V) \cdot a \cdot |\tilde{V} - \tilde{U}| \cdot (\tilde{V} - \tilde{U})_i \quad (B-3)$$

Buoyancy and gravity forces are

$$B_i = \rho g \tau \delta_{i2} \quad (B-4)$$

$$G_i = -\rho^* g \tau \delta_{i2} \quad ; \quad \tau \equiv \pi d^3 / 6 = \text{volume of spherical particle}$$

where the gravity force is assumed to act along the -ve y (i=2) axis.

Summing the forces (  $\sum F = ma$  ),

$$d\tilde{U}_i/dt = \frac{1}{2} \rho C_D(R_V) \cdot (a/\tau) \cdot |\tilde{V} - \tilde{U}| \cdot (\tilde{V} - \tilde{U})_i - (1-\sigma)g\delta_{i2} \quad (B-5)$$

Introducing the inertia parameter,  $P \equiv \rho^* d^2 V_\infty / (18\mu C)$ , where C is the characteristic dimension of the boundary surface, the coefficient of  $|\tilde{V} - \tilde{U}|(\tilde{V} - \tilde{U})_i$  term in (B-5) can be written as

$$\begin{aligned} \frac{1}{2} \rho C_D(R_V) (a/\tau) &= \rho C_D(R_V) \cdot (\pi d^2 / 4) \cdot (2\rho^* \pi d^3 / 6)^{-1} = 3\rho C_D(R_V) \cdot (4\rho^* d)^{-1} \\ &= \frac{3\rho C_D(R_V)}{4 \left( \frac{\rho^* d^2 V_\infty}{18 \mu C} \right) \left( \frac{18\mu C}{V_\infty d} \right)} \\ &= \frac{C_D(R_V)}{24PC} \cdot \frac{\rho V_\infty d}{\mu} \\ &= \frac{C_D(R_V) R}{24PC} \end{aligned}$$

where  $R \equiv \rho V_{\infty} d / \mu$  ( Reynolds number based on  $d$  ).

Equation (B-5) thus becomes

$$\frac{d\tilde{U}_i/d\tilde{t}}{24 PC} = \frac{C_D(R_V) \cdot R \cdot |\tilde{V} - \tilde{U}| (\tilde{V} - \tilde{U})_i}{24 PC} - g(1 - \sigma)\delta_{i2} \quad (B-6)$$

Non-dimensionalizing (B-6)

$$\frac{d[\tilde{U}_i/V_{\infty}]}{d[\tilde{t}/(C/V_{\infty})]} = \frac{C_D(R_V) \cdot R_V \cdot (\tilde{V}_i/V_{\infty} - \tilde{U}_i/V_{\infty})}{24 P} - (1 - \sigma)gC\delta_{i2}/V_{\infty}^2$$

which is

$$dU_i/dt = \frac{C_D(R_V) \cdot R_V \cdot (V_i - U_i)}{24P} - (1 - \sigma)gC\delta_{i2}/V_{\infty}^2$$

where  $U_i \equiv \tilde{U}_i/V_{\infty}$ ,  $V_i \equiv \tilde{V}_i/V_{\infty}$  and  $t \equiv \tilde{t}/(C/V_{\infty})$ .

APPENDIX C

Table of Sphere Drag Coefficient ( $C_D$ ) :

R	STND. C D	C (STOKES) D	C (LANG) D	# C (GAUVIN) D	\$ C (PUTNAM) D	& C (NORMENT) D	*
0.05	484.3200	480.0000	494.3258	489.1944	490.8577	486.5822	
0.10	244.3200	240.0000	251.0861	247.4012	248.6177	244.9004	
0.20	124.4400	120.0000	128.5796	125.9577	126.8399	124.0419	
0.40	64.3800	60.0000	66.6405	64.7958	65.4288	63.5772	
0.60	44.1200	40.0000	45.7168	44.2242	44.7425	43.3909	
0.80	34.2600	30.0000	35.1407	33.8604	34.3089	33.2742	
1.00	28.2240	24.0000	28.7342	27.6000	28.0000	27.1854	
1.20	24.0200	20.0000	24.4263	23.4003	23.7641	23.1104	
1.40	21.0000	17.1429	21.3245	20.3830	20.7185	20.1862	
1.60	18.7200	15.0000	18.9808	18.1075	18.4200	17.9814	
1.80	16.8933	13.3333	17.1450	16.3284	16.6216	16.2560	
2.00	15.4200	12.0000	15.6666	14.8979	15.1748	14.8662	
2.50	12.7872	9.6000	12.9774	12.3024	12.5472	12.3317	
3.00	10.9920	8.0000	11.1583	10.5525	10.7734	10.6027	
3.50	9.6823	6.8571	9.8414	9.2894	9.4917	9.5507	
4.00	8.6820	6.0000	8.8414	8.3327	8.5198	8.7009	
5.00	7.2624	4.8000	7.4180	6.9753	7.1392	7.3895	
6.00	6.2880	4.0000	6.4488	6.0547	6.2013	6.4363	
8.00	5.0340	3.0000	5.2042	4.8777	5.0000	5.1559	
10.00	4.2768	2.4000	4.4318	4.1511	4.2566	4.3399	
12.00	3.8020	2.0000	3.9013	3.6539	3.7472	3.7759	
14.00	3.4440	1.7143	3.5121	3.2903	3.3739	3.3631	
16.00	3.1635	1.5000	3.2128	3.0115	3.0874	3.0479	
18.00	2.9307	1.3333	2.9747	2.7901	2.8596	2.7994	
20.00	2.7492	1.2000	2.7801	2.6095	2.6736	2.5984	
25.00	2.3894	0.9600	2.4181	2.2745	2.3280	2.2314	
30.00	2.1384	0.8000	2.1659	2.0415	2.0873	1.9827	
35.00	1.9550	0.6857	1.9785	1.8688	1.9086	1.8027	
40.00	1.8078	0.6000	1.8329	1.7346	1.7696	1.6661	
50.00	1.5970	0.4800	1.6195	1.5381	1.5658	1.4720	
60.00	1.4400	0.4000	1.4689	1.3994	1.4217	1.3400	
80.00	1.2330	0.3000	1.2674	1.2133	1.2283	1.1699	
100.00	1.1016	0.2400	1.1363	1.0917	1.1018	1.0628	
120.00	1.0020	0.2000	1.0427	1.0045	1.0110	0.9875	
140.00	0.9257	0.1714	0.9719	0.9380	0.9418	0.9304	
160.00	0.8640	0.1500	0.9160	0.8952	0.8868	0.8848	
180.00	0.8213	0.1333	0.8704	0.8419	0.8418	0.8467	
200.00	0.7824	0.1200	0.8325	0.8056	0.8040	0.8140	
250.00	0.7085	0.0960	0.7598	0.7354	0.7310	0.7473	
300.00	0.6608	0.0800	0.7075	0.6839	0.6775	0.6934	
350.00	0.6171	0.0686	0.6676	0.6440	0.6362	0.6469	
400.00	0.5892	0.0600	0.6359	0.6119	0.6029	0.6094	
500.00	0.5501	0.0480	0.5885	0.5627	0.5520	0.5627	
600.00	0.5188	0.0400	0.5543	0.5261	0.5143	0.5315	
800.00	0.4743	0.0300	0.5077	0.4743	0.4609	0.4926	
1000.00	0.4469	0.0240	0.4771	0.4383	0.4240	0.4692	



APPENDIX D

Comparison between the Computed 3-D Full Potential CFD Flow Data and Wind Tunnel Test Data ( from NASA CR-3514 and Boeing Document D6-49848):

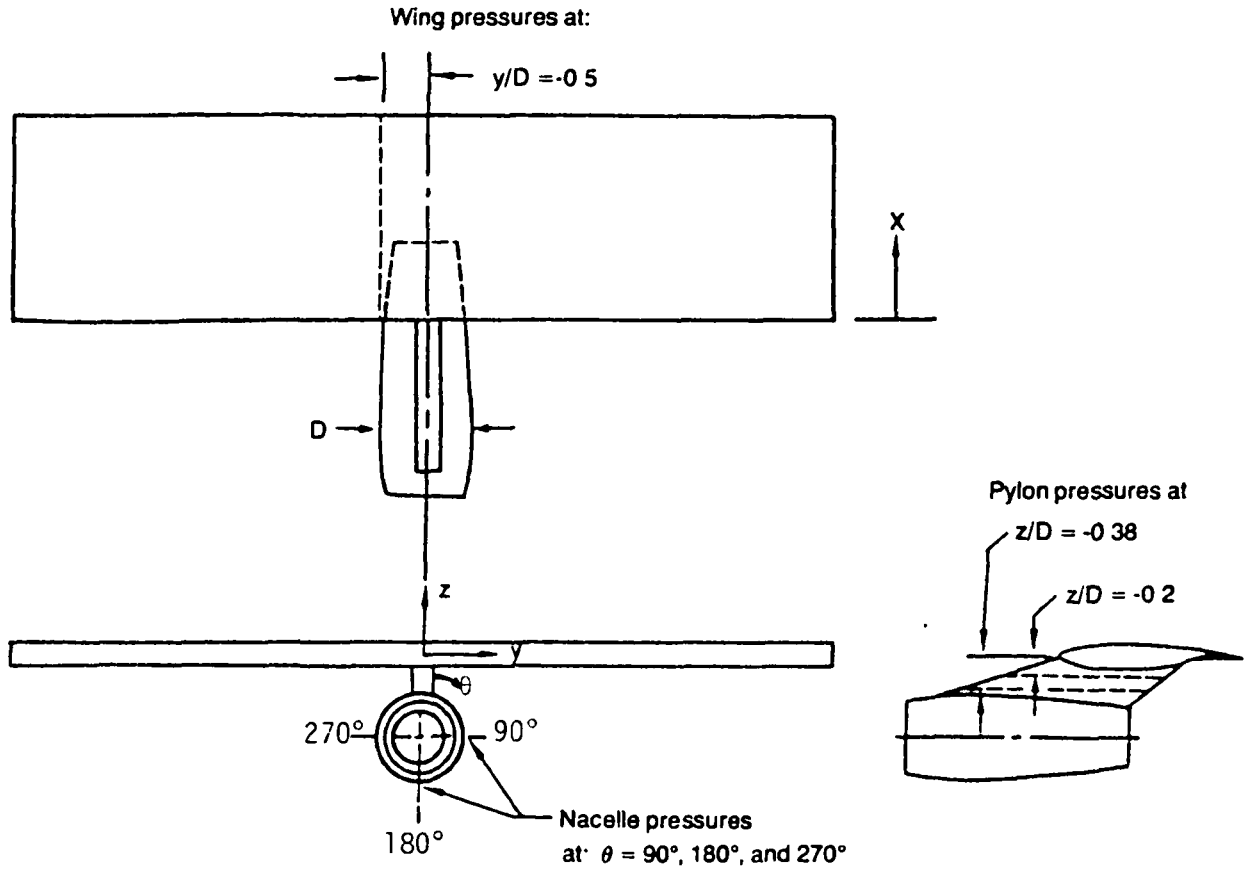


Figure D1 - NASA Wing-Pylon-Nacelle Test Model; Location of Pressure Measurements Used for Analysis Comparison (from NASA CR-3514)

C-2

$$\# \quad C_D = 24(1 + .197R^{.63} + 2.6E-04R^{1.38})/R ; \text{ REFERENCE[17] }$$

$$\$ \quad C_D = 24(1 + .15R^{.687})/R ; \text{ REFERENCE[47] }$$

$$\& \quad C_D = 24(1 + 1/6R^{2/3})/R ; \text{ REFERENCE[48] }$$

$$* \quad C_D R = 24.167R^2 + 3.254R^2 - .23564R^3, .05 \leq R \leq 3.04726$$

$$= -28.339 + 38.969R + .73204R^2 - 5.6084E-04R^3, 3.04726 < R \leq 377.566$$

$$= 93.462R + .37576R^2, 377.566 < R ; \text{ REFERENCE[49] }$$

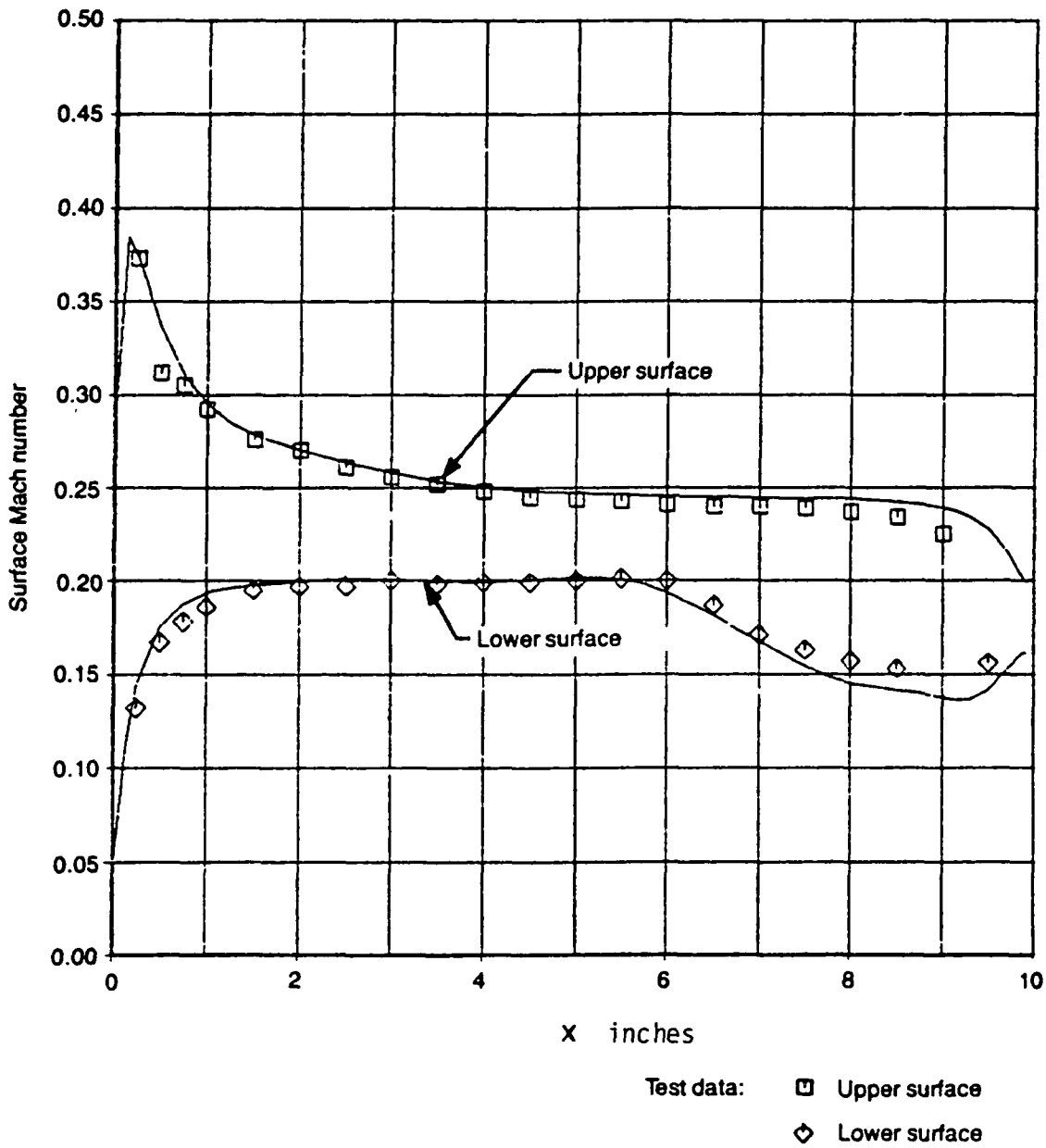


Figure D2 - Wing Surface Mach Number Distribution, Wing-Pylon-Nacelle Model;  $M_\infty = 0.2$ ,  $\alpha = 5^\circ$ ,  $D = 4.5''$   
 (from NASA CR-3514)

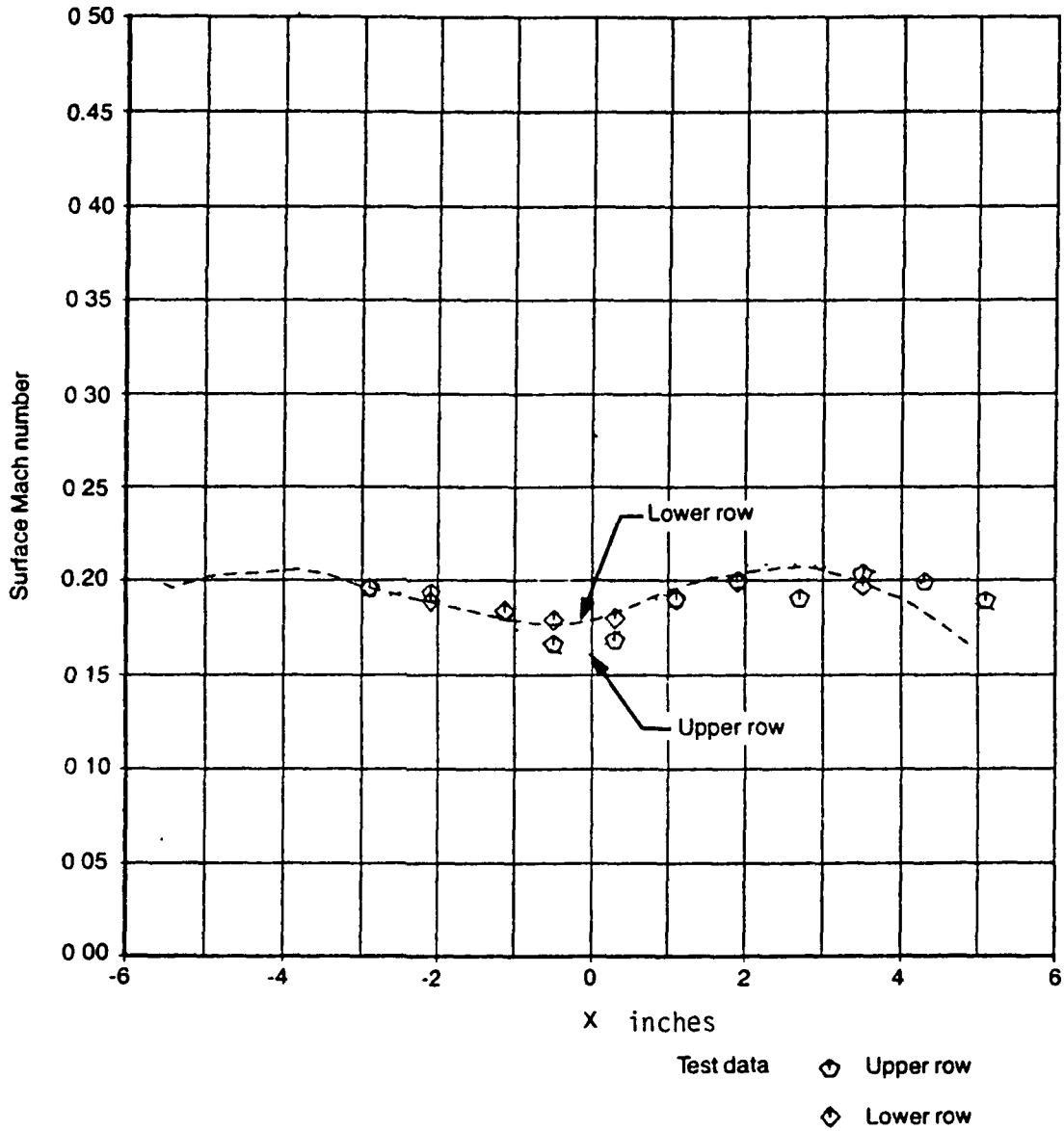


Figure D3 - Pylon Surface Mach Number Distribution, Wing-Pylon-Nacelle Model;  $M_\infty = 0.2$ ,  $\alpha = 5^\circ$ ,  $D = 4.5''$   
 (from NASA CR-3514)

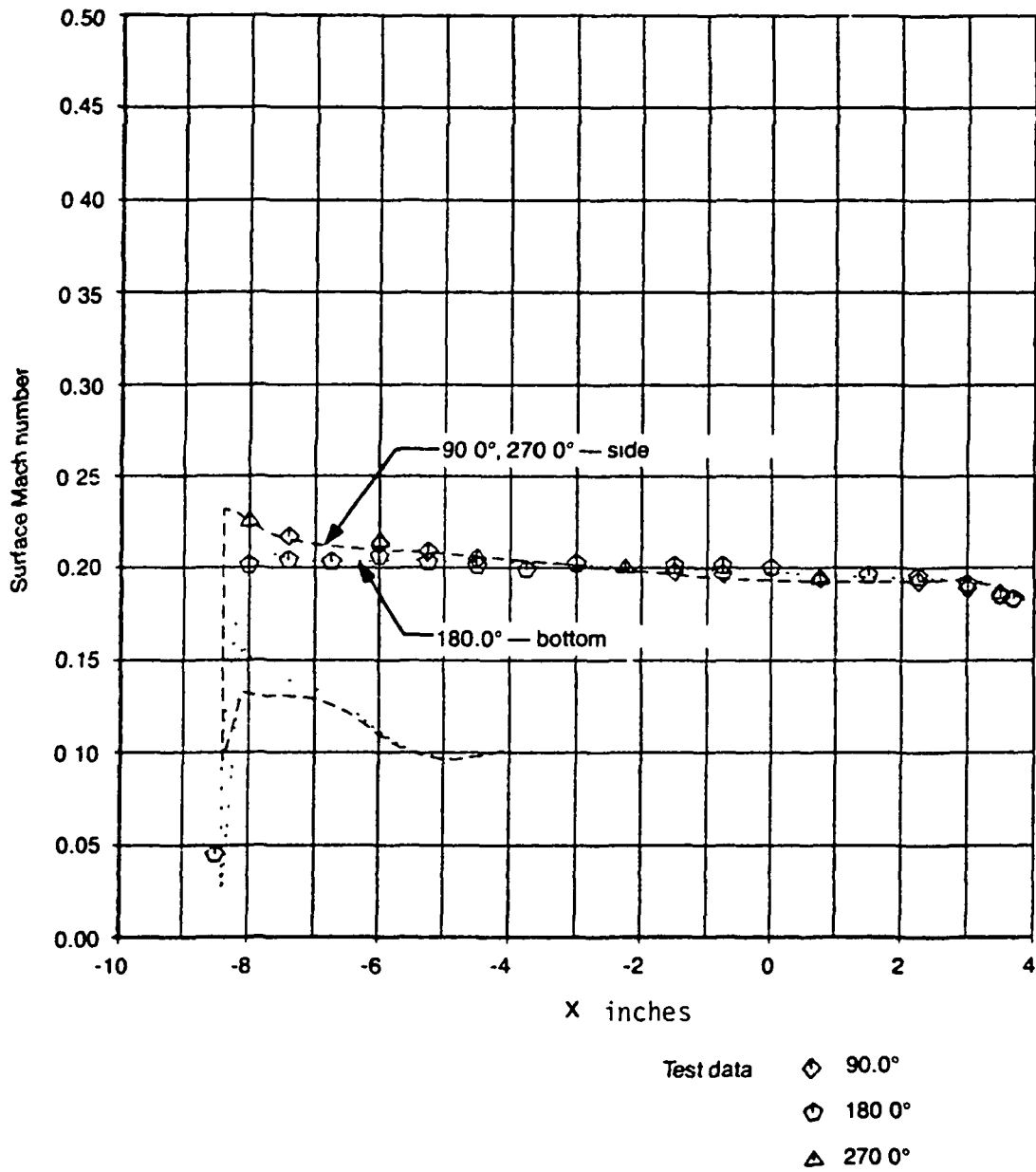


Figure D4 - Nacelle Surface Mach Number Distribution, Wing-Pylon-Nacelle Model;  $M_\infty = 0.2$ ,  $\alpha = 5^\circ$ ,  $D = 4.5''$   
 (from NASA CR-3514)

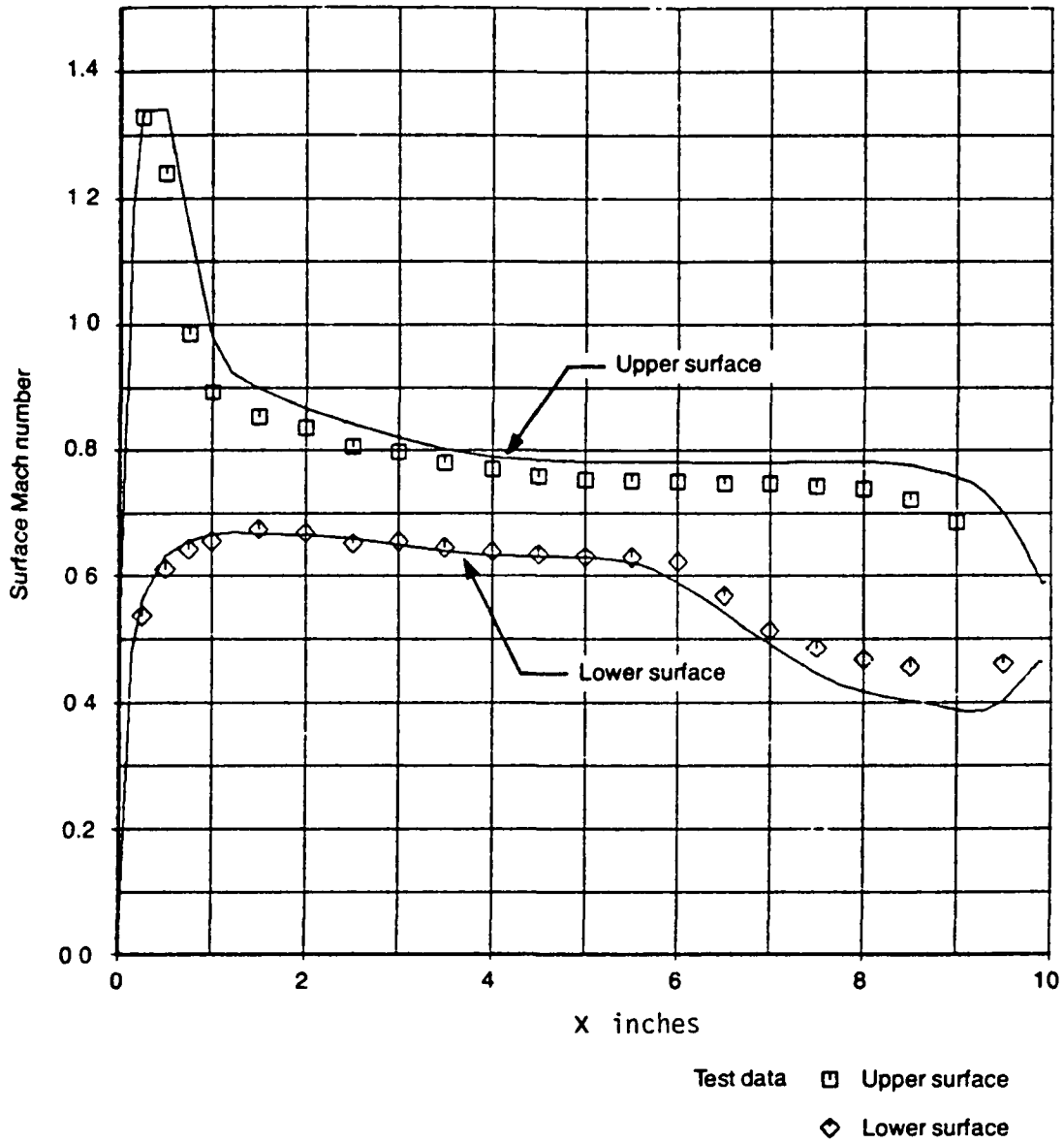


Figure D5 - Wing Surface Mach Number Distribution, Wing-Pylon-Nacelle Model;  $M_{\infty} = 0.6$ ,  $\alpha = 3^{\circ}$ ,  $D = 4.5''$   
 (from NASA CR-3514)

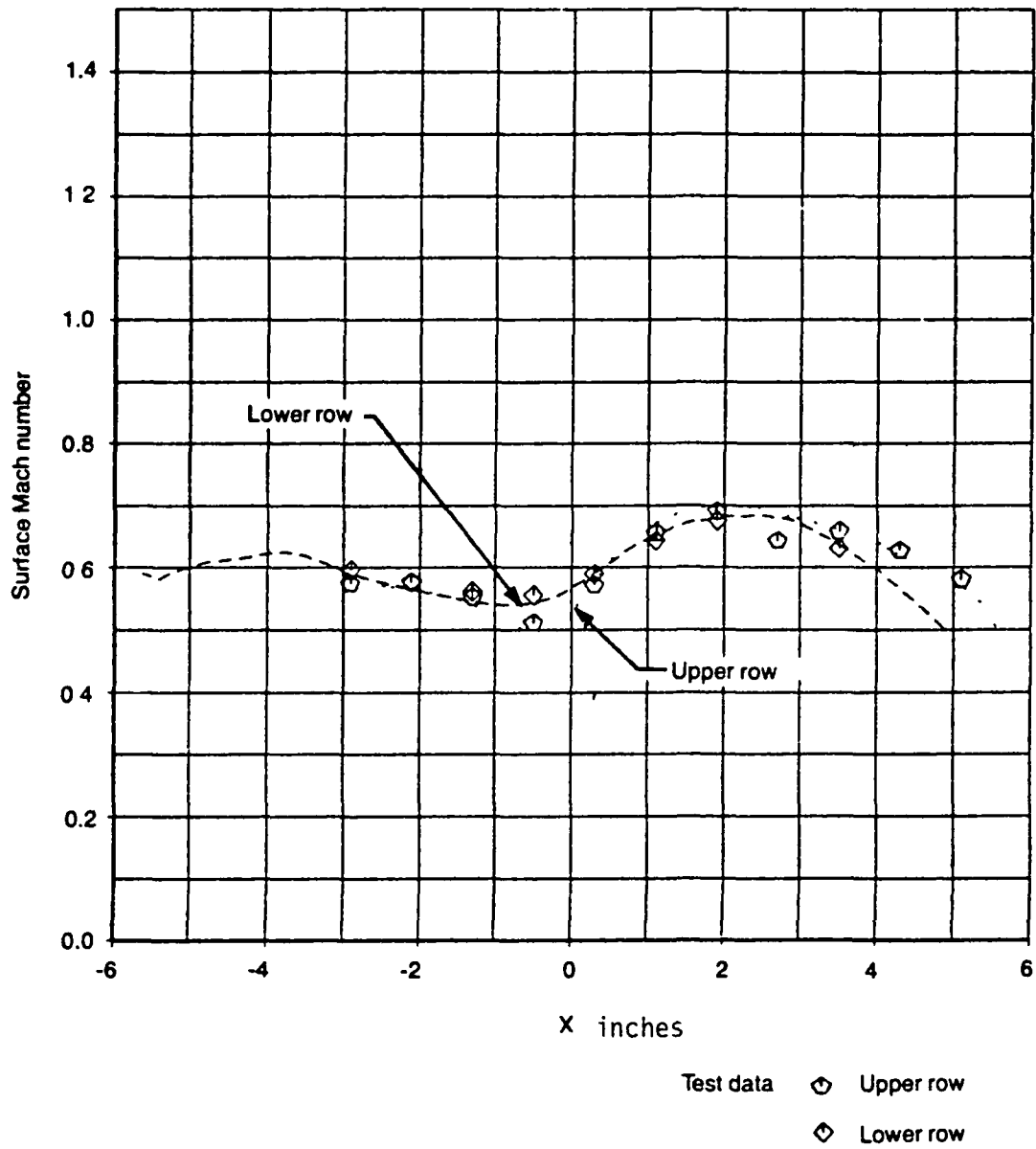


Figure D6 - Pylon Surface Mach Number Distribution, Wing-Pylon-Nacelle Model;  $M_\infty = 0.6$ ,  $\alpha = 3^\circ$ ,  $D = 4.5''$   
 (from NASA CR-3514)

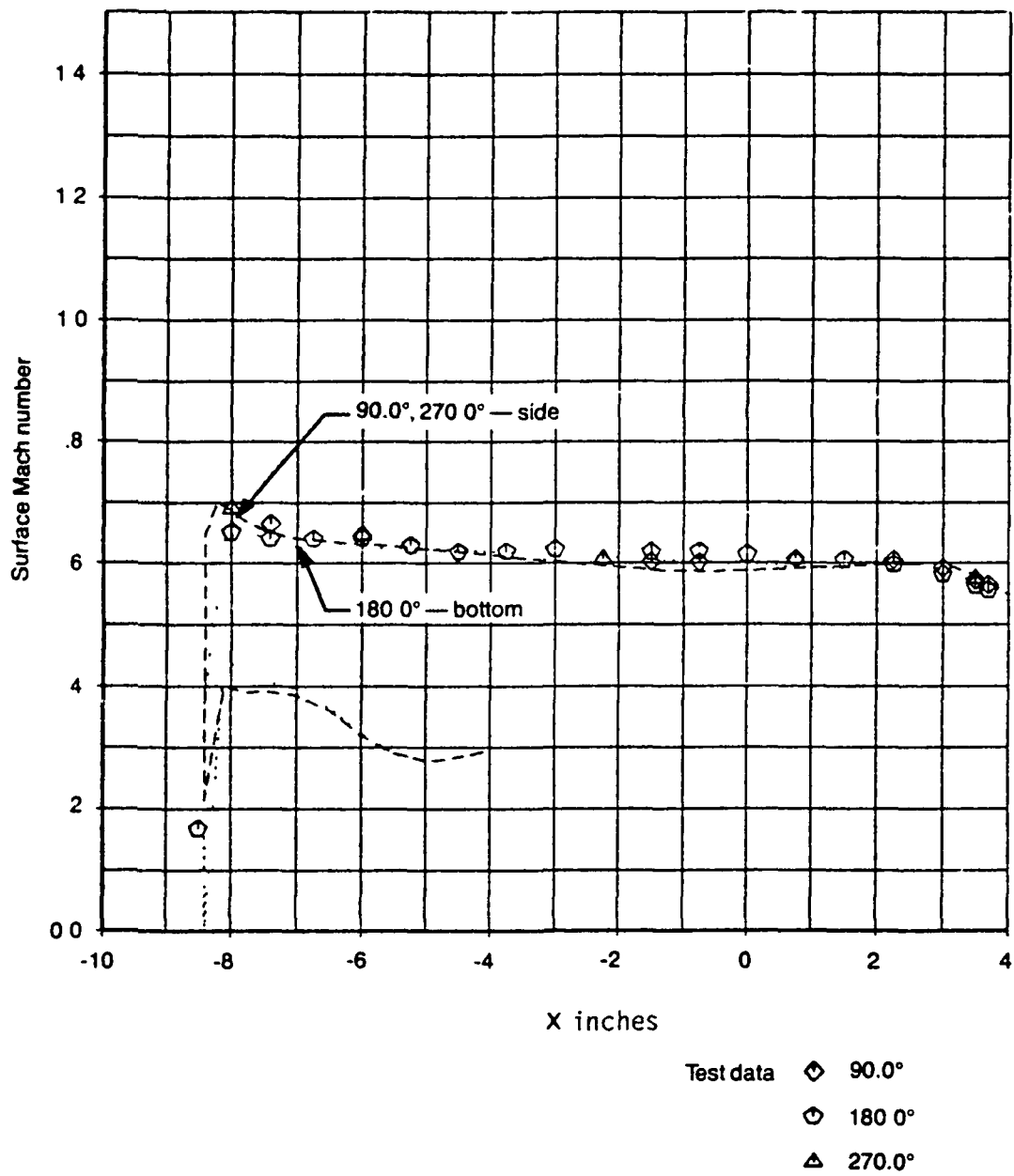


Figure D7 - Nacelle Surface Mach Number Distribution, Wing-Pylon-Nacelle Model;  $M_\infty = 0.6$ ,  $\alpha = 3^\circ$ ,  $D = 4.5''$   
 (from NASA CR-3514)



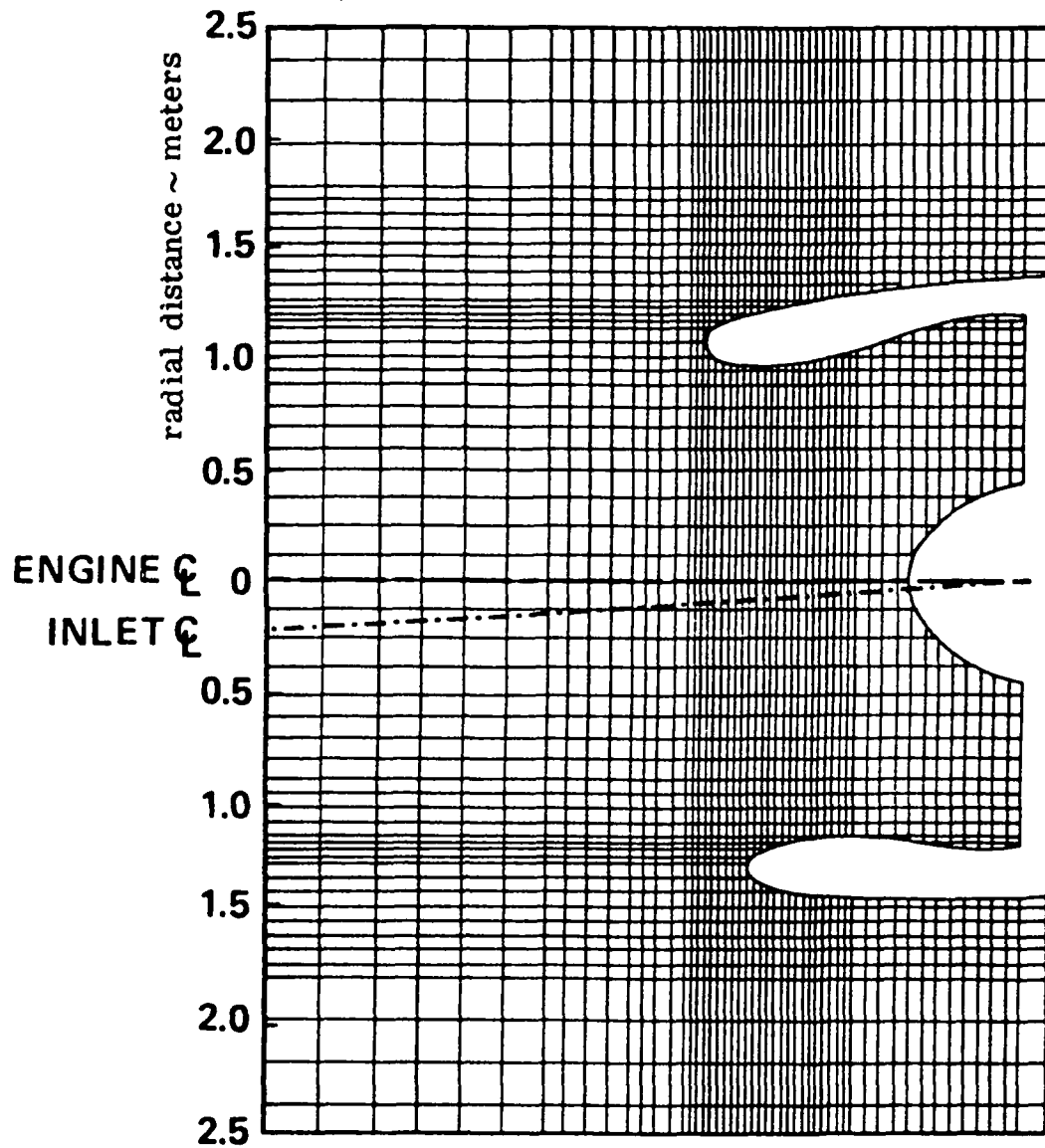


Figure D8 - Computational Mesh in the Vicinity of a Commercial -  
 Transport Turbofan-Engine Type Inlet  
 (from NASA CR-3514)

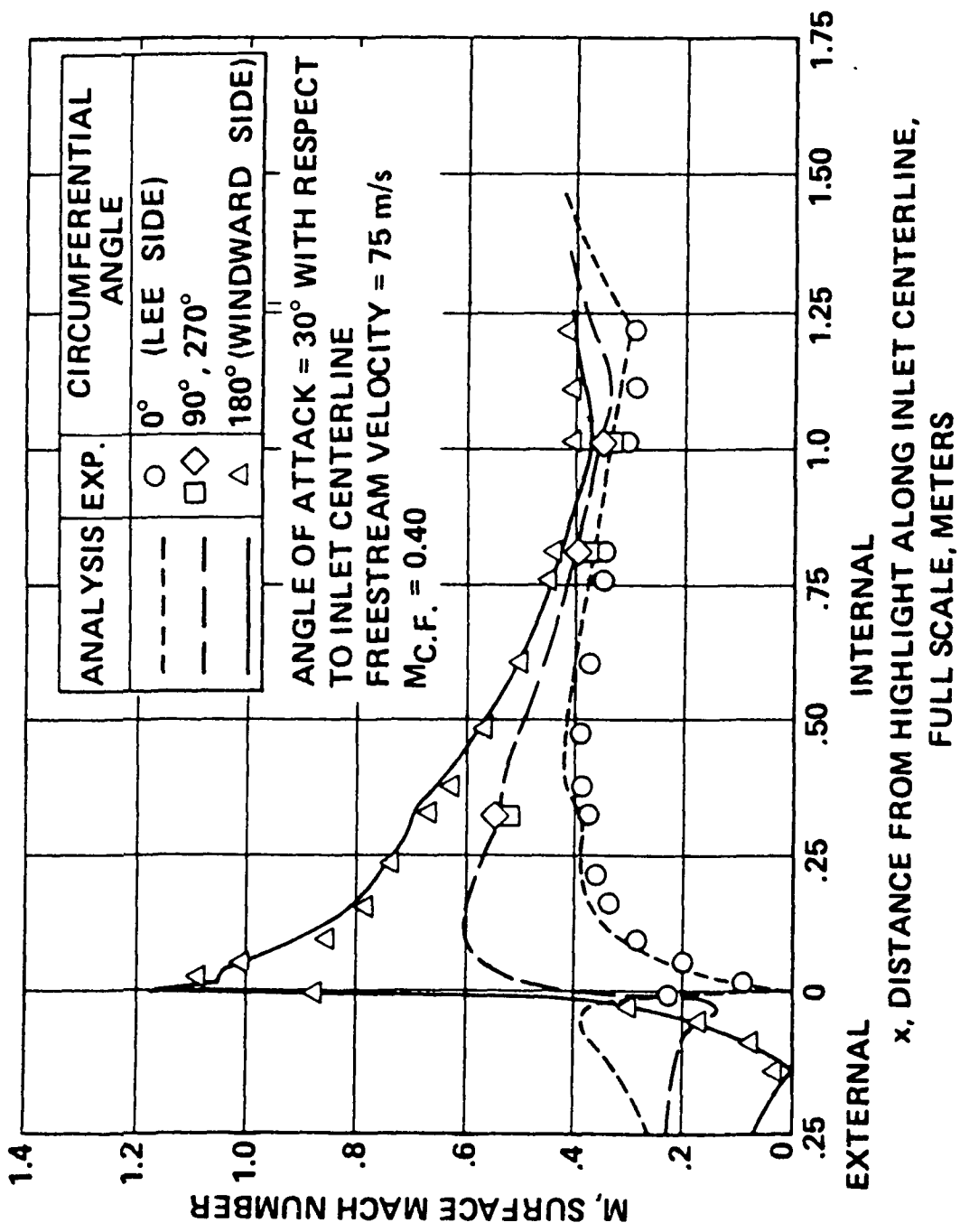


Figure D9 - Cowl Surface Mach Number Distribution for a Commercial Turbofan-Engine Type Inlet;  $\alpha = 25^\circ$   
 (from NASA CR-3514)

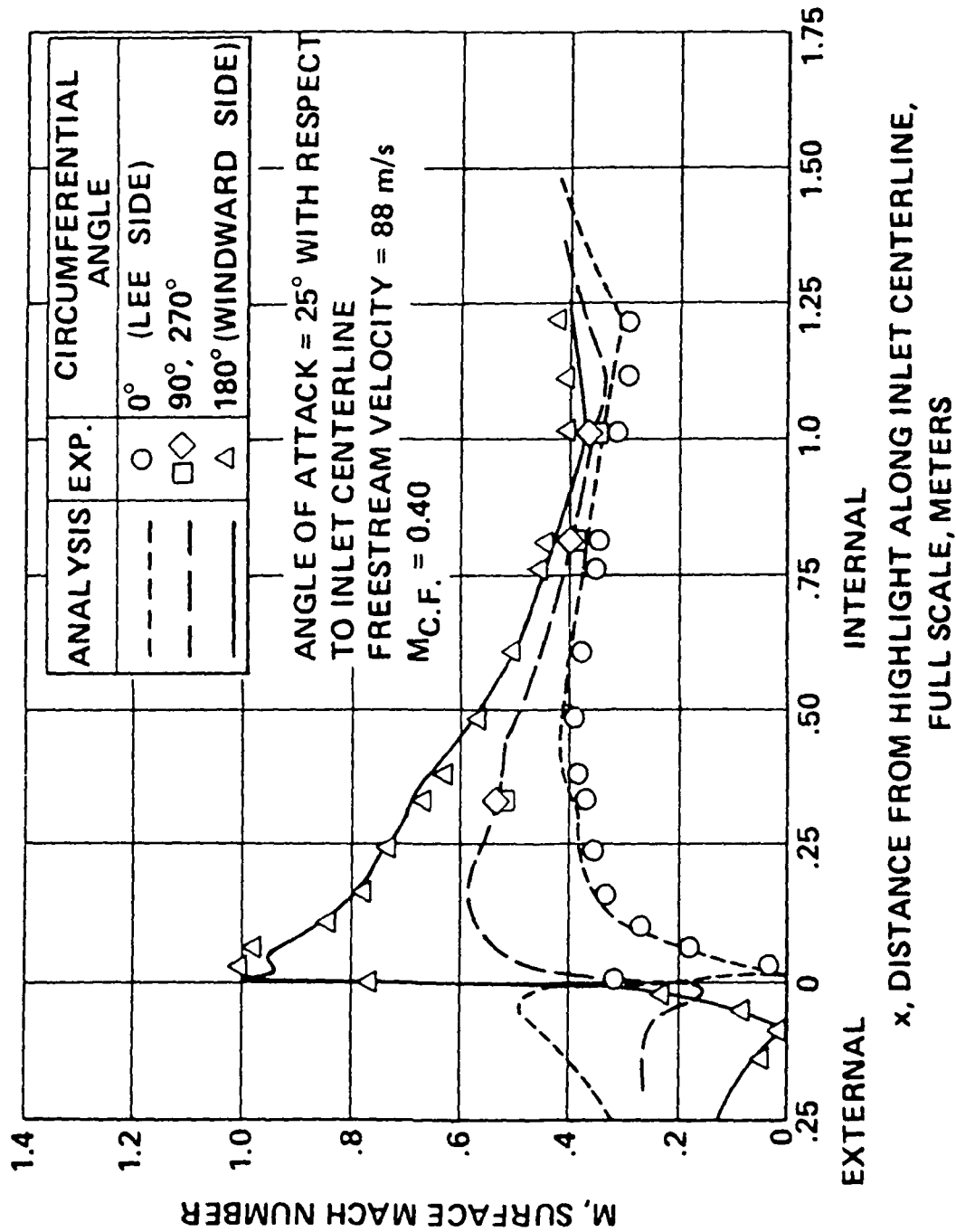


Figure D10 - Cowl Surface Mach Number Distribution for a Commercial Turbofan-Engine Type Inlet;  $\alpha = 30^\circ$   
 (from NASA CR-3514)

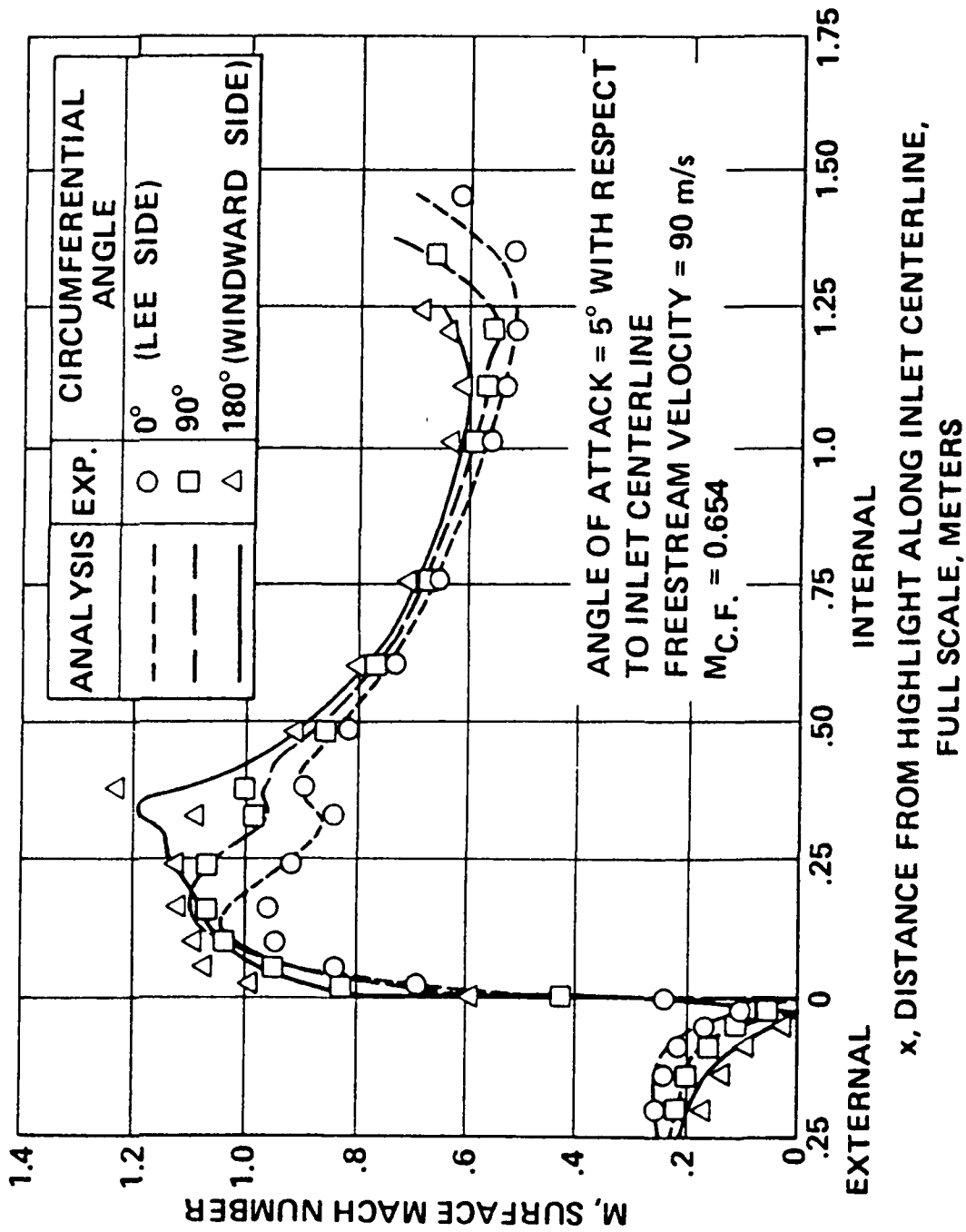


Figure D11 - Cowl Surface Mach Number Distribution for a Commercial Turbofan-Engine Type Inlet;  $\alpha = 5^\circ$   
 (from NASA CR-3514)

## REFERENCES

1. Federal Aviation Regulation Part 25, Appendix C, 1974.
2. Peterson, A.A. and Dunford, P.J., "Qualification of a Composite Rotor Blade Electrothermal Deicing System", paper no. AIAA-84-2481, AIAA/AHS/ASEE Aircraft Design, System, and Operations Meeting, San Diego, California, November 1984.
3. Zumwalt, G.W., "Icing Tunnel Tests of Electro-Impulse Deicing of an Engine Inlet and High-Speed Wings", paper no. AIAA-85-0466, AIAA 23rd Aerospace Sciences Meeting, Reno, Nevada, January 1985.
4. Albright, A., "A Summary of NASA's Research on the Fluid Ice Protection System", paper no. AIAA-85-0467, AIAA 23rd Aerospace Sciences Meeting, Reno, Nevada, January 1985.
5. Cansdale, J.T. and Gent, R.W., "Ice Accretion on Aerofoils in 2-Dimensional Compressible Flow - A Theoretical Model", RAE TR 82128, January 1983.
6. Lozowski, E.P. and Oleskiw, M.M., "Computer Simulation of Airfoil Icing Without Runback", paper no. AIAA-81-0402, AIAA 19th Aerospace Sciences Meeting, St. Louis, Mo., Jan 12-15, 1981.
7. Potapczuk, M.G. and Gerhart, P.M., "Progress in Development of a Navier-Stokes Solver for Evaluation of Iced Airfoil Performance", paper no. AIAA-85-0410, AIAA 23rd Aerospace Sciences Meeting, Reno, Nevada, January 1985.
8. Bragg, M.B. and Gregorek, G.M., "An Analytical Evaluation of the Icing Properties of Several Low and Medium Speed Airfoils", paper no. AIAA-83-0109, AIAA 21st Aerospace Sciences Meeting, Reno, Nevada, January 10-13, 1983.

9. Shaw, R.J., "Progress Toward the Development of an Aircraft Icing Analysis Capability", NASA TM 83562, 1983.
10. Dorsch, R.G., Brun, R.J. and Gregg, J.L., "Impingement of Water Droplets on an Ellipsoid With Fineness Ratio 5 in Axisymmetric Flow", NACA TN 3099, 12954.
11. Lewis, J.P. and Ruggeri, R.S., "Experimental Droplet Impingement on Four Bodies of Revolution", NACA TN 4092, 1957.
12. Bergrun, N.R., "A Method for Numerically Calculating the Area and Distribution of Water Impingement on the Leading Edge of an Airfoil in a Cloud", NACA TN 1397, 1947.
13. Brun, R.J., Gallagher, H.M. and Vogt, D.E., "Impingement of Water Droplets on NACA 65-208 and 65-212 Airfoils at 4 Degree Angle of Attack", NACA TN 2952, 1953.
14. Brun, R.J., Gallagher, H.M. and Vogt, D.E., "Impingement of Water Droplets on NACA 65A004 Airfoil and Effect of Change in Airfoil Thickness from 12 to 4 Percent at 4 Degree Angle of Attack", NACA TN 3047, 1953.
15. Gelder, T.F., Symers, W.H. and Von Glahn, U.H., "Experimental Droplet Impingement on Several Two-Dimensional Airfoils with Thickness Ratios of 6 to 16 Percent", NACA TN 3839, 1955.
16. Gelder, T.F., Smyers, W.H. and Von Glahn, U.H., "A Dye-Tracer Technique for Experimentally Obtaining Impingement Characteristics of Arbitrary Bodies and a Method for Determining Droplet Size Distribution", NACA TN 3338, 1955.
17. Langmuir, I. and Blodgett, K.B., "A Mathematical Investigation of Water Droplet Trajectories", Army Air Forces Technical Report No. 5418, 1946.

18. Bragg, M.B. and Gregorek, G.M. "An Analytical Approach to Airfoil Icing", paper no. AIAA-81-0403, AIAA 19th Aerospace Sciences Meeting, St. Louis Mo., Jan 12-15, 1981.
19. Frost, W., Chang, H.P. and Kimble, K.R., "Particle Trajectory Computer Program for Icing Analysis", Final Report for NASA/Lewis Research Center under Contract NAS 3-22448 by FWG Associates, Inc., 1982.
20. Chang, H.P. and Kimble, K.R., "Influence of Multidroplet Size Distribution on Icing Collection Efficiency", paper no. AIAA-83-0110, AIAA 21st Aerospace Sciences Meeting, Reno, Nevada, January 10-13, 1983.
21. Schmidt, W.F., "Water Droplet Impingement Prediction for Engine Inlets by Trajectory Analysis in a Potential Flow Field", Boeing Document D3-6961, Final Report, 1965.
22. Breer, M.D. and Seibel, W., "Particle Trajectory Computer Program - User Manual", Boeing Document D3-9655-1, December 1974.
23. Norment, H.G., "Calculation of Water Drop Trajectories To and About Arbitrary Three-Dimensional Bodies in Potential Airflow", NASA CR-3291, August 1980.
24. Stock, H.W., "Water Droplet Trajectory Computation Around an Air Intake", Zeitschrift fur Flugwissenschaften and Weltraumforschung, Band 8, 1984, Heft 3, pp. 200-208.
25. Hess, J.L. and Smith, A.M.O., "Calculation of Potential Flow About Arbitrary Bodies", Progress in Aeronautical Sciences, Vol. 8, edited by D. Kuechemann, Pergamon Press, pp 1-138, 1967.

26. Grashof, J., "Investigation of the three-dimensional Transonic Flow around an Air Intake by a Finite Volume Method for the Euler Equations", Recent Contributions to Fluid Mechanics, edited by W. Haase, Springer-Verlag, 1982.
27. Thompson, J.F., "A Survey of Grid Generation Techniques in Computational Fluid Dynamics", paper no. AIAA-83-0447, AIAA 21st Aerospace Sciences Meeting, Reno, Nevada, January 1983.
28. Reyhner, T.A., "Transonic Potential Flow Computation About Three-Dimensional Inlets, Ducts, and Bodies", AIAA Journal, Vol. 19, September 1981, pp. 1112-1121.
29. Reyhner, T.A., "Computation of Transonic Potential Flow About Three-Dimensional Inlets, Ducts, and Bodies", NASA CR-3514 (Boeing Document D6-49848), March 1982.
30. Gibson, S.G., "User's Manual for MASTER: Modeling of Aerodynamic Surfaces by Three-Dimensional Explicit Representation", Boeing Document D6-51088, January 1983.
31. Rudinger, G., "Penetration of Particles into a Constant Cross Flow", AIAA J., Vol. 12, pp 1138-1140, 1974.
32. Kriebel, A.R., "Particle Trajectories in a Gas Centrifuge", J. Basic Eng., Trans. ASME, 83D, pp 333-340, 1961.
33. Gunn, R. and Kinzer, G.D., "The Terminal Velocity of Fall for Water Droplets in Stagnant Air", J. of Meteor, Vol. 6, pp 243-248, August 1949.
34. Beard, K. and Purppacher, H.R., "A Determination of the Terminal Velocity and Drag of Small Water Drops by Means of a Wind Tunnel", J. of the Atmospheric Sci., Vol. 26, pp 1066-1072, 1969.



35. LeClair, B.P., Hamielec, A.E., Pruppacher, H.R. and Hall, W.D., "A Theoretical and Experimental Study of the Internal Circulation in Water Drops Falling at Terminal Velocity in Air", J. of the Atmospheric Sci., Vol. 29, pp 728-740, May 1972.
36. Rudinger, G., "Fundamentals of Gas-Particle Flow", Elsevier Scientific Publishing Company, 1980, pp. 7-12.
37. Schaaf, S.A. and Chambre, P.L., "Flow of Rarefied Gases", Section H of Fundamentals of Gas Dynamics, Editor, High Speed Aerodynamics and Jet Propulsion, Vol. III, Princeton University Press, Princeton, New Jersey, 1958.
38. Carlson, D.J. and Hoggund, R.F., "Particle Drag and Heat Transfer in Rocket Nozzles", AIAA J., Vol. 2, no. 11, pp. 1980-1984, Nov. 1964.
39. Faux, I.D., and Pratt, M.J., "Computational Geometry for Design and Manufacture", Ellis Horwood Publishers, 1979, pp. 198-210.
40. Brandt, A., "Multilevel Adaptive Computations in Fluid Dynamics", AIAA Journal, Vol. 18, October 1980, pp. 1165-1172.
41. McCarthy, D.R. and Reyhner, T.A., "Multigrid Code for Three-Dimensional Transonic Potential Flow About Inlets", AIAA Journal, Vol. 20, January 1982, pp. 45-50.
42. Householder A.S., "The Theory of Matrices in Numerical Analysis", Blaisdell, 1965.
43. Spurny, K.R., Gentry, J.W. and Stober, W., "Sampling and Analysis of Fibrous Aerosol Particles", Fundamentals of Aerosol Science, D.T. Shaw (Editor), John Wiley, New York, pp 257-324, 1978

44. Lapple, C.E., "Characteristics of Particles and Particle Dispersoids", Stanford Research Institute Journal, 3rd Quarter, 1961.
45. Tabakoff, W. and Sugiyama, Y., "Experimental Method of Determining Particle Restitution coefficients", Symposium on Polyphase Flow and Transient Technology Proceedings, 1980.
46. Bragg, M.G., Gregorek, G.M. and Lee, J.D., "Experimental and Analytical Investigations into Airfoil Icing", paper no. ICAS-84-1.10.4 presented at the 14th Congress of the Aeronautical Sciences, Toulouse, France, September 10-14, 1984.
47. Gauvin, W.H., "Fundamental Aspects of Solid-Gas Flow", Can. Journal of Chem. Eng., 37, pp. 129-141, 1959.
48. Putnam, A., "Integrable Form of Droplet Drag Coefficient", ARS Journal, 31, pp. 1467-1468, 1961.
49. Norment, H., "Effects of Airplane Flow Fields on Hydrometeor Concentration Measurements", Final Report AFCRL-TR-74-0602, December, 1974.

1 Report No <b>NASA CR-175023 DOT-FAA-CT-86-1</b>	2 Government Accession No	3 Recipient's Catalog No.	
4 Title and Subtitle  <b>Particle Trajectory Computation on a 3-Dimensional Engine Inlet</b>		5 Report Date  <b>January 1986</b>	
		6 Performing Organization Code	
7 Author(s)  <b>John J. Kim</b>		8 Performing Organization Report No  <b>None</b>	
		10 Work Unit No	
9 Performing Organization Name and Address  <b>Wichita State University College of Engineering Wichita, Kansas</b>		11 Contract or Grant No  <b>NAG 3-566</b>	
		13 Type of Report and Period Covered  <b>Contractor Report</b>	
12 Sponsoring Agency Name and Address  <b>National Aeronautics and Space Administration Washington, D.C. 20546</b>		14 Sponsoring Agency Code  <b>505-68-11</b>	
		15 Supplementary Notes  <b>Final report. Project Managers, Robert J. Shaw, Propulsion Systems Division, NASA Lewis Research Center, Cleveland, Ohio 44135 and James Riley, Federal Aviation Administration. This report was submitted as a dissertation in partial fulfillment of the requirements of the degree of Doctor of Philosophy to Wichita State University in May 1985. The droplet trajectory analysis computer code was developed at Boeing Military Airplane Company by Dr. J.J. Kim. It is being provided to the aerospace community as part of a NASA/FAA/Boeing/Wichita State joint program in aircraft icing.</b>	
16 Abstract  <b>A 3-dimensional particle trajectory computer code has been developed to compute the distribution of water droplet impingement efficiency on a 3-dimensional engine inlet. The computed results provide the essential droplet impingement data required for the engine inlet anti-icing system design and analysis. The droplet trajectories are obtained by solving the trajectory equation using the fourth order Runge-Kutta and Adams predictor-corrector schemes. A compressible 3-D full potential flow code is employed to obtain a cylindrical grid definition of the flowfield on and about the engine inlet. The inlet surface is defined mathematically through a system of bi-cubic parametric patches in order to compute the droplet impingement points accurately. Analysis results of the 3-D trajectory code obtained for an axisymmetric droplet impingement problem are in good agreement with NACA experimental data. Experimental data are not yet available for the engine inlet impingement problem analyzed in this study. Applicability of the method to solid particle impingement problems, such as engine sand ingestion, is also demonstrated.</b>			
17 Key Words (Suggested by Author(s))  <b>Aircraft icing; Water droplet trajectory analysis; Three dimensional flow field analysis; Inlet flow field analysis</b>		18 Distribution Statement  <b>Unclassified - unlimited STAR Category 03</b>	
19 Security Classif (of this report)  <b>Unclassified</b>	20 Security Classif (of this page)  <b>Unclassified</b>	21 No of pages	22 Price*

National Aeronautics and  
Space Administration

**Lewis Research Center**  
Cleveland, Ohio 44135

Official Business  
Penalty for Private Use \$300

SECOND CLASS MAIL

ADDRESS CORRECTION REQUESTED



Postage and Fees Paid  
National Aeronautics and  
Space Administration  
NASA-451

**NASA**

---